

Molecular Dynamics Study of Effects of Geometric Defects on the Mechanical Properties of Graphene

by

Nuwan Dewapriya Mallika Arachchige

B.Sc., University of Moratuwa, Sri Lanka, 2008
M.Sc., University of Moratuwa, Sri Lanka, 2010

A THESIS SUBMITTED IN PARTIAL FULFILLMENT OF
THE REQUIREMENTS FOR THE DEGREE OF
MASTER OF APPLIED SCIENCE

in

The Faculty of Graduate Studies
(Mechanical Engineering)

THE UNIVERSITY OF BRITISH COLUMBIA
(Vancouver)

April 2012

© Nuwan Dewapriya Mallika Arachchige 2012

Abstract

Graphene is a flat monolayer of carbon atoms arranged in a two-dimensional hexagonal lattice. It is the strongest material ever measured with strength exceeding more than hundred times of steel. However, the strength of graphene is critically influenced by temperature, vacancy defects (missing carbon atoms) and free edges. A systematic Molecular Dynamics (MD) simulation study is performed in this thesis to understand the effects of temperature, free edges, and vacancy defects on the mechanical properties of graphene. Results indicate that graphene has a positive coefficient of thermal expansion. However, the amplitude of intrinsic ripples (out-of-plane movement of carbon atoms) increases with increasing temperature, which reduces the net effect of thermal expansion. This is probably the reason for negative values of thermal expansion coefficient observed in some experiments. The MD simulations provide significant insights. At higher temperatures the sheets are observed to fail at lower strains due to high kinetic energy of atoms. Excess edge energy of a narrow graphene sheet is found to induce an initial strain at equilibrium configuration. Free edges have a greater influence on the mechanical properties of zigzag sheets compared to those of armchair sheets. Simulation of sheets with vacancy defects indicates that a single missing atom could reduce the strength by nearly 20%. It is also found that the calculated strength based on Griffith's theory falls below the results from MD simulations. The results obtained in this study are useful to the design and fabrication of graphene based nano-devices.

Table of Contents

Abstract	ii
Table of Contents	iii
List of Tables	vi
List of Figures	vii
List of Symbols	xi
List of Abbreviations	xii
Acknowledgements	xiii
Dedication	xiv
1 Introduction	1
1.1 Nanotechnology	1
1.2 Graphene	2
1.3 Nanomechanics	3
1.4 Mechanics of Geometric Defects of Graphene	8
1.4.1 Edge Effects	8
1.4.2 Defects	10
1.5 Scope of Current Work	12
2 Molecular Dynamics Simulations	13
2.1 Introduction	13
2.2 Basic Theory	13

Table of Contents

2.2.1	Equation of Motion	13
2.2.2	Temperature Control	15
2.2.3	Pressure Control	16
2.2.4	NPT Ensemble	17
2.3	Potential Fields	19
2.3.1	AIREBO Potential Field	21
2.4	Molecular Dynamics Parameters	26
2.4.1	Time step	28
2.4.2	Strain Rate	28
2.4.3	Periodic Boundary Conditions	30
2.5	Overview of LAMMPS	31
2.5.1	Uniaxial Tensile Test in LAMMPS	33
2.6	Overview of VMD	33
2.7	Conclusions	35
3	Effect of Temperature and Edges on the Mechanical Properties of Graphene	38
3.1	Effect of Temperature	39
3.1.1	Thermal Expansion	39
3.1.2	Stress Strain Behaviour	43
3.2	Effect of Edges	58
3.2.1	Equilibrium Configuration	59
3.2.2	Stress Strain Behaviour	64
3.2.3	Effect of Temperature on Edge Effect	69
3.3	Effect of Curvature on the Strength of Carbon Nanotubes	74
3.4	Conclusions	78
4	Fracture of Defective Graphene	82
4.1	Introduction	82
4.2	Effects of Vacancy Defects	82
4.3	Continuum Fracture Mechanics Approaches	88
4.3.1	Inglis' Local Stress	89
4.3.2	Griffith's Energy Balance	92

Table of Contents

4.3.3 Comparison of Continuum Approaches with MD	94
4.4 Conclusions	97
5 Summary and Conclusions	100
5.1 Summary of the Present Work and Major Findings	100
5.2 Suggestions for Future Work	101
Bibliography	102
Appendix A Input Files for LAMMPS	116
Appendix B Input Files for VMD	120

List of Tables

2.1	Dependence of mechanical properties of a graphene sheet on the strain rate.	30
3.1	Average physical quantities of graphene at equilibrium.	41
3.2	Strain energy and stress of graphene sheets at various tem- peratures and under a strain of 0.078.	44
3.3	Strain energy stored in a graphene sheet up to fracture at various temperatures.	48
3.4	Initial stress of graphene sheets given by Eq. (3.6) at various temperatures and under unstrained condition.	51
3.5	Virial stress of a graphene sheet given by Eq. (3.7) at various temperatures and under unstrained condition.	54
3.6	Excess edge energy of graphene sheets by different methods. .	63

List of Figures

1.1	Some example of nanomechanical models.	5
1.2	Bond based finite element method.	6
1.3	Elements of atomic-scale finite element method.	7
1.4	Armchair and zigzag edges of a finite graphene sheet.	9
2.1	Change in positions and velocities of atoms with time. The changes are marked only for one atom.	15
2.2	Graphical representation of the microcanonical (NVE) ensemble, the canonical (NVT) ensemble and the isothermal-isobaric (NPT) ensemble.	18
2.3	Graphical representation of the MD simulation procedure.	20
2.4	The system used to investigate the cut-off effect.	24
2.5	Effect of the cut-off function on the fracture simulations of the C-C bond.	25
2.6	Contribution from E^{REBO} , E^{LJ} , and E^{tors} on the strain energy under uniaxial tensile test.	27
2.7	Stress-strain curve of a graphene sheet obtained from MD simulations with different time steps.	29
2.8	Graphical representation of the periodic boundary conditions.	31
2.9	Graphene sheet used to demonstrate the simulation procedure in LAMMPS.	33
2.10	Simulation procedure in LAMMPS.	34
2.11	Change in the potential energy with time.	35
2.12	Various methods of rendering available in VMD	36
3.1	Graphene sheet used to study temperature effects.	40

List of Figures

3.2	The variation of the potential energy of a graphene sheet with relaxation time at 300 K.	40
3.3	Ripples of graphene sheet at 300 K and 800 K.	43
3.4	Variation of the normalized strain energy (U) with strain up to the fracture of graphene sheet at different temperatures. .	45
3.5	Variation of the potential energy of an armchair graphene sheet with strain.	46
3.6	Change in potential energy of a bond with bond length at 0 K.	47
3.7	Comparison of armchair and zigzag graphene sheets at a temperature of 300 K.	50
3.8	Stress-strain curves of arm-chair and zigzag graphene sheets at different temperatures.	52
3.9	Comparison of virial stress and continuum stress of a zigzag graphene sheet at 300 K.	54
3.10	Effect of temperature on ultimate stress and strain of graphene sheets.	56
3.11	Comparison of the change in Young's modulus of graphene sheets with temperature.	57
3.12	Nucleation of fracture of graphene sheet at 300 K	58
3.13	The smallest graphene sheet used for the study.	59
3.14	Variation of initial strain of graphene sheets with width. . . .	60
3.15	Comparison of initial strain of graphene sheets with width given by MD and Eq. (3.14)	62
3.16	Buckling of an armchair graphene sheet due to edge force. . .	63
3.17	Potential energy variation of the atoms with the distance from the edge.	64
3.18	Variation of strain energy with strain of graphene sheet with different widths at 1 K.	66
3.19	Variation of potential energy of atoms of armchair graphene sheet at different strains.	67
3.20	Variation of potential energy of atoms of zigzag graphene sheet at different strains.	68

List of Figures

3.21 Stress strain curves of graphene sheet with different widths at 1 K.	70
3.22 Ultimate stress and strain of graphene sheets with different widths at 1 K.	71
3.23 Change of E and D with width of graphene sheet at 1 K.	72
3.24 E vs width of graphene sheet at 1 K.	73
3.25 Stress strain curves of graphene sheet at 300 K.	75
3.26 Ultimate stress and strain of graphene sheets with different widths at 300 K.	76
3.27 Change of E and D with width of graphene sheet at 300 K.	77
3.28 Armchair and zigzag CNTs with a diameter of 24 Å.	78
3.29 Comparison of armchair and zigzag CNTs with diameters of 24 Å.	79
3.30 Stress strain curves for CNTs with different diameters.	80
3.31 Change of E and D of CNTs with different diameters.	81
4.1 Different sizes of square graphene sheets used to investigate the effect of finiteness.	84
4.2 σ - ε relation of square graphene sheets with various sizes and a crack of width 1.4 nm in the centre.	85
4.3 Crack length (2a) and crack tip radius (ρ) graphene sheets.	85
4.4 Stress - strain curve for graphene sheets with crack length.	87
4.5 Comparison of ultimate strength of graphene at various crack lengths.	88
4.6 Fracture of armchair graphene sheet. Strain has been applied along x direction.	89
4.7 Fracture of zigzag graphene sheet. Strain has been applied along y direction.	90
4.8 Ripples in defective graphene sheet. Strain has been applied along y-direction.	91
4.9 Parameters of an elliptical crack.	92
4.10 Calculation of γ_s	95
4.11 Comparison of Inglis' and Griffith's theories with MD.	96

List of Figures

4.12 Comparison of modified Inglis' and Griffith's theories with MD simulations.	98
4.13 Square-root singularity of the strength of graphene.	99

List of Symbols

E	Young's modulus
D	Third order elastic modulus
σ	Stress
ε	Strain
C	Carbon
N	Number of atoms
V	Volume
T	Temperature in Kelvins
P	Pressure in Pascal
U	Strain energy
γ_s	Surface energy density
$2a$	Crack length
ρ	Crack tip radius
\AA	Angstrom
r	Position vector
Δt	Time step
t	Time
v	Velocity
k_B	Boltzmanns constant
m	Mass
f	Force
A	Area

List of Abbreviations

MD	Molecular dynamics
QSMD	Quasi-static molecular dynamics
MM	Molecular mechanics
VMD	Visual molecular dynamics
PBC	Periodic boundary conditions
CTE	Coefficient of thermal expansion
CNT	Carbon nanotube
GNR	Graphene nanoribbons
AFM	Atomic force microscope
AFEM	Atomic-scale Finite Element Method
SEM	Scanning electron microscope
TEM	Trans- mission electron microscope
NEMS	Nano-electromechanical system
DFT	Density functional theory
REBO	Reactive empirical bond order
AIREBO	Adaptive intermolecular reactive empirical bond order
NVE	Constant number of atoms (N), volume (V), and energy (E) ensemble
NVT	Constant number of atoms (N), volume (V), and temperature (T) ensemble
NPT	Constant number of atoms (N), pressure (P), and temperature (T) ensemble
LAMMPS	Large-scale atomic/molecular massively parallel simulator

Acknowledgements

I would like to express my heartfelt gratitude to my supervisors, Professor Nimal Rajapakse and Dr. Srikantha Phani, whose patient guidance and continuous support enabled me to complete this thesis. Their influence has helped me to shape my thinking and observe the world with a new insightful perspective. I thank my colleagues for healthy discussions and for creating a friendly research atmosphere in the Dynamic and Applied mechanics Laboratory.

Financial support from Natural Sciences and Engineering Research Council of Canada (NSERC) is thankfully acknowledged.

To My Parents

Chapter 1

Introduction

1.1 Nanotechnology

Nanotechnology is the creation and utilization of materials and devices through the control of matter at the scale of nanometers. Nanometer (nm) is a one billionth of a meter; diameter of a human hair is 100,000 nm. Control of matter on the nanoscale has already made a significant advancement in many scientific disciplines such as physics, chemistry, materials science, biology, medicine, and engineering [1].

A lecture given by Richard Feynman in 1959 is considered to be the first scientific discussion on nanotechnology [2]. Invention of scanning tunnelling microscopy (STM) in 1982 [3] and atomic force microscopy (AFM) in 1986 [4] accelerated the research at nanoscale. Both STM and AFM were discovered by a group of researchers IBM, lead by Gerd Binnig. Binnig and Heinrich Rohrer were awarded the Nobel Prize in Physics in 1986 for the invention of STM. These inventions gave the researchers ability to observe individual atoms and manipulate them, which lead Harold Kroto, Robert Curl, Richard Smalley, and Sean Ó'Brien to discover the buckyball, which is a molecule, resembling a soccer ball in shape, and composed entirely of carbon. The team was awarded the 1996 Nobel Prize in Chemistry for their discovery [5]. Another great leap in nanotechnology is the discovery of carbon nanotube by Sumio Iijima in 1991 [6]. Iijima was awarded the Kavli Prize in Nanoscience in 2008 for this advance in the field.

At nanoscale, the quantum effects become important and material properties are size-dependent. When particle size approaches nanoscale, properties such as melting point, electrical conductivity, magnetic permeability, and chemical reactivity change as a function of the size of the particle.

1.2. Graphene

Nanoscale materials have larger surface area compared to area of the material at macroscale for a given volume. The reactivity of the material increases as surface area increases so that nanomaterial can be effectively used as catalyst [1].

Nanotechnology has made many advances in biology and medicine. Researchers are working on designing tools, treatments, and therapies that are more precise than conventional ones [7]. Researchers have discovered that in photosynthesis, the energy from sunlight is instantly transferred to the place where photosynthesis occurs by quantum mechanical processes with nearly 100% efficiency [8]. Growing understanding of nanoscale biomolecular structures is also impacting other fields than medicine. Some scientists are looking at ways to use nanoscale biological principles of molecular self-assembly, self-organization, and quantum mechanics to create novel computing platforms [9–11].

Recently, researchers were able to manipulate a single atom in a way they want [11, 12], which will lead researchers to fabricate devices by manipulating atom by atom. Isolation of a single layer graphene sheet from bulk graphite started a new research front in nanotechnology [13].

1.2 Graphene

Graphene is a flat monolayer of carbon atoms arranged into a two-dimensional (2-D) hexagonal lattice. One millimetre of graphite consists of three million layers of graphene, stacked on top of one another. These layers are held together by weak Van der Waals forces, therefore fairly easy to separate. Graphene is the basic building block of 0-D fullerene and 1-D carbon nanotube. Graphene was presumed not to exist in the free state, until Geim and Novoselov isolated free-standing graphene for the first time in 2004 [13]. Geim and Novoselov were awarded the 2010 Nobel prize in Physics for this discovery.

Graphene has been studied for more than sixty years [14]. Graphene has been found to be the strongest and stiffest material ever measured [15]. It has been experimentally found that the ultimate tensile strength (σ_{ult}) of

1.3. Nanomechanics

graphene is 130 GPa and its Young's modulus is 1 TPa [15]. The corresponding values of high carbon steel are ≈ 1 GPa and ≈ 200 GPa, respectively. It is about hundred times stronger and five times stiffer than the strongest steel. Also, thermal and electrical conductivities of graphene are much better than those of diamond and copper, respectively [16]. Researchers have demonstrated that graphene can be effectively used in structural applications. As an example, graphene is considered to be an excellent filler for composite materials [17–21]. There is also a growing interest in graphene as a base material for nano-electromechanical systems (NEMS) [22–25], given that lightness and stiffness are the essential characteristics sought in NEMS for sensing applications. Graphene-based resonators offer low inertial masses and ultra high frequencies.

Researchers have developed a number of different methods to produce graphene. Single and few-layer graphene have been grown epitaxially by chemical vapour deposition of hydrocarbons on metal substrates [26] and by thermal decomposition of SiC [27]. In the absence of quality graphene wafers, many researchers are currently using graphene samples obtained by micromechanical cleavage of bulk graphite, which is the technique that allowed for the isolation of graphene for the first time [13]. This technique provides high-quality graphene crystallites of up to $100\ \mu\text{m}$ in size, which is sufficient for most research purposes.

Fundamental understanding of the mechanical behavior of graphene is required for successful design and manufacture of devices such as graphene based resonators. The following section gives an overview of the different methods available to study the nanoscale materials such as graphene, and systems such as graphene based transistors.

1.3 Nanomechanics

Nanomechanics is a new area of mechanics which studies the properties and behaviour of nanoscale materials and structures. A structure with at least one dimension less than 100 nm is considered to be a nanostructure. A thorough understanding of the mechanical behaviour of nanoscale materials

1.3. Nanomechanics

is necessary to design and fabricate nanostructures. This has been achieved in nanomechanics by experimental studies and theoretical models. Transmission electron microscope (TEM), scanning electron microscope (SEM), and atomic force microscope (AFM) are widely used for experiments at nanoscale. TEM was used to find the ultimate strength of multiwalled carbon nanotubes [28]. AFM has been used to investigate the elastic properties and strength of graphene [15]. Conducting experiments at nanoscale is very expensive and time consuming. Therefore, theoretical models play a vital role in nanomechanics.

Nanomechanic models can be divided into three branches, such as *ab-initio* approaches, semi-empirical methods, and modified continuum models as shown in Fig. 1.1. *Ab-initio* (first principal) approaches, such as Hartree-Fock method and density functional theory (DFT) are considered to be more accurate than other methods to obtain the characteristics of nanoscale structures since these *ab-initio* approaches start with the basic equation for the entire system. As an example, Hartree-Fock method starts with Schrödinger equation of the system, which considers all quantum many-body interactions [29]. DFT is not as intense as Hartree-Fock method, and can be used for nanostructures containing up to a couple of hundreds to thousands of atoms [30] depending on the approximation used in the theory. However, the analysis of even a couple of hundred of atoms is not possible without the aid of super computers. Therefore, *ab-initio* approaches are not efficient to analyze large nanostructures such as graphene sheets, which can contain couple of thousand of atoms.

Semi-empirical methods, such as molecular dynamics (MD) and tight-binding method, are much more computationally affordable compared to *ab-initio* approaches and give quite accurate results [31]. MD is the most commonly used semi-empirical method. It assumes atoms as interacting classical particles and the interactions between atoms are described using molecular mechanics force fields. A detailed description about MD is given in Chapter 2. Tight-binding method uses a linear combination of the wave function of the neighbouring atoms to obtain the solution of a system of atoms [32]. Even though semi-empirical methods are computationally affordable, it is

1.3. Nanomechanics

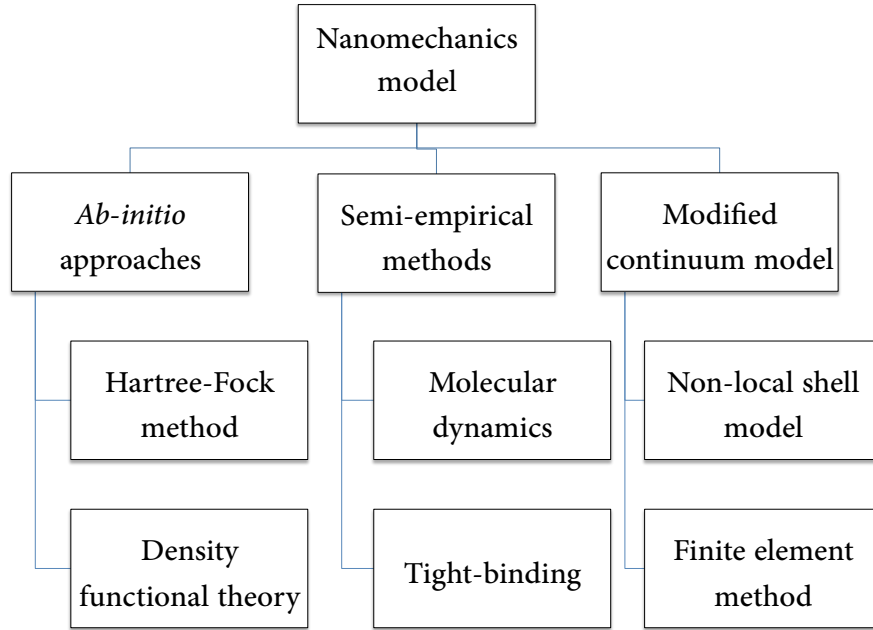


Figure 1.1: Some example of nanomechanical models.

expensive to conduct these calculations for all possible cases when designing nanostructures. To overcome this problem, researchers have used continuum models for basic level design calculations to get an overall idea of the behaviour of nanostructures, and then use semi-empirical methods or *ab-initio* calculations depending on the required level of accuracy and the available computational power.

A number of modified continuum models, such as non-local shell model, surface elasticity model, and finite element models, have been used to predict the behaviour of nanostructures. These models are not as accurate as the semi-empirical methods, but computationally very efficient. Non-local shell model has been successful in explaining the mechanics of carbon nanotubes, such as torsional behaviour [33], buckling [34, 35], vibration [36], and wave propagation [37–39]. The surface elasticity theory has been effectively used to study the effects of surface energy on the elastic behavior of nanotubes

1.3. Nanomechanics

and nanowires [40, 41] and effects on the resonance frequency and surface buckling of micro cantilever beams [42–45].

Molecular mechanics based finite element models have been used by researchers to predict the behaviour of nanostructures [46]. In these approaches, carbon-carbon (C-C) bonds are modelled as spring elements or beam elements as shown in Fig. 1.2. Mechanical properties of these elements are evaluated by considering the strain energy equivalence of structural mechanics and molecular mechanics [47]. In molecular mechanics, change in bond angles contribute to the stored strain energy of a system. Researchers have used various approaches to take this into account in molecular mechanics based finite element models.

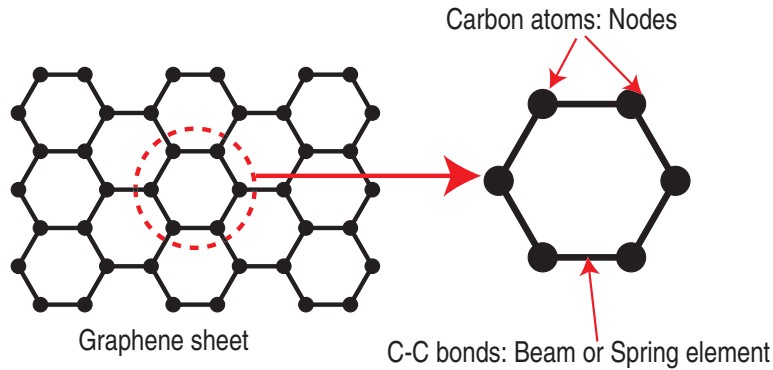


Figure 1.2: Bond based finite element method.

Odegard *et al.* [48] modelled C-C bond as a translational spring element. This simple model can only be applied when graphene sheet is subjected to an infinitesimal deformation. Meo and Rossi [49] modelled the angle between two adjacent C-C bonds using the relative rotation of the bonds. They used translational spring elements to model bonds. Nasdala and Ernst [50] presented a four-node finite element consisting of bond stretch, valence angle and dihedral angle change of C-C bonds. This element has been applied to investigate the mechanical behavior of carbon nanotubes, and it was found to be computationally expensive compared to other molecular mechanics based finite element methods [51]. Tserpes and Papanikos modelled C-C bonds

1.3. Nanomechanics

using three-dimensional elastic beam elements [47]. Length to diameter ratio of the beam element used in this study is 0.97, which indicates that the modelling of C-C bonds as beams is not appropriate.

Liu *et al.* [52, 53] proposed a new molecular mechanics based finite element method, which they named as atomic-scale finite element method (AFEM). This method does not have any assumption on the nature of the bonds and also considers the contributions from nearest and second nearest neighbouring atoms, which automatically consider the change in bond angles. Two AFEM elements needed to analyse a graphene sheet are shown in Fig. 1.3. The central atom (labelled as 1) of each element interacts with three nearest neighboring atoms (2 - 4) and six second nearest neighbors (5 - 10). Stiffness matrix is obtained from a molecular mechanics force field [52, 53].

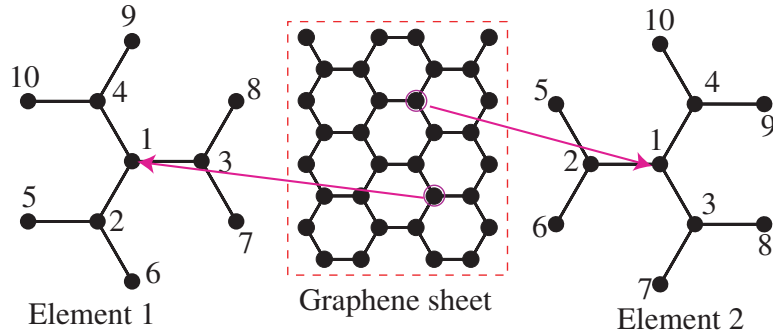


Figure 1.3: Elements of atomic-scale finite element method.

Continuum mechanics methods are only applicable to study the mechanics of infinitely large systems. However, in a system such as graphene, the discreteness of atoms and large surface area lead to scale effects, which cannot be explained using classical continuum mechanical methods [34]. Geometric effects of graphene, such as edge effects and defects arise due to finiteness and imperfectness of the atomic lattice. These effects need more sophisticated analyses to understand the influence on mechanics of graphene. Mechanics of an infinitely large perfect lattice can be investigated using classical continuum methods, however these continuum method should take into

account the discreteness of the atomic lattice and the results should be verified using a more refined atomistic simulations.

Researchers have used nanomechanics to study the mechanics of carbon nanotubes and graphene. Detailed literature survey on the use of nanomechanics to study the mechanics of geometric effects of graphene will be presented in the following sections.

1.4 Mechanics of Geometric Defects of Graphene

Edges and defects are the two main geometric effects that alter the mechanical properties of graphene. A thorough understanding of these effects is required for the design and manufacturing of graphene based nano devices.

1.4.1 Edge Effects

Graphene has two principal edge configurations, namely, armchair and zigzag as shown in Fig. 1.4. It has been experimentally observed that zigzag edge is more stable compared to armchair edge due to the edge configuration [54] due to the bonding environment of the edge atoms. It can be seen in Fig. 1.4 that armchair edge has bonds between two unstable edge atoms, which have only two C-C bonds. Combinations of these two basic configurations create a number of other edge configurations. Theoretical studies have indicated that both electronic and mechanical properties of graphene depend on the edge configuration [55–57]. Each carbon atom of the zigzag and armchair edges has an unpaired electron, which makes the edge atoms unstable. These unstable edge atoms alter the mechanical and electronic properties of the graphene sheet. Previous theoretical studies have shown that the effects of edges are prominent at lower widths [58, 59]. Researchers have used very narrow graphene sheets (width \approx 15 nm) for experiments on graphene based transistors [60]. Also, it has been suggested that elastic deformation of graphene can be used to tune the electronic structure and transport characteristics in graphene based devices [59, 61, 62]. Therefore, a deep understanding of the effects of edges is essential in order to design graphene

1.4. Mechanics of Geometric Defects of Graphene

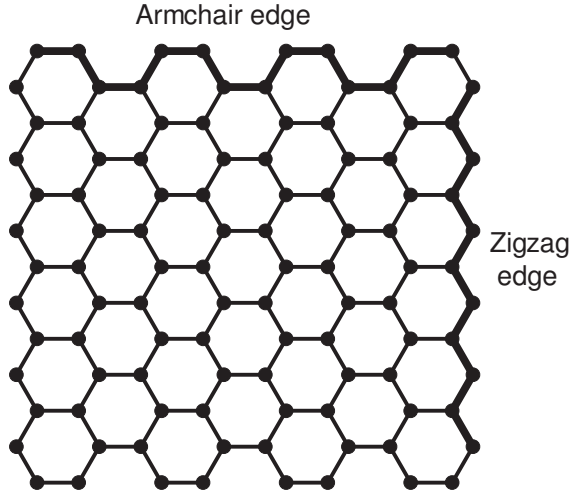


Figure 1.4: Armchair and zigzag edges of a finite graphene sheet.

based electromechanical systems.

Researchers have used various theoretical models, such as DFT, molecular mechanics, MD, and FEM to investigate the effects of edges on the mechanical properties of finite graphene sheets. Shenoy *et al.* [63] have studied the effect of edge stress on warping of graphene sheets, using MD simulations and a finite element model. They showed that edge stresses introduce ripples in freestanding graphene sheets, even without any thermal effect. Reddy *et al.* [64], using MD simulations, showed that the edge effect strongly influences the elastic properties of graphene with smaller widths (less than 8 nm). Zhao *et al.* [58] studied the change in Young's modulus of graphene nanoribbons (GNRs) with size and chirality, using the orthogonal tight-binding method and MD simulations. Their results indicate that Young's modulus of graphene increases with the increasing diagonal size of an approximately square graphene sheet. They also found that the fracture strain and fracture strength of bulk graphene under uniaxial tension heavily depend on the chirality. Ricardo *et al.* [59] studied the mechanical properties of GNRs using DFT, and found that both Young's modulus and shear modulus of GNR decrease with increasing width and attain the values of graphene. Quing *et al.* [65] used molecular mechanics simulations to

1.4. Mechanics of Geometric Defects of Graphene

determine the effect of edges on the equilibrium configuration. They found that compressive edge forces could cause GNRs to extend along the longitudinal direction and induce buckling in GNRs. Hao *et al.* [66] studied the mechanical behaviour of armchair GNRs using MD simulations. According to their observation, Young's modulus increases with width up to 4 nm and thereafter attains the value that of bulk graphene. Qiang *et al.* [62] studied the effect of edge structure on the mechanical behaviour of graphene sheets using molecular mechanics simulations. They observed that the initial Young's modulus decreases with increasing width in both types of GNR up to 6 nm and then reaches the value of bulk graphene. This observation is in contradiction to what was observed in [66]. This may be due to different potential fields used in the two simulations. Tersoff potential was used in [66] while reactive empirical bond-order (REBO) was used in [62]. Also, those simulations were done at difference temperatures. Simulations in [66] were done at 300 K, while the simulation temperature is 0 K in [62].

Researchers have studied effects of edges on mechanical behaviour of graphene using different methods as summarized above. However, the effect of temperature on edges has not been studied.

1.4.2 Defects

As in many crystalline materials, defects play a vital role in the effective material properties of graphene. Defects, such as Stone-Wales defect, vacancy defects, adatoms, dislocations and edge defects degrade the mechanical and electronic properties of graphene [67]. These defects can arise during the growth or during device production stages. Vacancy defect is the absence of carbon atoms in a graphene sheet, and it has been found that vacancy defect has greater influence on the mechanical properties of graphene compared to other types of defects [68]. Researchers have observed vacancy defects in graphene using TEM [69, 70]. The influence of vacancy defects on the mechanical properties of graphene has not yet been studied experimentally. However, a number of theoretical studies have been conducted on the effect of defects.

1.4. Mechanics of Geometric Defects of Graphene

Khare *et al.* [71] studied the effects of large defects and cracks on the mechanical properties of carbon nanotubes and graphene sheets using a coupled quantum mechanical/molecular mechanical method. They found that the weakening effects of holes, slits, and cracks vary only moderately with the shape of the defect, and instead depend primarily on the cross section of the defect perpendicular to the loading direction and the atomic structure near the fracture initiation point. Ansari *et al.* [68], using molecular dynamics simulations, showed that the presence of defects significantly reduces the ultimate strength and strain of graphene, while it has a minor effect on Young's modulus. They also showed that graphene is stronger in the armchair direction and defects have a lower effect in this direction compared to zigzag direction. Wang *et al.* [72] studied the effect of defects on the fracture strength of graphene sheets using molecular dynamics. They found that vacancies can cause significant strength loss in graphene and also concluded that the fracture strength is affected by temperature and loading directions. Pugno *et al.* [73, 74] introduced a new fracture mechanics concept called quantized fracture mechanics, which substitute the differentials in Griffith's energy balance [75] with finite differences in order to take into account the underlying crystal structure. The examples in [73, 74] show that this new fracture mechanics concept works well for discrete atomic systems. However, none of the previous studies [67, 68, 71, 72] have investigated the effect of the length of a vacancy defect (crack length) on the mechanical properties of both armchair and zigzag graphene sheets. It is also important to understand the mechanical behaviour of defects at different temperatures, which has not been investigated yet.

Even though the fracture is a very complex concept at macroscale, cracks simply propagate by breaking individual bonds at nanoscale. So the study of the fracture of graphene sheet, which is one atom thick 2-D sheet, may give an insight into the fracture of brittle materials at macroscale.

1.5 Scope of Current Work

Based on the above introduction and literature survey, it is seen that a thorough understanding of the mechanics of graphene is required to exploit the full potential of graphene. Geometric effects such as defects and edge effects degrade the mechanical properties of graphene. The ability of continuum models to capture such geometric effects at nanoscale is questionable. This motivates the use of MD simulations to study the geometric effects.

Two main objectives have emerged based on the literature review. The first is to investigate the effect of temperature and edges on the mechanical properties of graphene. The second is to study the effect of defects on the mechanical properties. Both studies have been conducted using MD simulations.

Chapter 2 gives a comprehensive description of MD. A detailed description about MD simulator (LAMMPS) and visualizer (VMD) is also presented. The effect of default cut-off function of reactive empirical bond order (REBO) potential on the fracture simulations of a graphene sheet is also investigated. Chapter 3 presents a study of the effects of temperature and edges on the mechanical properties of graphene. Also, the edge effect of graphene is compared with the effect of curvature on the mechanical properties of carbon nanotubes. In Chapter 4, a detailed study of the effects of vacancy defects on the mechanical properties of graphene at various temperatures is presented. Applicability of classical continuum fracture mechanics to predict the ultimate strength of defective graphene sheets is also investigated. Chapter 5 summarize the conclusions from the present work and indicates scope for future work.

Chapter 2

Molecular Dynamics Simulations

2.1 Introduction

Molecular dynamics (MD) is a mechanics based computer simulation method in which the time evolution of a set of interacting atoms is followed by integrating their equations of motion. The integration is done by solving Newton's equations of motion, numerically, and the interactions between the atoms are defined by molecular mechanics potential fields. The method was originally conceived by theoretical physicist in the late 1950s [76]. This chapter reviews the theory behind MD and one of the most commonly used MD simulators called large-scale atomic/molecular massively parallel simulator (LAMMPS) and a MD visualization software called visual molecular dynamics (VMD).

2.2 Basic Theory

2.2.1 Equation of Motion

Molecular dynamics can be divided into two basic steps. The first step involves the determination of the interacting forces between a system of atoms using molecular mechanics potential field. The second is the tracing of the movements of atoms by integrating Newton's equation of motion. The interacting force between atoms are obtained from the gradient of a molecular mechanics (MM) potential field. The force acting on atom i (f_i) is given by [31]

2.2. Basic Theory

$$f_i = -\frac{\partial E_i}{\partial r_i}, \quad (2.1)$$

where E_i and r_i are the potential energy and position of atom i , respectively. Potential energy of atoms is given by a MM potential field. There are a number of MM potential fields that are suitable to simulate various systems. Section 2.3 gives an overview of the MM potential fields. Once the force acting on an atom is known, it is possible to find the acceleration of the atom using Newton's second law, which is given by

$$f_i = m_i \frac{d^2 r_i}{dt^2} = m_i a_i, \quad (2.2)$$

where m_i , r_i , and a_i are the mass, position, and acceleration of atom i , respectively.

A system of atoms are allowed to move under these accelerations for a time period called time step. The new positions and velocities of the atoms are obtained using a numerical integration method such as velocity Verlet method [31]. According to the velocity Verlet method,

$$v\left(t_0 + \frac{\Delta t}{2}\right) = v(t_0) + a(t_0) \frac{\Delta t}{2}, \quad (2.3a)$$

$$r(t_0 + \Delta t) = r(t_0) + v\left(t_0 + \frac{\Delta t}{2}\right) \Delta t, \quad (2.3b)$$

$$v(t_0 + \Delta t) = v\left(t_0 + \frac{\Delta t}{2}\right) + a(t_0) \Delta t, \quad (2.3c)$$

where r , v , and a are the position, velocity, and acceleration of an atom, respectively; t_0 is the initial time; Δt is the time step. Variation in r and v with Δt is graphically presented in Fig. 2.1.

Controlling temperature and pressure is necessary in MD simulations in order to simulate real systems which are under a constant temperature or pressure. The temperature control is achieved by modifying the velocities of atoms, while pressure is controlled by adjusting the size of the simulation

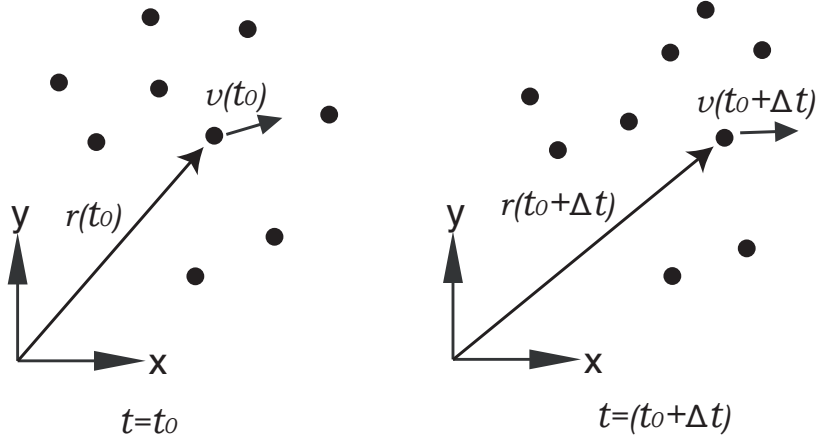


Figure 2.1: Change in positions and velocities of atoms with time. The changes are marked only for one atom.

box. A review of commonly used technique to control temperature and pressure follows next.

2.2.2 Temperature Control

Temperature of a system of atoms is defined as the average of kinetic energies of all particles. The instantaneous temperature can be given as

$$T = \frac{1}{N_f k_B} \sum_{i,\alpha} m_i (v_i^\alpha)^2, \quad (2.4)$$

where, N_f is the total translational degrees of freedom of the system, k_B is Boltzmann's constant, m_i is the mass of atom i and v_i^α is the velocity of atom α in i direction. The value of α can be 2 or 3 depending on the dimensionality of the system.

It is not possible to keep the temperature at a fixed value during the simulation due to the fluctuations in velocities. Therefore, only the average value of temperature can be maintained at a constant value during simulations. The temperature of a system depends only on the velocities of atoms as given in Eq. (2.4). Therefore, the temperature of a system can be controlled by scaling the velocities of atoms, which is achieved using a

2.2. Basic Theory

thermostat. Anderson, Berendson, and Nosé-Hoover thermostats are the most commonly used thermostats.

Anderson thermostat [77] is one of the simplest among the many available thermostats. In this thermostat, the velocity of a randomly selected particle is replaced by a value chosen from the Maxwell-Boltzmann distribution for a given temperature. However, Anderson thermostat has not been widely used since it is computationally expensive [78]. Berendson thermostat [79] is one of the most commonly used thermostats which is simple and easy to implement. Berendson thermostat scales the velocities of atoms in such a way that the total kinetic energy of the system is fixed.

The Nosé-Hoover thermostat, which has been used in this study, is considered to be one of the best thermostats [80]. Nosé-Hoover thermostat [81–84] uses a friction factor (μ) to modify the equation of motion, and μ is defined as

$$\frac{d\mu(t)}{dt} = \frac{N_f k_B}{Q} (T(t) - T_0), \quad (2.5)$$

where T_0 and $T(t)$ are the desired and the current temperatures, respectively; Q is the effective mass of the thermostat, which determines the strength of thermostat, and is given as

$$Q = N_f k_B T_0 \tau_T^2, \quad (2.6)$$

where τ_T is the specified time constant for temperature fluctuations. The value of τ_T is generally in the order of hundred time steps to achieve a smooth temperature transition.

The modified Newton's equation of motion is given by,

$$a = \frac{f(t)}{m} - \mu(t)v(t). \quad (2.7)$$

2.2.3 Pressure Control

The pressure of a system of atoms is defined as

$$P_{ij}^V = \frac{1}{V} \sum_{\alpha} \left[\sum_{\beta=1}^N \left(r_i^{\beta} - r_i^{\alpha} \right) f_j^{\alpha\beta} + m^{\alpha} v_i^{\alpha} v_j^{\alpha} \right], \quad (2.8)$$

where (i, j) are directional indices and β is an assigned number to the neighbouring atoms that goes from 1 to the number of neighbouring atoms N ; r_i^{α} is the position of atom α along direction i and $f_j^{\alpha\beta}$ is the force along direction j on atom α due to atom β ; m^{α} and v^{α} are the mass and velocity of atom α , respectively. V is the total volume of the system.

Berendsen barostat [79] and Nosé-Hoover barostat [85] are the most commonly used barostats to control pressure in MD simulations. In both these methods, the system pressure is adjusted by changing the dimensions of the simulation box during the simulation. However, it has been found that Berendson's approach is less reliable compared to Nosé-Hoover approach [80].

The volume scaling factor (η) in Nosé-Hoover barostat is defined as

$$\frac{d\eta(t)}{dt} = \frac{1}{N_f k_B T_0 \tau_P^2} V(t) (P(t) - P_0), \quad (2.9)$$

where P_0 and T_0 are instantaneous pressures and temperature, respectively; $P(t)$ is the desired and τ_P is the specified time constant for pressure fluctuations. The value of τ_P is generally on the order of thousand time steps to achieve a smooth temperature fluctuation. The adjusted volume of the system is calculated using η as

$$\frac{dV(t)}{dt} = [3\eta(t)]V(t). \quad (2.10)$$

2.2.4 NPT Ensemble

An ensemble is a collection of all the possible states of a real system. The microcanonical or constant N, V, and E (NVE) ensemble, the canonical (NVT) ensemble, and the isothermal-isobaric (NPT) ensemble are commonly used in MD. The abbreviations N, V, E, T, and P stand for the number of atoms, volume, energy, temperature, and pressure of the system, respectively and

2.2. Basic Theory

these quantities are kept constant during the simulation. As an example, the number of atoms, temperature, and pressure are constant in the NPT ensemble. Fig. 2.2 graphically shows the NVE, NVT, and NPT ensembles. Most of the experiments are being conducted under constant temperature and constant pressure (isothermal-isobaric) condition, which is represented by the NPT ensemble.

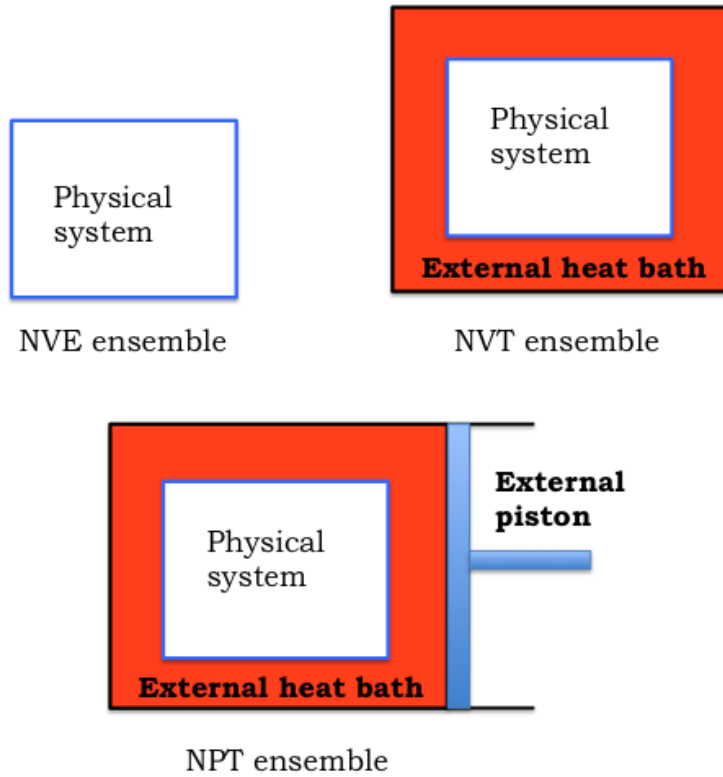


Figure 2.2: Graphical representation of the microcanonical (NVE) ensemble, the canonical (NVT) ensemble and the isothermal-isobaric (NPT) ensemble.

Combination of Nosé-Hoover thermostat and barostat generates the NPT ensemble [86, 87]. The modified equations of motion for the NPT ensemble

2.3. Potential Fields

can be expressed as

$$\frac{d\mu(t)}{dt} = \frac{1}{\tau_T^2} \left(\frac{T}{T_0} - 1 \right), \quad (2.11a)$$

$$\frac{d\eta(t)}{dt} = \frac{1}{N_f k_B T_0 \tau_P^2} V(t) (P(t) - P_0), \quad (2.11b)$$

$$\frac{dV(t)}{dt} = [3\eta(t)]V(t), \quad (2.11c)$$

$$\frac{dr(t)}{dt} = v(t) + \eta(r(t) - R_0), \quad (2.11d)$$

$$\frac{dv(t)}{dt} = \frac{f(t)}{m} - [\mu(t) + \eta(t)] v(t), \quad (2.11e)$$

where R_0 is the centre of mass of the system. All other parameters have been defined earlier.

The procedure of a MD simulation can be summarized as in Fig. 2.3. Initial positions of atoms should be defined in such a way that atoms are slightly away from their known equilibrium, so that the atoms will come to their equilibrium position over the relaxation time. Initial velocities of atoms are assigned randomly. Those velocities are rescaled by thermostat during the simulation to obtain the desired temperature. The loop shown in Fig. 2.3 runs until termination condition is met. The number of iterations is most commonly used as the termination condition.

2.3 Potential Fields

Potential field is a mathematical description of the potential energy of a system of interacting atoms. Parameters in potential fields are derived from both experimental work and high-level quantum mechanical calculations, so they are empirical in nature. Researchers have defined various potential fields to simulate various molecular systems such as bio-molecules, hydrocarbons, etc. The general form of a potential field can be expressed as

$$E_{tot} = E_{covalent} + E_{non-covalent}, \quad (2.12)$$

2.3. Potential Fields

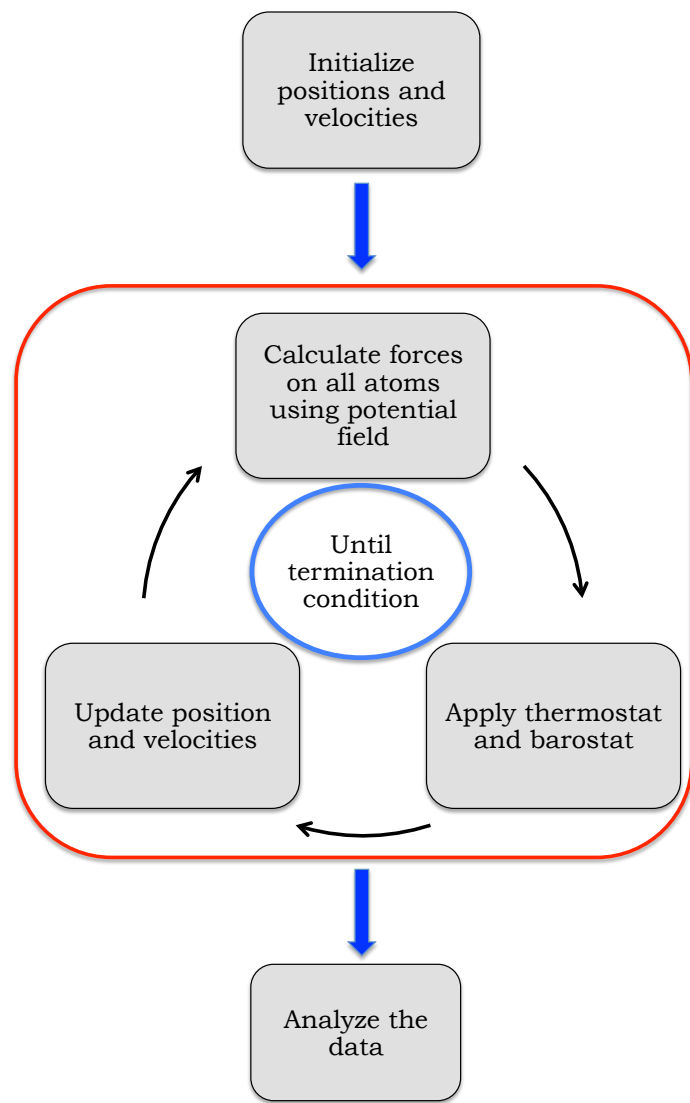


Figure 2.3: Graphical representation of the MD simulation procedure.

2.3. Potential Fields

where E_{tot} , $E_{covalent}$, and $E_{non-covalent}$ are the total energy, covalent energy, and non-covalent energy, respectively. The components of covalent and non-covalent energies can be further broken down as,

$$E_{covalent} = E_{bond} + E_{angle} + E_{dihedral} + E_{out-of-plane}, \quad (2.13a)$$

$$E_{non-covalent} = E_{electrostatic} + E_{Van\ der\ Waals}. \quad (2.13b)$$

The exact functional form of a potential field depends on the type of simulation, for which it has been made. All-atom potential fields provide parameters for every type of atom in a system, while united-atom potential fields provide parameters only for one or two types of atoms.

Researchers have used Morse potential field, reactive empirical bond order (REBO) potential field and adaptive intermolecular reactive empirical bond order (AIREBO) potential field to simulate graphene and carbon nanotubes [88]. Morse potential field is two body potential field, which does not represent the systems with many body interaction, such as graphene. The MD simulations in this study has been conducted using AIREBO and REBO potentials, which are many body potentials.

2.3.1 AIREBO Potential Field

AIREBO [89] potential field is an extension of the commonly used REBO [90] potential field. AIREBO addresses some of the short coming in the REBO potential. Absence of the non-bonded interaction in REBO potential makes it poorly suitable for systems with significant intermolecular interactions such as graphite. Even covalent material such as graphene is also benefited from intermolecular interactions [89]. AIREBO potential field takes non-bonded interactions into account. It also consider the four-body torsional interactions, which was not included in REBO potential. This torsional interaction become important when simulating curved structures such as carbon nanotubes. AIREBO potential consists of three parts that can be expressed as,

2.3. Potential Fields

$$E^{AIREBO} = \frac{1}{2} \sum_i \sum_{i \neq j} \left[E_{ij}^{REBO} + E_{ij}^{LJ} + \sum_{k \neq i,j} \sum_{l \neq i,j,k} E_{ijkl}^{tors} \right], \quad (2.14)$$

where E^{AIREBO} is the total potential energy of a system of atoms and indices i, j, k , and l refer to individual atoms; E_{ij}^{REBO} is the REBO part, which explains the bonded interaction between atoms; E_{ij}^{LJ} is Lennard-Jones potential that considers the non-bonded interactions between atoms; E_{ijkl}^{tors} includes the torsional interactions between atoms into the total energy.

The REBO part consists of the attractive and the repulsive potentials, which are combined using the bond order term as given in Eq. (2.15).

$$E_{ij}^{REBO} = f(r_{ij}) (V_{ij}^R + b_{ij} V_{ij}^A), \quad (2.15)$$

where E_{ij}^{REBO} is the energy stored in the bond between atom i and atom j ; b_{ij} is the bond order term, which modifies the strength of the bond depending on the local bonding environment; V_{ij}^R and V_{ij}^A are the repulsive and the attractive terms, respectively.

The function $f(r_{ij})$ in Eq. (2.15) is called cut-off function. The purpose of the cut-off function is to limit the interatomic interactions to the nearest neighbour [90]. However, the cut-off function can cause nonphysical behaviour in fracture simulation of carbon nanostructures [88, 91].

Cut-off Function

The originally suggested cut-off function in REBO potential field is given by

$$f(r) = \begin{cases} 1, & r < R^{(1)} \\ \left[1 + \cos \left[\frac{\pi(r-R^{(1)})}{(R^{(2)}-R^{(1)})} \right] \right] / 2, & R^{(1)} < r < R^{(2)} \\ 0, & R^{(2)} < r \end{cases} \quad (2.16)$$

where r is the bond length and $R^{(1)}$ and $R^{(2)}$ are cut-off radii, which have

2.3. Potential Fields

the values of 1.7 Å and 2 Å, respectively. Researchers have used modified cut-off radii ranging from 1.9 Å to 2.2 Å [62, 92] to eliminate the nonphysical behaviour in fracture simulations.

The stress-strain curves of a graphene sheet obtained with default cut-off function show a strain hardening around strain of 0.2 [56]. However, experiments [15] and *ab initio* calculations [93] have given smooth nonlinear stress-strain curve without any strain hardening. In order to further investigate the effect of cut-off function on the fracture simulations and also to find a suitable cut-off radii for the fracture simulations of graphene, potential energy of C-C bond between atoms 1 and 2 in Fig. 2.4 is numerically obtained with increasing bond length r . The relative positions of other atoms were kept unchanged. It was found that the non-physical behaviour in force-strain curve disappears when both the radii ($R^{(1)}$ and $R^{(2)}$) are equal to 2 Å. The effect of cut-off function on the potential energy-strain curve of the C-C bond between atoms 1 and 2 in Fig. 2.4 is shown in Fig. 2.5(a). It can be seen in Fig. 2.5(a) that the default cut-off function alters the potential energy of the bond around a strain of 0.22. This induces a non-physical behaviour in the force-strain curve as shown in Fig. 2.5(b).

It has been found that the fracture strength of a covalent material, such as graphene, primarily depends on the inflection point of the interatomic energy [88]. According to Fig. 2.5(b), inflection point is located around strain value of 0.22 with the modified cut-off radius. The inflection point is around 0.32 for the default cut-off radii due to a spurious strain hardening initiated around a strain value of 0.22. Therefore, bond breaking takes place around a strain value of 0.22 with the modified cut-off radius, while it takes place at a strain of 0.32 for the default radii. *Ab-initio* calculations have shown that the ultimate strains of graphene are 0.194 and 0.266 in armchair and zigzag directions, respectively [93]. On the other hand, the shape of the force-strain curve with modified cut-off function is similar to what have been observed in experiments [15] and *ab initio* calculations [93]. This confirms that the REBO potential with the modified cut-off function is able to simulate the fracture of a graphene sheet accurately, whereas default cut-off function is unable to do so.

2.3. Potential Fields

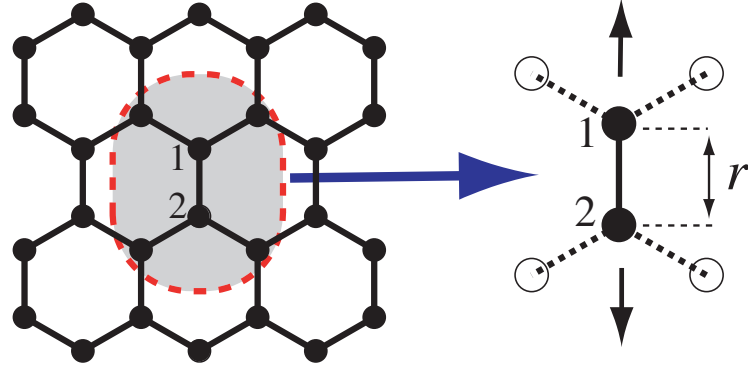


Figure 2.4: The system used to investigate the cut-off effect. The arrows indicates the straining direction and r is the initial bond length.

In this work, the cut-off function has been modified with a fixed cut-off radius of 2 Å. The modified cut-off function ($\tilde{f}(r)$) is given as

$$\tilde{f}(r) = \begin{cases} 1, & r < R \\ 0, & r > R \end{cases} \quad (2.17)$$

where R is the new cut-off radius, which is 2 Å.

Torsional and Non-bonded Interactions

The E_{ij}^{LJ} term in AIREBO potential takes into account the non-bonded interactions with a Lennard-Jones (LJ) 12-6 potential [94] as,

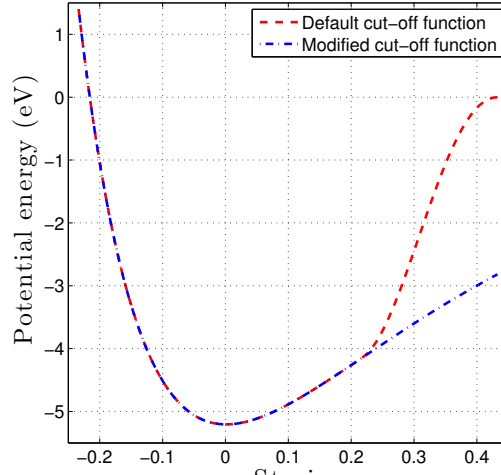
$$E_{ij}^{LJ} = f(r_{ij})V_{ij}^{LJ}(r_{ij}), \quad (2.18a)$$

$$V_{ij}^{LJ}(r_{ij}) = 4\epsilon_{ij} \left[\left(\frac{\sigma_{ij}}{r_{ij}} \right)^{12} - \left(\frac{\sigma_{ij}}{r_{ij}} \right)^6 \right], \quad (2.18b)$$

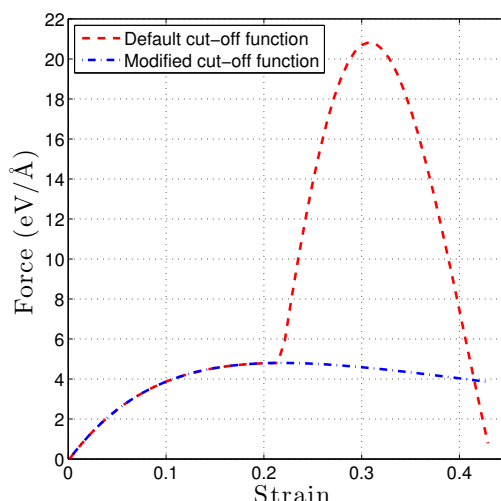
where the function $f(r_{ij})$ consists of a set of cut-off functions, which limits the non-bonding interactions to a certain range; ϵ_{ij} is the potential barrier; σ_{ij} is the finite distance at which the inter-particle potential is zero; r_{ij} is the distance between the atoms.

The last term of the AIREBO potential given in Eq. (2.14), and E_{ijkl}^{tors} ,

2.3. Potential Fields



(a)



(b)

Figure 2.5: Effect of the cut-off function on the fracture simulations of the C-C bond in Fig. 2.4. (a) Strain energy vs strain (b) The force strain curve.

gives the energy contribution from the four-body torsional interactions which

2.4. Molecular Dynamics Parameters

is defined as,

$$E_{ijkl}^{tors} = f(r_{ij}, r_{lk}, r_{kl}) V^{tors}(\omega_{ijkl}), \quad (2.19a)$$

$$V^{tors}(\omega_{ijkl}) = \epsilon \left[\frac{256}{405} \cos^{10} \left(\frac{\omega_{ijkl}}{2} \right) - \frac{1}{10} \right], \quad (2.19b)$$

where the function $f(r_{ij}, r_{lk}, r_{kl})$ consists of a set of cut-off functions, which depend on the bond lengths r_{ij} , r_{lk} and r_{kl} ; ω_{ijkl} is the dihedral angle.

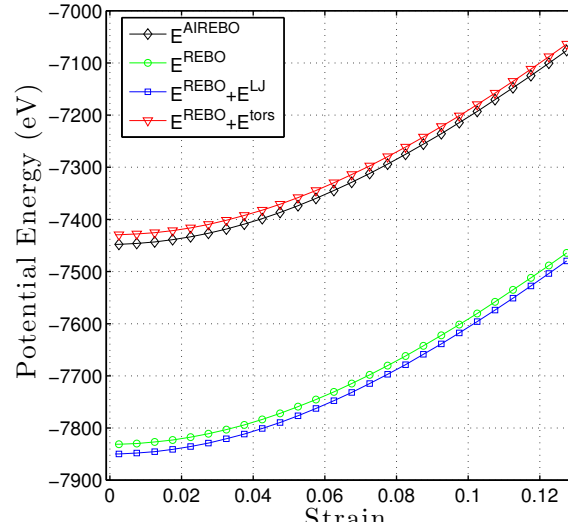
It is of interest to compare the contribution from the three parts (E^{REBO} , E^{tors} , and E^{LJ}) of AIREBO potential field towards the strain energy stored in a graphene sheet under the uniaxial tensile test. In order to investigate this, a set of MD simulations were performed on a graphene sheet of size 5 nm × 5 nm. The simulation temperature was 300 K. The time step and strain rate were 0.5 fs and 0.001 ps⁻¹, respectively. The LAMMPS MD simulator was used for all the simulations [95].

As shown in Fig. 2.6, the torsional potential (E^{tors}) has a significant amount of energy compared to non-bonded interaction (E^{LJ}) at unstrained state. However, neither E^{tors} nor E^{LJ} energies have changed with strain. The stress on the graphene sheet is calculated using the gradient of strain energy-strain curve. The thickness of the graphene sheet is assumed to be 3.4 Å. This comparison indicates that both E^{tors} and E^{LJ} do not have an effect on the stress-strain curve of graphene. In other words, AIREBO and REBO potentials give a similar stress-strain curve under the uniaxial tensile test. The torsional effect given by E^{tors} of AIREBO potential might be significant in curved structures such as carbon nanotubes.

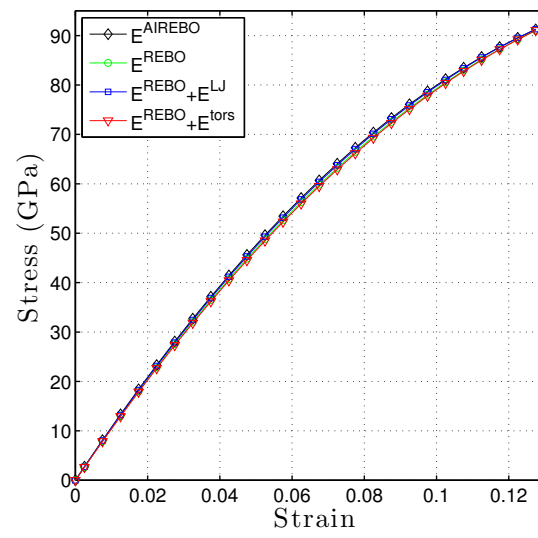
2.4 Molecular Dynamics Parameters

All the parameters mentioned in Section 2.2 except τ_T and τ_P are predefined parameters in MD simulator. In fact τ_T and τ_P also depend on the value of time step, so the user has only a partial control. However some MD parameters such as time step, strain rate, and boundary conditions are user

2.4. Molecular Dynamics Parameters



(a)



(b)

Figure 2.6: Contribution from E^{REBO} , E^{LJ} , and E^{tors} on the strain energy under uniaxial tensile test. (a) Variation of potential energy. (b) Stress-strain relation.

2.4. Molecular Dynamics Parameters

defined parameters. Selection of these parameter has an influence on the MD simulation results.

2.4.1 Time step

The time step is the length of time between two consecutive iterations in a MD simulation. Larger time steps increase the computational efficiency and smaller time steps may increase the accuracy of the simulation. Therefore, the time step controls the trade-off between accuracy and computational efficiency in a MD simulation. If a time step is chosen too large, the system might become unstable.

A time step should be less than 10% of the vibration period of an atom and, time step of 0.5 fs to 0.8 fs provides good results in carbon nanotube and graphene simulations [96]. However, researchers have used time steps from 0.1 fs to 1 fs to simulate uniaxial tensile tests of graphene [92, 97]. In fact, most of them have used AIREBO potential field implemented in LAMMPS MD simulator for the simulations. Therefore, it is of interest to investigate the effect of time step on the simulation of the uniaxial tensile test of graphene. In order to investigate this, a set of MD simulations were performed on a $5\text{ nm} \times 5\text{ nm}$ graphene sheet with time steps of 0.1 fs, 0.5 fs, and 1 fs. All other MD parameters were kept at the values mentioned in Section 2.3.1. The results indicate that the stress-strain curves of graphene obtained with different time steps are identical as shown in Fig. 2.7. This confirms that a time step between 0.1 fs and 1 fs could be used to simulate uniaxial tensile tests of graphene. A time step of 0.5 fs, which is the most commonly used value in literature, will be used in all the MD simulations hereafter.

2.4.2 Strain Rate

In MD simulations, a tensile test is performed by applying strain to the nanostructure at a constant strain rate. Researchers have found that the failure point of graphene depends on the strain rate [97–99]. At lower strain rates, the system has more time to relax and reach equilibrium state, and

2.4. Molecular Dynamics Parameters

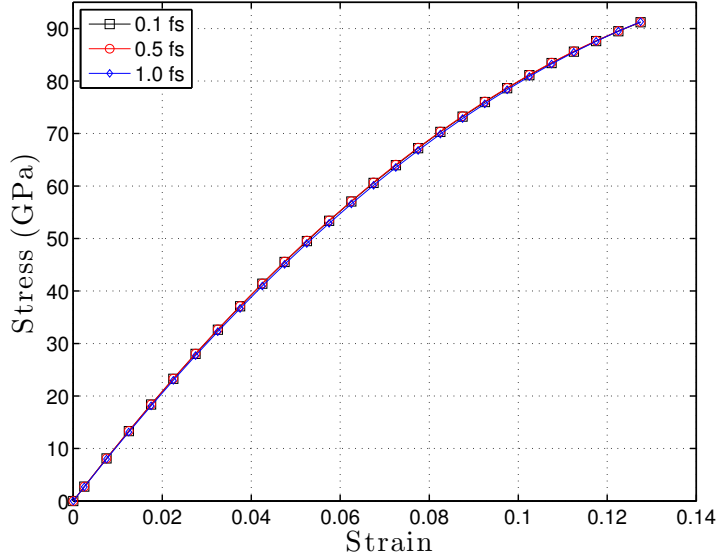


Figure 2.7: Stress-strain curve of a graphene sheet obtained from MD simulations with different time steps.

hence the results would be more accurate. Practical strain rates, used in experiments, such as 10^{-2} s^{-1} is not possible to simulate in MD simulations due to high computational time. As an example, in order to apply a strain of 0.1 on a graphene sheet at a strain rate of 10^{-2} s^{-1} , 2×10^{16} iterations with a time steps of 0.5 fs are required. Simulating 2×10^{16} iterations for a graphene sheet of size $5 \text{ nm} \times 5 \text{ nm}$, which is the size of graphene sheet has been used for the simulations presented in this chapter, could take around 10^6 years in a Mac with 3.06 GHz Intel Core i3 processor and 4 GB memory. Even, the use of super computers is not able to increase the computational speed more than four times of the above speed due to the communication time between cores. Therefore, in order to become computationally viable, strain rate of the order of 10^9 is generally used in MD simulations.

Researchers have used various strain rates ranging from 0.0005 ps^{-1} to 0.01 ps^{-1} [97]. In order to investigate the effect of strain rate on the failure point of graphene, a set of MD simulations were performed on a

2.4. Molecular Dynamics Parameters

graphene sheet of size $5 \text{ nm} \times 5 \text{ nm}$ under the strain rates of 0.01 ps^{-1} , 0.001 ps^{-1} , and 0.0001 ps^{-1} . A quasi-static MD (QSMD) simulation was also performed on the sheet. There is no strain rate in QSMD simulation [33]. In this method, the graphene sheet, which is under a certain applied strain, is allowed to reach equilibrium over 30 ps time, and potential energy of the system is obtained. All other MD parameters were kept at the values mentioned in Section 2.3.1. Table 2.1 shows that the strain rate does not affect the Young's modulus, however the higher strain rates result in higher ultimate stress (σ_{ult}) and higher ultimate strains (ϵ_{ult}). Even though the failure point depends on the strain rate, a fixed strain rate can be used to compare the stress-strain behaviour of graphene sheets under various conditions. The values of σ_{ult} , ϵ_{ult} , and E at strain rate of 0.0001 ps^{-1} agrees quite well with the values obtained from QSMD simulations. However, strain rate of 0.0001 ps^{-1} is computationally expensive. QSMD simulations are also computationally expensive since it required separate simulation at each strain. A strain rate of 0.001 ps^{-1} has been used in all the MD simulations presented hereafter, since it is computationally viable and the values of σ_{ult} , ϵ_{ult} , and E at this strain rate are within 6% of the values calculated from QSMD. On the other hand, 0.001 ps^{-1} is a commonly used strain rate in literature [58, 97].

Table 2.1: Dependence of mechanical properties of a graphene sheet on the strain rate.

Strain rate (ps^{-1})	ϵ_{ult}	$\sigma_{ult}(\text{GPa})$	$E(\text{TPa})$
0.01	0.143	94.9	1.109
0.001	0.133	92.8	1.105
0.0001	0.123	89.8	1.102
0 (QSMD)	0.125	90.5	1.159

2.4.3 Periodic Boundary Conditions

The effects of edges in 2-D systems such as graphene and surfaces in 3-D systems such as graphite should be eliminated in MD simulations in order to obtain the bulk properties of these systems. One way of doing this is by

simulating an extremely large system to ensure that the surfaces and edges have only a small influence on the properties. However, this approach is computationally expensive. The most efficient way to simulate an infinitely large system is the use of periodic boundary conditions (PBC). In PBC, the cubical simulation box is replicated throughout space to form an infinite lattice as shown for a 2-D case in Fig. 2.8. During the simulation, when a molecule moves in the central box, its periodic images in every other box also move in exactly the same way. Thus, as a molecule leaves the central box, one of its images will enter through the opposite face. Therefore the system has no edges.

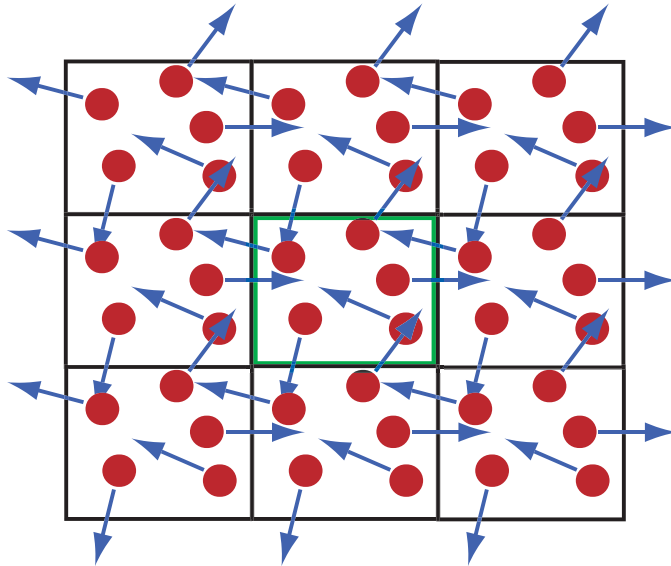


Figure 2.8: Graphical representation of the periodic boundary conditions of the middle box. The arrows indicate the velocities of atoms. The atoms in the middle box can interact with atoms in the neighbouring boxes without having any boundary effects.

2.5 Overview of LAMMPS

All the MD simulations presented in this thesis have been performed using large-scale atomic/molecular massively parallel simulator (LAMMPS) [95].

2.5. Overview of LAMMPS

LAMMPS is a free and open source software developed by Sandia National Laboratories. It can be used as a parallel particle simulator at the atomic, meso, or continuum scales [100].

A LAMMPS input script can be categorized into four parts, named as initiation, atom definition, settings, and running. Units and boundary conditions of the simulation are defined in the initialization part. Different unit systems, such as SI, cgs, metal, etc. are available in LAMMPS. Metal units are mandatory if AIREBO or REBO potential field is used for the simulation. In metal units, the units of distance, time and energy are Angstroms, picoseconds and electron-volts, respectively. Boundary conditions can be chosen as either periodic or non-periodic. The input file should be named as *in.filename*.

Coordinates (x, y and z) of the atoms and the atom types are defined under atom definition part. Atom coordinates can also be given in a different file, which is named as *data.filename*. This file is called when the input file (*in.filename*) is executed.

Potential field coefficients, simulation parameters and output options are defined in the third part. Over 70 potential fields and variations of potential fields have been implemented in LAMMPS. The basic simulation parameters, such as time step, temperature, pressure, etc. are defined here. Most of the pressure and temperature controlling methods, such as Berendsen and Nosé-Hoover methods are implemented in LAMMPS. Microcanonical (NVE) ensemble, canonical (NVT) ensemble and isothermal-isobaric (NPT) ensemble are also implemented. NPT ensemble uses Nosé-Hoover thermostat and barostat in order to control the temperature and pressure, respectively. LAMMPS allows to calculate time and spatial averages of physical quantities, such as temperature, pressure, energies, etc. The user is given the ability to get these quantities written in to a separate text files at specified time intervals.

The final part is running the simulation. LAMMPS allows to deform the simulation box while it is running. A nanostructure, which is being simulating, is attached to the simulation box. Therefore, the nanostructure also deforms with the simulation box. This gives user the ability to apply

2.6. Overview of VMD

strain at a constant strain rate into a nanostructure. Output of the simulation is written to a file named as *log.lammps* after pre-specified number of iterations.

2.5.1 Uniaxial Tensile Test in LAMMPS

To demonstrate the simulation procedure of LAMMPS, uniaxial tensile test has been performed on graphene sheet shown in Fig 2.9. Size of the graphene sheet is $49.6 \text{ \AA} \times 11.2 \text{ \AA}$ with 252 carbon atoms. The simulation temperature is 300 K. Graphene sheet is allowed to relax for 30 ps before applying strain. The strain rate and time step were 0.002 ps^{-1} and 0.5 fs, respectively.

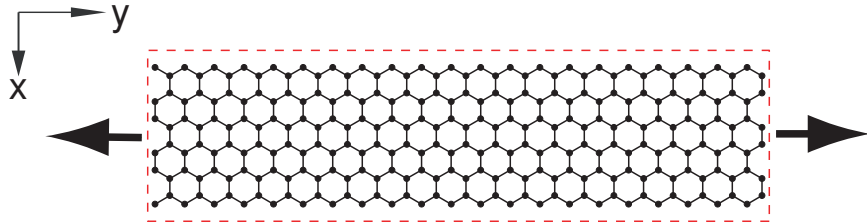


Figure 2.9: Graphene sheet used to demonstrate the simulation procedure in LAMMPS. The dashed box indicates the boundaries of the simulation box. The arrows indicate the straining direction.

The simulation procedure is graphically shown in Fig. 2.10. LAMMPS input files *in.graphene* and *data.graphene*, and the output file *log.lammps* are given in Appendix A.

One of the most important output from MD simulation is the potential energy of the graphene sheet. Variation of potential energy of the sheet with time is shown in Fig. 2.11. Potential energy is almost constant during the relaxation period (up to 30 ps) and then start to increase with the applied strain with a strain rate of 0.002 ps^{-1} .

2.6 Overview of VMD

Visual molecular dynamics (VMD) [101] has been used for the visualization of MD simulations presented in this thesis. VMD is a free and open source

2.6. Overview of VMD

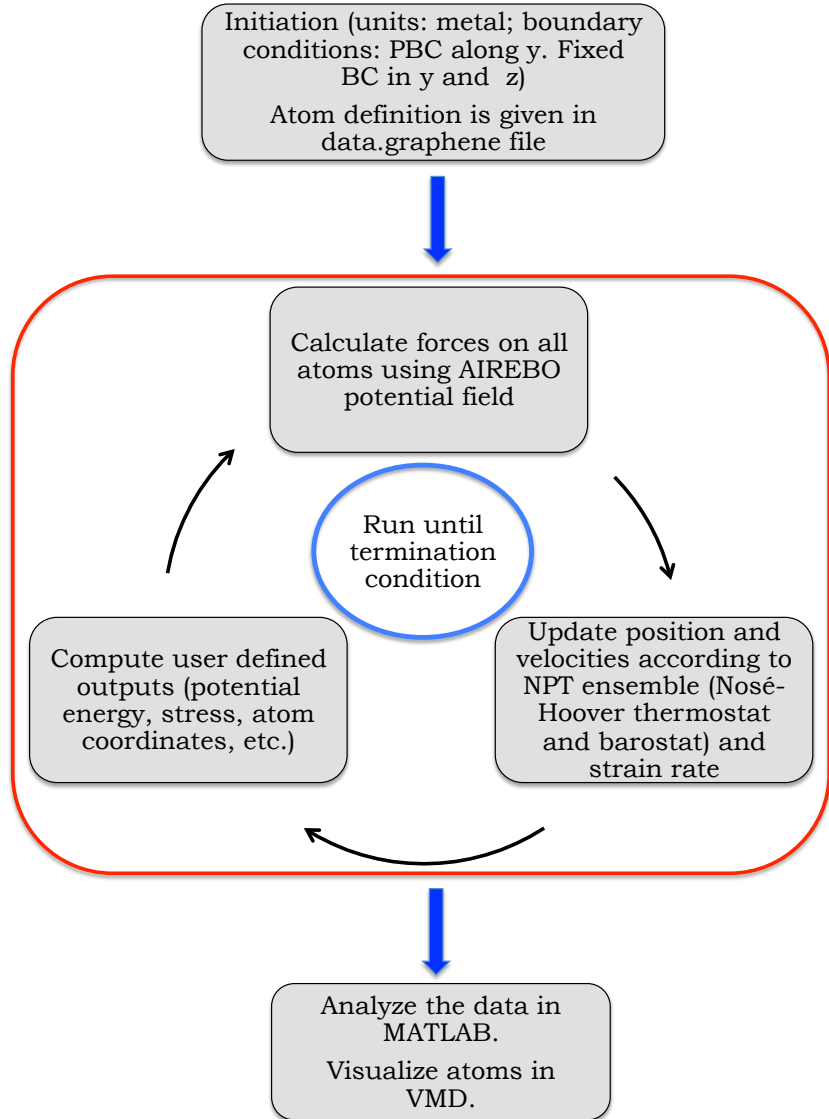


Figure 2.10: Simulation procedure in LAMMPS.

software developed by theoretical and computational biophysics group at University of Illinois. It supports over 60 molecular file formats including LAMMPS output files [102]. VMD provides a wide variety of methods for rendering and colouring a molecule, such as simple points-lines method and

2.7. Conclusions

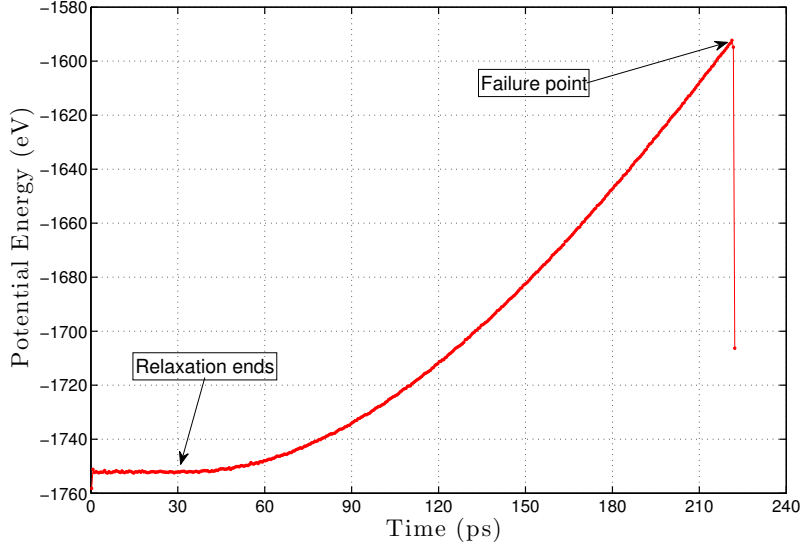


Figure 2.11: Change in the potential energy with time.

spheres-cylinders method, etc.

VMD was used to animate the trajectories of the MD simulations, which are given by LAMMPS. Input file to VMD is named as *filename.lammpstrj*, which contains the coordinates of atoms at various time steps. The VMD input file of the MD simulation in Section 2.5.1 is given in Appendix B. Four different way of rendering the graphene sheet used in Section 2.5.1 is shown in Fig. 2.12.

2.7 Conclusions

This chapter reviewed the theory behind MD simulations. A set of MD simulations were done in order to investigate the effect of some MD parameters, such as potential field, strain rate, and time step on the stress-strain curve of a graphene sheet. Non-physical behaviour in stress-strain curve, induced by default cut-off function of REBO potential, could be removed by changing cut-off radii to 2 Å. Strain rate does not affect Youngs modulus, however

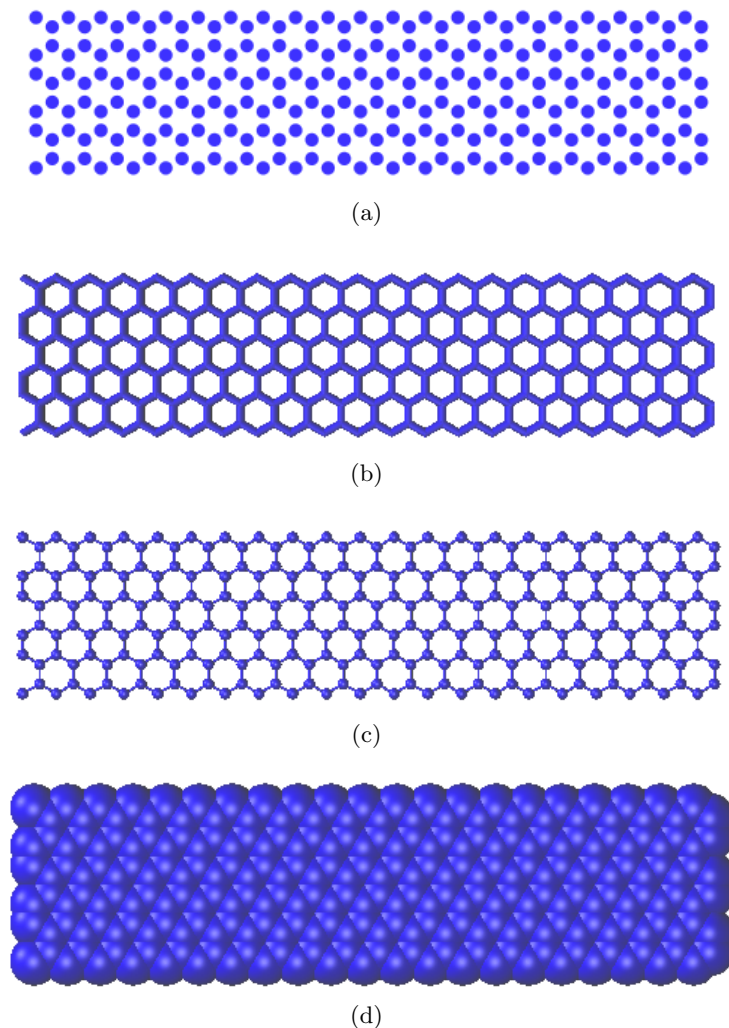


Figure 2.12: Various methods of rendering available in VMD.(a) Point, (b)Bond, (c)CPK and, (d)VDW

2.7. Conclusions

the higher strain rates result in higher ultimate stress and higher ultimate strains. Time step does not have an influence on the stress-strain curve. Intermolecular interaction and torsional interactions of AIREBO potential do not affect the stress-strain curve.

Chapter 3

Effect of Temperature and Edges on the Mechanical Properties of Graphene

Graphene can be subjected to higher temperature at production stage as well as when graphene based devices operate at higher temperature. Chemical vapour deposition (CVD), which is one of the most commonly used methods of graphene production, produces graphene at a temperature around 800 K. Therefore, understanding the temperature behaviour of graphene helps to fabricate high quality graphene based devices. On the other hand, understanding the effects of temperature on an infinitely large perfect graphene sheet sets the baseline for studying the geometric effects such as edges and defects. The ultimate tensile strength (σ_{ult}) and the ultimate strain (ε_{ult}) of an infinitely large armchair graphene sheet heavily depend on the temperature, however the Young's modulus is not affected by the temperature up to 1000 K [97]. The effect of temperature on zigzag graphene has not been previously investigated. The finiteness of graphene sheet also alters the mechanical properties of graphene [64, 65]. However, the effect of temperature on edges has not been studied.

An investigation of the effects of temperature on σ_{ult} , ε_{ult} , Young's modulus, and third order elastic modulus of infinitely large armchair and zigzag graphene sheets is presented in Section 3.1. This is followed by a study of the effects of edges on the mechanical properties of graphene at various temperatures presented in Section 3.2. Finally, the chapter is concluded in Section 3.3 with a comparison between the effects of edges of graphene

3.1. Effect of Temperature

and the effect of diameter of carbon nanotubes (CNTs) on the mechanical properties of the structures.

3.1 Effect of Temperature

In this section, a study of the effect of temperature on the mechanical properties of an infinitely large armchair and zigzag graphene sheet is presented. It should be noted that armchair and zigzag graphene sheets indicate graphene along armchair and zigzag direction. The study has been carried out by performing MD simulations at various temperatures ranging from 1 K to 800 K. Figure 3.1 shows the geometry of the graphene sheet used for the study. The size of the sheet is $50.26 \text{ \AA} \times 50.78 \text{ \AA}$ with 1008 carbon atoms. The C-C bond length of graphene is 1.396 \AA , which is the equilibrium C-C bond length of graphene according to AIREBO potential field. Periodic boundary conditions (PBCs) are used in both in-plane directions (x and y) to eliminate the effect of the edges. Initially, the graphene sheet is allowed to relax over a time period of 30 ps. The pressure components in x and y directions are equal to zero during this time period. The size of time step is 0.5 fs. Potential energy of the sheet is extracted at the end of each time step. Variation in the potential energy with the relaxation time is shown in Fig. 3.2 for a graphene sheet at 300 K. The sudden increase of potential energy at a time around 3 ps in Fig. 3.2 suggests that there could be a thermal expansion of the graphene sheet. However, AIREBO potential field is temperature independent and empirical parameters have been evaluated at 300 K [89]. Therefore, the expansion of the graphene sheet may come from the kinetic energy of the atoms.

3.1.1 Thermal Expansion

Strain energy stored in a graphene sheet at a particular strain is obtained by

$$U_\varepsilon = E_\varepsilon - E_0, \quad (3.1)$$

3.1. Effect of Temperature

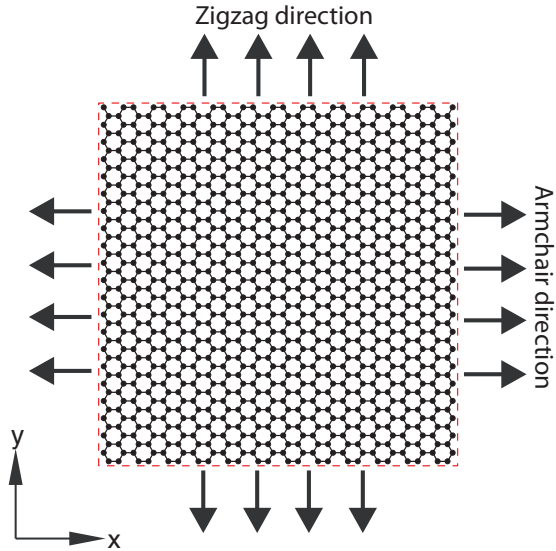


Figure 3.1: Graphene sheet used to study temperature effects. Outer dashed line indicates the boundaries of the box. Arrows indicate the armchair and zigzag directions of graphene.

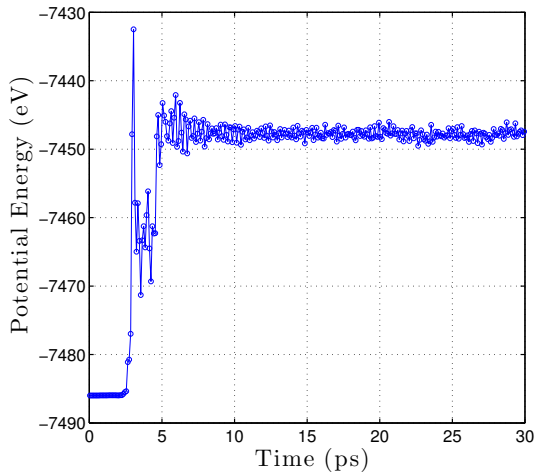


Figure 3.2: The variation of the potential energy of a graphene sheet with relaxation time at 300 K.

3.1. Effect of Temperature

where U_ε and E_ε are the strain energy and the potential energy at strain ε , respectively; E_0 is the potential energy of the unstrained graphene sheet.

Table 3.1 gives E_0 , kinetic energy (KE) and the equilibrium size of graphene sheet at various temperatures. These quantities were taken as the average values over the last 10 ps of the relaxation period. The area of the graphene sheet increases by 1.29 % when the temperature increases from 1 K to 800 K. This increase of area results in increasing E_0 of the graphene sheet by 1.38 %. Both KE and E_0 of the sheets increase linearly with the increasing temperature.

Table 3.1: Average physical quantities of graphene at equilibrium.

Temperature (K)	E_0 (eV)	KE (eV)	$L_x(\text{\AA})$	$L_y(\text{\AA})$
1	-7485.9	0.1	50.29	50.81
100	-7473.2	13.0	50.32	50.85
200	-7460.6	26.0	50.36	50.89
300	-7447.8	39.0	50.40	50.93
400	-7434.9	52.0	50.44	50.97
500	-7422.0	65.2	50.48	51.01
600	-7408.9	78.0	50.52	51.05
700	-7396.1	90.9	50.56	51.09
800	-7382.3	104.6	50.60	51.14

The relationship between the temperature (T) and the area of the graphene sheet at temperature T (A_T) can be written as

$$A_T = A_0(1 + \alpha T), \quad (3.2)$$

where A_0 is the area of the graphene sheet at 0 K and α is the coefficient of thermal expansion (CTE) of the graphene sheet which is defined as

$$\alpha = \frac{1}{A_0} \frac{dA}{dT}. \quad (3.3)$$

The values of A_0 and α are calculated by fitting a linear regression line between the temperature and the corresponding area of the graphene sheet. The values of A_0 and α are 2554.5 \AA^2 and $1.6 \times 10^{-5} \text{ K}^{-1}$, respectively.

3.1. Effect of Temperature

Experimental studies have found that the CTE of graphene is found to be $-6 \times 10^{-6} \text{ K}^{-1}$ [103] and $-7 \times 10^{-6} \text{ K}^{-1}$ [104] at temperature of 300 K, and the value of CTE increases from $-7 \times 10^{-6} \text{ K}^{-1}$ to $4 \times 10^{-6} \text{ K}^{-1}$ as temperature increases from 300 K to 400 K [104]. These anomalies in CTE could be due to two factors. Firstly, it has been found that substrate interaction strongly influences the CTE of graphene. Graphene has been suspended in the experiments in [103, 104], whereas the simulations presented in this work have been performed on free standing graphene. Jiang *et al.* [105], using nonequilibrium Green's function method, found that the CTE value of free standing graphene (without substrate) is $-6 \times 10^{-6} \text{ K}^{-1}$ at 300 K, and can go up to $2 \times 10^{-5} \text{ K}^{-1}$ with sufficiently strong substrate interaction. Secondly, surface ripples in graphene sheets have been experimentally observed at room temperatures [104, 106, 107]. These surface ripples, which are out-of-plane motion of atoms, could cause a contraction in the planar dimensions of graphene. This reduction of planar dimensions due to ripples could also be interpreted as a thermal contraction. In order to investigate this hypothesis, a set of MD simulations were performed with surface ripples on graphene. The ripples were introduced by giving a small random out-of-plane perturbation ($\approx 0.05 \text{ \AA}$) to atoms. This exercise resulted in a CTE of $3.6 \times 10^{-6} \text{ K}^{-1}$. The ripples reduce the CTE value of graphene by more than 75 %, which suggests that the sufficiently large ripples of graphene could even cause a negative CTE value as observed in the experiments. A recent study by Monica *et al.* [108], using first principle MD simulations, revealed that the C-C bond length of free standing graphene increases with temperature, and the rate of change is $6.5 \times 10^{-6} \text{ K}^{-1}$ for a free standing graphene sheet. This confirms that the area of graphene sheet could increase with the temperature in the absence of ripples.

Fig. 3.3 shows that the ripples of graphene increase with the temperature. MD simulations with different random out of plane perturbation (0.05 \AA to 0.25 \AA) have shown that the equilibrium area of a graphene sheet is independent of the initial random out-of-plane perturbation and depends only on the simulation temperature.

3.1. Effect of Temperature

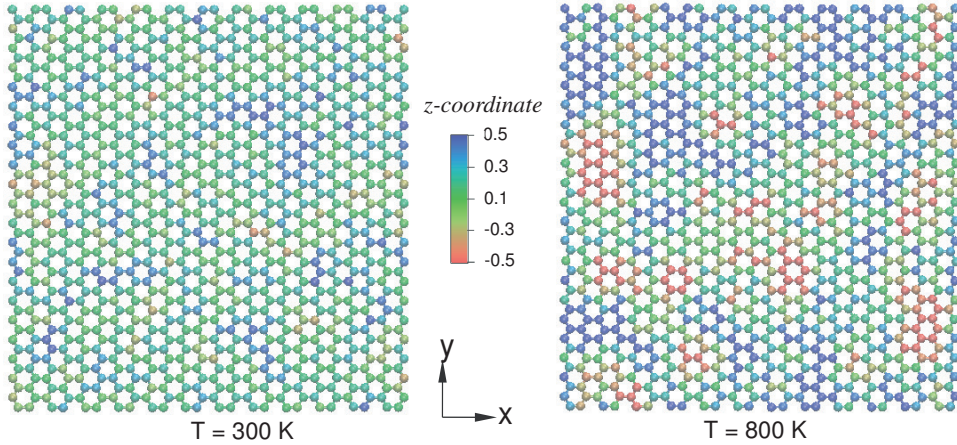


Figure 3.3: Ripples of graphene sheet at 300 K and 800 K. Scale bar indicates the out-of-plane deformation in Å

3.1.2 Stress Strain Behaviour

Fig. 3.4 shows the variation of normalized strain energy per unit volume of graphene sheet (U) with the strain (ε) at different temperatures. Strain energy has been normalized with respect to the maximum strain energy per unit volume at 1 K, which are $1.10 \times 10^{10} \text{ J m}^{-3}$ and $2.13 \times 10^{10} \text{ J m}^{-3}$ for armchair and zigzag sheets, respectively. It can be observed in Fig. 3.4 that graphene sheets at higher temperatures store a significantly higher amount of strain energy at a given strain.

Table 3.2 compares the strain energy stored in graphene sheets under a strain of 0.078 at different temperatures. Armchair graphene sheet stores 18% higher strain energy at 800 K compared to that at 1K and the corresponding value for zigzag graphene sheet is 20%. This can be due to the fact that the initial potential energy of graphene sheets is comparatively high at higher temperatures as shown in Fig. 3.5, due to the thermal expansion of graphene. It can be seen in Fig. 3.4 that U - ε curves at higher temperatures attain the linear portion of the curve relatively lower strains. On the other hand, a particular strain at a higher temperature resembles that of a slightly higher strain at a lower temperature and this leads the graphene sheets at higher temperatures to store more strain energy at a given strain. This

3.1. Effect of Temperature

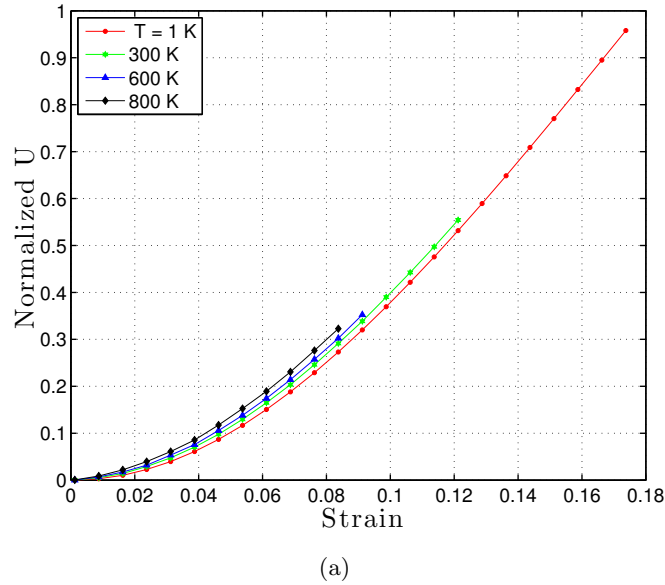
can be further explained by considering the potential energy vs bond length curve of a C-C bond as shown in Fig. 3.6. The equilibrium bond length at 0 K is 1.396 Å. According to AIREBO potential field, potential energy of a C-C bond is -4.95 eV. However, at higher temperatures, C-C bond length is greater than that at 0 K due to the thermal fluctuations arising from kinetic energy. This leads C-C bonds to store higher potential energy. The equilibrium bond length at 800 K is 1.408 Å and potential energy is -4.88 eV. Therefore, the equilibrium bond length at 800 K is under a strain of 0.009 compared to the equilibrium bond length at 0 K. Due to this discrepancy in the initial configurations, graphene sheet stores higher amount of strain energy at higher temperatures compared to that at lower temperatures at a given strain.

Table 3.2: Strain energy and stress of graphene sheets at various temperatures and under a strain of 0.078.

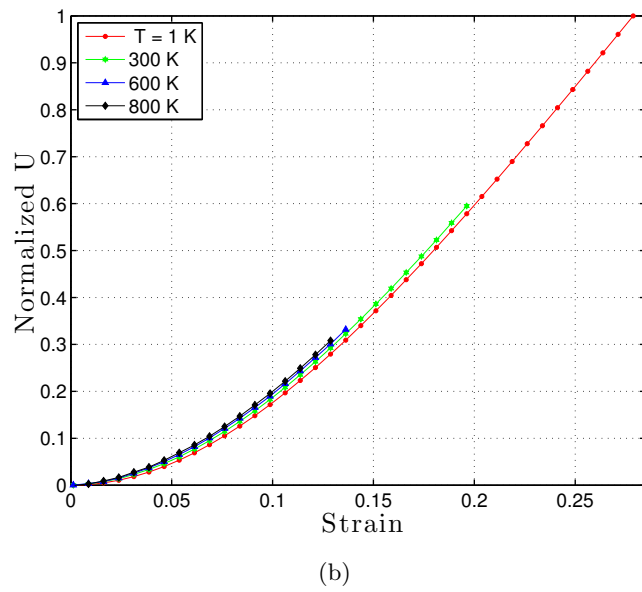
Temperature (K)	Strain energy (eV)		Stress (GPa)	
	armchair	zigzag	armchair	zigzag
1	148.4	130.0	66.5	58.8
100	152.7	133.2	67.2	59.6
200	151.6	134.3	66.9	59.7
300	159.8	140.8	68.3	61.0
400	161.4	144.1	68.8	61.5
500	166.8	145.7	69.8	61.7
600	166.3	148.9	69.9	62.4
700	171.7	153.3	71.1	63.2
800	178.7	153.8	72.4	63.4

It is also noticed in Table 3.2 that armchair graphene sheet stores a higher amount of strain energy compared to zigzag. This can be explained by considering the arrangement of C-C bonds in the straining directions of the graphene sheets as shown in Fig. 3.1. In armchair graphene sheet, there is a row of C-C bonds aligned in the straining direction and these bonds carry a higher strain compared to inclined ones. The inclined bonds contribute to carry a significant amount of strain by changing the bond angles apart from the bond length change. Strain energy from the bond

3.1. Effect of Temperature



(a)



(b)

Figure 3.4: Variation of the normalized strain energy (U) with strain up to the fracture of graphene sheet at different temperatures. The simulation temperatures are given in legends (a) Armchair (b) Zigzag

3.1. Effect of Temperature

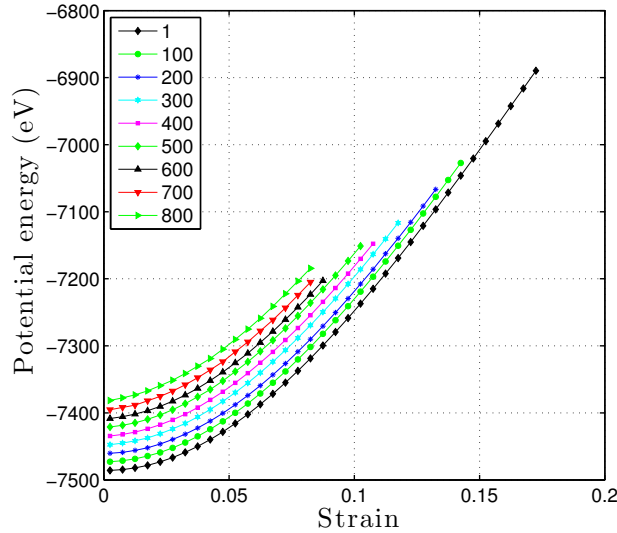
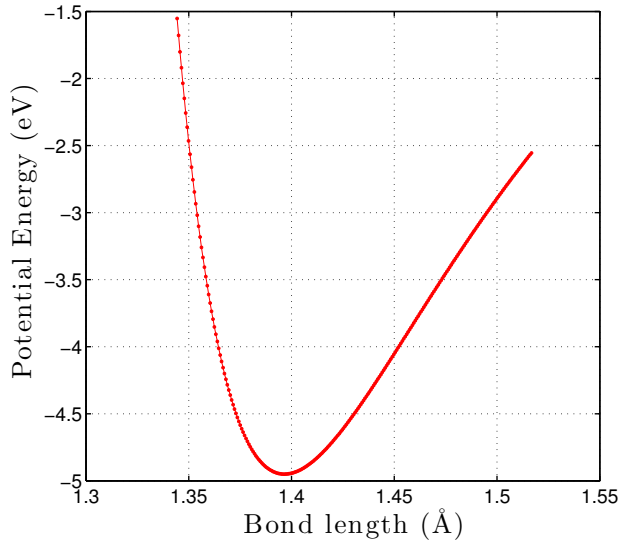


Figure 3.5: Variation of the potential energy of an armchair graphene sheet with strain. Legend gives the simulation temperatures.

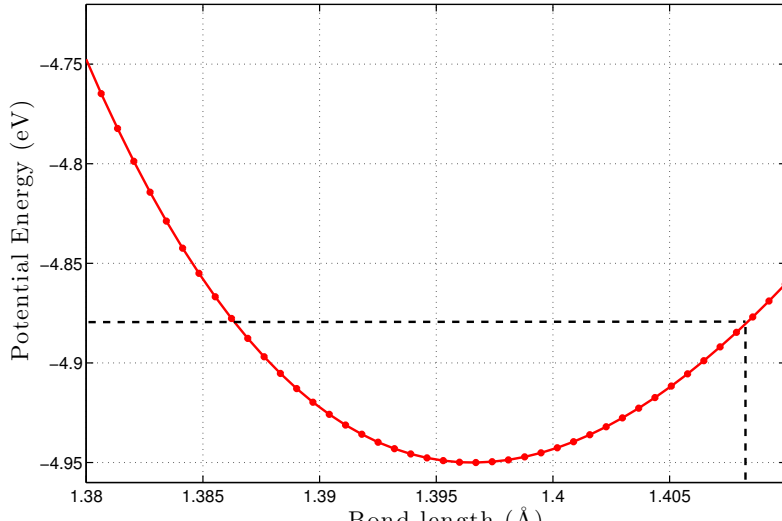
extension is much higher than that of bond angle variation [89]. All the C-C bonds in zigzag graphene are inclined and those carry a significant amount of strain by changing the bond angles. The extension of a comparatively large number of bonds in armchair sheet compared to zigzag sheet leads armchair sheet to store more strain energy compared to zigzag graphene at a given strain.

Table 3.3 compares the strain energy stored in graphene sheets up to fracture at different temperatures. Armchair graphene sheet stores only about 50% of the strain energy stored by zigzag graphene sheet at all temperatures. The fracture of armchair sheet occurs at lower strain compared to zigzag sheet due to higher extension of C-C bonds in armchair graphene as explained above. It is also important to notice that the initial configurations of graphene sheet are different at different temperatures as given in Table 3.1. However, the different initial configuration alone does not explain the fracture of graphene sheets at lower strain in higher temperatures. As an example, the difference in equilibrium energies at 1 K and 800 K is 104

3.1. Effect of Temperature



(a)



(b)

Figure 3.6: (a) Change in potential energy of a bond with bond length at 0 K. (b) Shows the change around equilibrium bond length. The dashed horizontal line marks the unstrained potential energy of a bond at 800 K.

3.1. Effect of Temperature

Table 3.3: Strain energy stored in a graphene sheet up to fracture at various temperatures.

Temperature (K)	Strain energy (eV)	
	armchair	zigzag
1	596	1156
100	446	854
200	394	735
300	331	689
400	287	499
500	271	528
600	206	378
700	191	292
800	198	362

eV due to thermal expansion. However, the difference in strain energies at fracture of zigzag graphene sheet at 1 K and 800 K is 794 eV. The percentage reduction of the strain energy at 800 K compared to 1 K is 67% and 69% for armchair and zigzag graphene sheets, respectively.

It has been found that the fracture strength of covalent materials, such as graphene, primarily depends on the inflection point of the interatomic energy and is almost independent of the energy required to break bonds (bond dissociation energy) [88]. Table 3.3 indicates that the fracture of graphene is independent of the bond dissociation energy which confirms the findings in [88]. At higher temperatures, local strain can exceed the bond breaking strain which corresponds to the inflexion point of the potential due to thermal movements of atoms. Fracture of a single bond leads to progressive fracture of the graphene sheet.

In order to obtain the stress-strain (σ - ε) relation of graphene, a third order polynomial is fitted on the strain (ε) and the strain energy per unit volume (U) data, in the form of

$$U = \frac{D}{3}\varepsilon^3 + \frac{E}{2}\varepsilon^2 + C\varepsilon + K, \quad (3.4)$$

where D is the third order elastic modulus, E is the Young's modulus; C

3.1. Effect of Temperature

takes into account any residual stress in the graphene sheet and K gives full flexibility to the model. It should be noted that E in this study is slightly different from the conventional Young's modulus which is defined as slope of the linear part of σ - ε curve. However, the σ - ε curve of graphene is nonlinear. Therefore, E has been defined as the initial slope of the σ - ε curve.

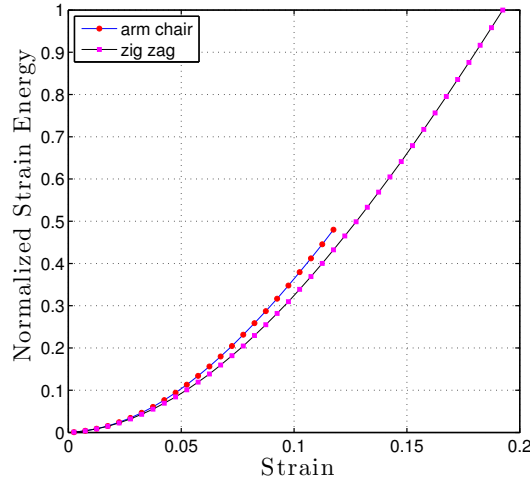
Stress (σ) is obtained by taking the first derivative of the strain energy in Eq. (3.4) with respect to ε as

$$\sigma = \frac{\partial U}{\partial \varepsilon} = D\varepsilon^2 + E\varepsilon + C. \quad (3.5)$$

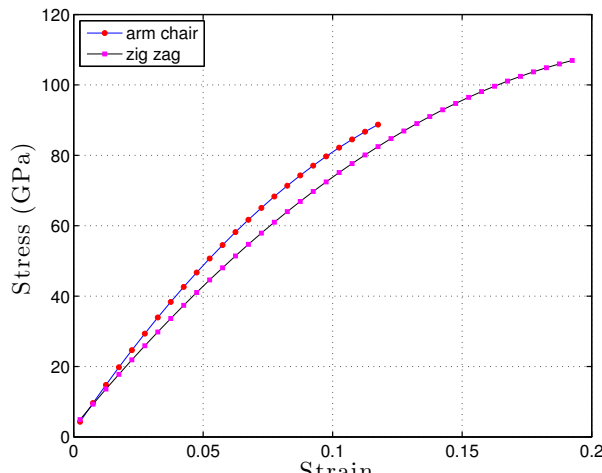
The comparison of σ - ε relations of armchair and zigzag graphene sheet in Fig. 3.7 shows that zigzag sheet is much stronger than armchair sheet. This can be explained by considering the orientation of C-C bonds in zigzag and armchair sheets as mentioned above. Zigzag sheet can go up to 64% higher strain compared to armchair sheet, but it results in only 21% higher ultimate stress due to the reduction of stiffness of zigzag sheet with increasing strain as shown in Fig. 3.7.

The σ - ε relations of armchair and zigzag graphene sheets at various temperatures are shown in Fig. 3.8. It can be observed that sheet at higher temperatures is under a tensile stress even in an unstrained condition. Table 3.4 compares the initial stress of sheets at different temperatures. The origin of this stress is the thermal expansion, as explained in Section 3.2.3, causes C-C bonds in graphene to expand. Fig. 3.6(b) indicates that the gradient of U - ε curve, which is stress, is a positive value for the bond lengths greater than 1.396 Å. This introduces a tensile stress at the equilibrium configuration. However, Table 3.4 indicates that the initial stress of armchair and zigzag sheets are not equal. This suggest that there is another factor affecting this initial stress since the initial configurations for both armchair and zigzag sheets are similar. One possible cause is the continuum stress interpretation used in this work, which is given in Eq. (3.6). It should be noted that the initial stress of graphene is dependent on the complete U - ε relation due to the curve fitting. In order to remove this dependence of initial stress on the higher stress values, stress at a particular strain was

3.1. Effect of Temperature



(a)



(b)

Figure 3.7: Comparison of armchair and zigzag graphene sheets at a temperature of 300 K. (a) normalized strain energy, with respect to $1.273 \times 10^{10} \text{ J m}^{-3}$, which is the maximum strain energy stored in zigzag graphene sheet. (b) Stress-strain curves.

3.1. Effect of Temperature

Table 3.4: Initial stress of graphene sheets given by Eq. (3.6) at various temperatures and under unstrained condition.

Temperature (K)	Stress (GPa)	
	armchair	zigzag
1	-2.9	0
100	-1.6	0
200	-1.6	0.4
300	0.6	2.2
400	1.4	3.5
500	2.8	4.0
600	2.9	4.6
700	4.1	5.7
800	5.1	6.3

calculated using finite difference method, which is given by

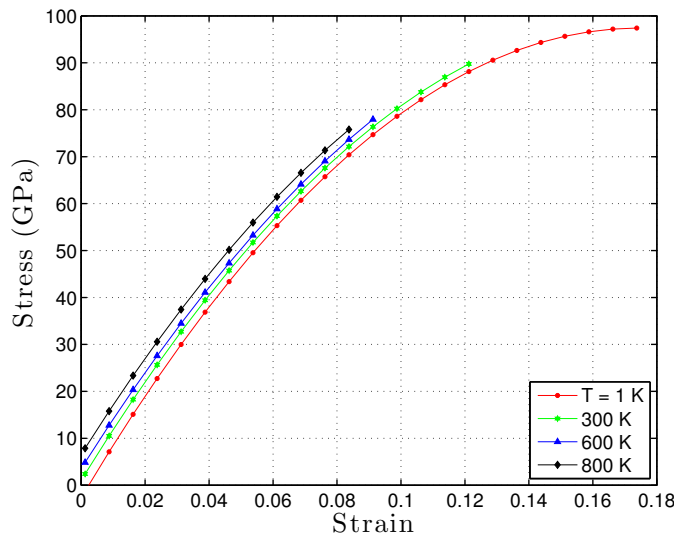
$$\sigma_{\varepsilon+\Delta\varepsilon/2} = \frac{U_{\varepsilon+\Delta\varepsilon} - U_\varepsilon}{\Delta\varepsilon}, \quad (3.6)$$

where $\Delta\varepsilon$ is the strain increment which has the value of 0.005.

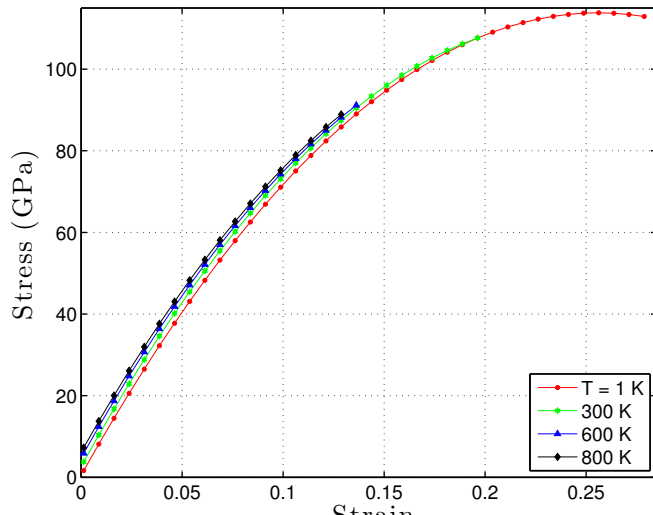
Initial stress was obtained by fitting a linear regression line between stress, calculated using Eq. (3.6), and strain up to a strain value of 0.04. This analysis indicated that initial stress of armchair and zigzag graphene sheets increases as temperature increases from 1 K to 800 K. It is from 0 to 7.6 GPa and 0.3 to 7 GPa for armchair and zigzag graphene sheets, respectively. This investigation confirms that the initial stress has been introduced by the thermal expansion of graphene due to kinetic energy. However, the kinetic energy of the system is neglected in the continuum definition of stress. Therefore, an atomistic stress measure, which takes kinetic energy into account, could be a better stress measure for graphene sheets at a finite temperature.

Several definitions have been developed to calculate the local atomic stress [109–114]. Virial stress, which is the most commonly used atomistic stress measure, takes into account the stress contribution from kinetic energy. On the other hand, virial stress depends only on the current state of

3.1. Effect of Temperature



(a)



(b)

Figure 3.8: Stress-strain curves of arm-chair (a) and zigzag (b) graphene sheets at different temperatures.

3.1. Effect of Temperature

strain as opposed to the continuum approach. The virial stress has been developed based on the virial theorem for gas pressure [114–116], which can be expressed as,

$$\sigma_{ij}^V = \frac{1}{V} \sum_{\alpha} \left[\frac{1}{2} \sum_{\beta=1}^N \left(R_i^{\beta} - R_i^{\alpha} \right) F_j^{\alpha\beta} - m^{\alpha} v_i^{\alpha} v_j^{\alpha} \right], \quad (3.7)$$

where (i, j) are the directional indices (x, y, and z), β is an assigned number to neighbouring atoms which goes from 1 to N , R_i^{α} is the position of atom α along direction i , $F_j^{\alpha\beta}$ is the force along direction j on atom α due to atom β . m^{α} is the mass of atom α , v^{α} is thermal excitation velocity and V is the total volume. It can be observed in Eq. (3.7) that at low temperatures, the stress contribution from kinetic part ($m^{\alpha} v_i^{\alpha} v_j^{\alpha}$) becomes negligible due to low velocities of atoms.

There was a controversy regarding the kinetic part in virial stress, which is given by the term $m^{\alpha} v_i^{\alpha} v_j^{\alpha}$ in Eq. (3.7). Zhou argued that the virial stress definition with kinetic part is not equivalent to Cauchy stress [117]. However, it has been recently demonstrated that the virial stress with kinetic part is equivalent to Cauchy stress [118].

Table 3.5 presents the virial stress of a graphene sheet under various temperatures in unstrained state. It shows that there is a residual stress when kinetic part is being ignored. However, this residual stress has been cancelled out by the kinetic energy part in the complete virial stress definition. This observation suggests that the complete virial stress, including kinetic energy, gives better explanation about the stress state of the graphene sheet compared to the continuum interpretation of stress used in this work. However, the continuum interpretation used in this work is much similar to the virial stress measure excluding the kinetic part. Fig. 3.9 shows that virial stress is equivalent to continuum stress at lower strains (up to ≈ 0.05), but gives higher stress values as strain increases. It also shows that the contribution from the kinetic part is a constant value, 0.7 GPa, at all strains.

Figure 3.10 compares the variation of σ_{ult} and ε_{ult} with temperature. It can be seen that the effect of temperature is similar in both zigzag and

3.1. Effect of Temperature

Table 3.5: Virial stress of a graphene sheet given by Eq. (3.7) at various temperatures and under unstrained condition.

Temperature (K)	Virial Stress (GPa)	
	With KE	Without KE
1	0.00	0.00
100	0.00	0.23
200	0.00	0.48
300	0.00	0.71
400	0.00	0.96
500	0.00	1.20
600	0.00	1.42
700	0.00	1.66
800	0.01	1.92

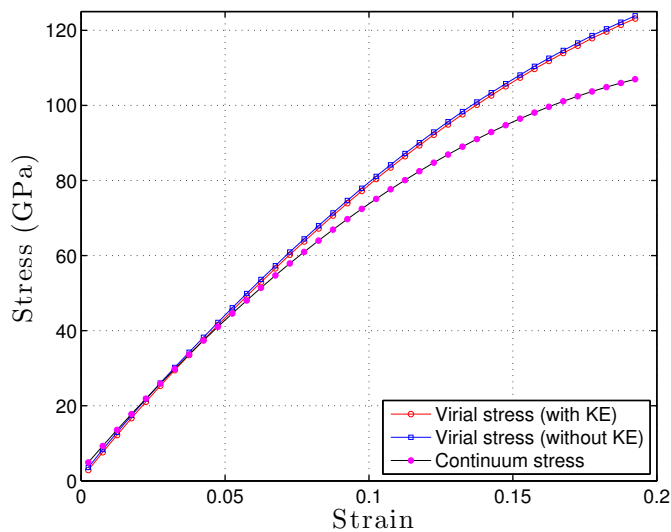


Figure 3.9: Comparison of virial stress and continuum stress of a zigzag graphene sheet at 300 K.

3.1. Effect of Temperature

armchair graphene sheets. Reduction of σ_{ult} is 23% and 27% and reduction in ε_{ult} is 54% and 59% in armchair and zigzag sheets, respectively. It can be noticed in Fig. 3.11 that the effect of temperature on the Young's modulus is not that significant. There is only a slight reduction in Young's modulus with increasing temperature in both graphene sheets. However, there is a significant reduction in the third order modulus (about 10%) of armchair graphene sheet. The reduction of third order modulus in zigzag direction is not significant. Another important fact about third order modulus is that the modulus in zigzag direction is much smaller than the value in armchair direction. At 300 K, the third order modulus in zigzag direction is 41% lesser than that in armchair direction, which agrees quite well with the values obtained from tight binding calculations in [119].

Fracture of armchair graphene sheet occurs always perpendicular to the straining direction, while diagonal fracture has been observed in zigzag graphene sheet as shown in Fig. 3.12. Fracture occurs at the bonds, which carry more load in both graphene sheets. Insets of Fig. 3.12 show the forces carried by three C-C bonds of a typical atom. Considering the equilibrium along T_1 direction, the relationship between the three forces can be written as,

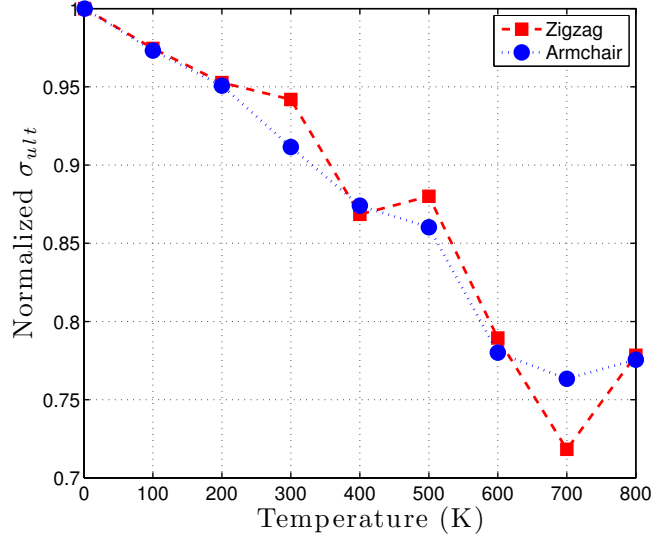
$$T_1 = (T_2 + T_3) \cos\left(\frac{\theta}{2}\right). \quad (3.8)$$

However, $T_2 = T_3$ due to symmetry. This reduces Eq. (3.8) to

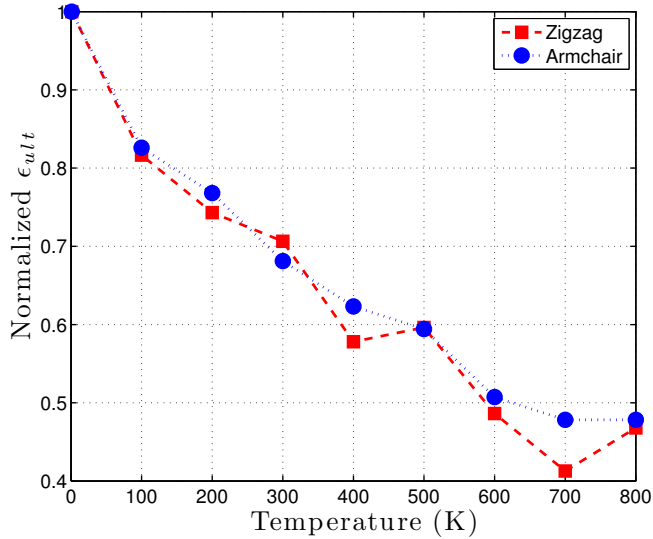
$$T_1 = 2T_2 \cos\left(\frac{\theta}{2}\right). \quad (3.9)$$

When the sheet is unstrained, $\theta = 120^0$, so $T_1 = T_2$. However, when the sheets are subjected to a strain, θ becomes less than 120^0 for armchair graphene sheet, which makes $T_1 > T_2$, so the fracture occurs at bonds aligned with the straining direction, and propagates perpendicular to the straining direction. In the case of zigzag graphene sheet, θ becomes larger than 120^0 so $T_1 < T_2$. Therefore, the fracture occurs at the bonds which are inclined $\pm 30^0$ to the straining direction and propagates at an angle of $\pm 60^0$

3.1. Effect of Temperature



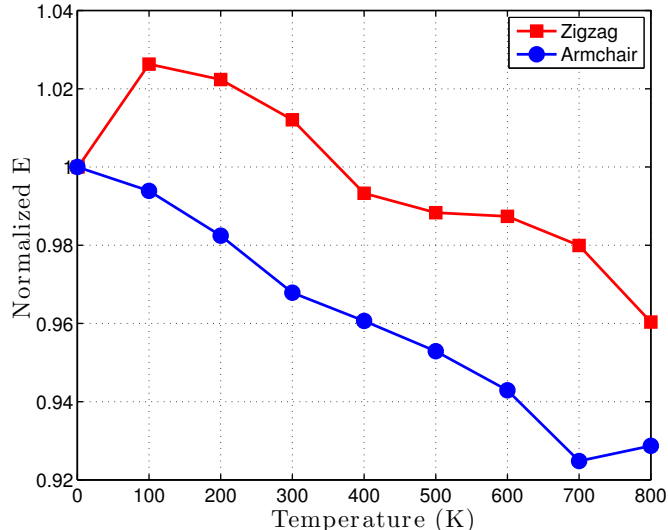
(a)



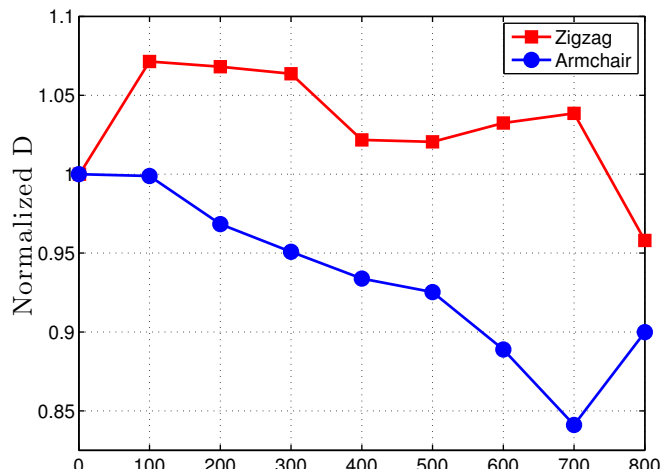
(b)

Figure 3.10: Effect of temperature on ultimate stress and strain of graphene sheets. (a) The ultimate stress values have been normalized by the values at 1 K that are 97.3 GPa and 113.6 GPa for armchair and zigzag sheets, respectively. (b) The ultimate strain values have been normalized by the values at 1 K that are 0.173 and 0.273 for armchair and zigzag sheets, respectively.

3.1. Effect of Temperature



(a)



(b)

Figure 3.11: (a) Comparison of the change in Young's modulus of graphene sheets with temperature. The Young's modulii have been normalized by the values at 1 K, which are 1.15 TPa and 0.89 TPa for armchair and zigzag sheets, respectively. (b) Comparison of the change in the third order modulus with the temperature. The third order modulus have been normalized by the values at 1 K, which are -3.30 TPa and -1.74 TPa for armchair and zigzag sheets, respectively.

3.2. Effect of Edges

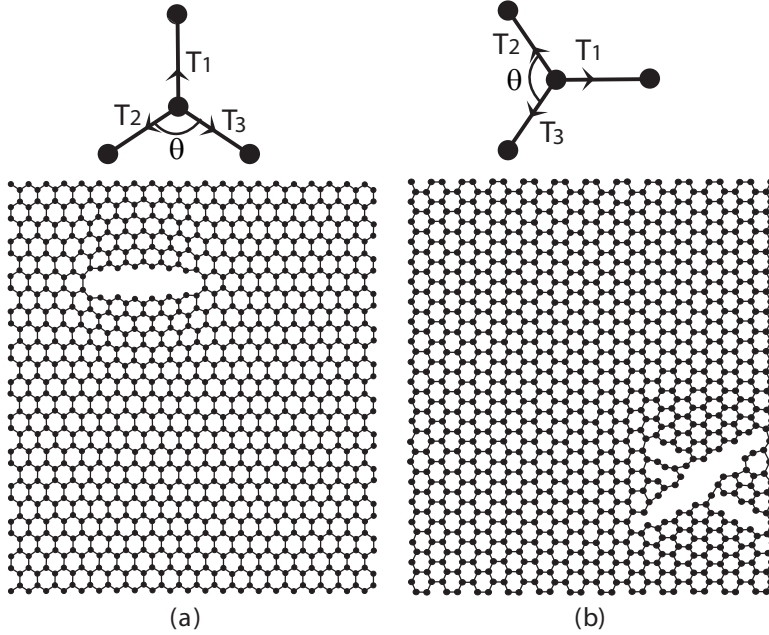


Figure 3.12: Nucleation of fracture of graphene sheet at 300 K (a) Armchair (b) Zigzag.

to the straining direction.

3.2 Effect of Edges

Researchers have used very narrow graphene sheets, called nanoribbons (width ≈ 15 nm) for experiments on graphene based transistors [60]. Theoretical studies have indicated that both electronic and mechanical properties of graphene depend on the edge configuration [55–57]. Even though several researchers have investigated the effect of edges on the mechanical properties of graphene [62–65], none of these studies have investigated the change of the effect of edges with temperature. On the other hand, many of the previous studies have been conducted using *ab initio* calculations or molecular mechanics [62, 65, 120–122], which are computationally expensive.

This section presents a study of the effect of edges on the mechanical properties of finite graphene sheets using MD. The widths of the graphene

3.2. Effect of Edges

sheets are varied in the range from 0.7 nm to 26.7 nm for armchair and form 1.1nm to 26.7 nm for zigzag. The smallest sizes of armchair and zigzag graphene sheets are shown in Fig. 3.13. PBCs have been applied in the longitudinal direction, while keeping transverse edges free. Lengths of graphene sheets are 50.26 Å and 50.78 Å for armchair and zigzag sheet, respectively.

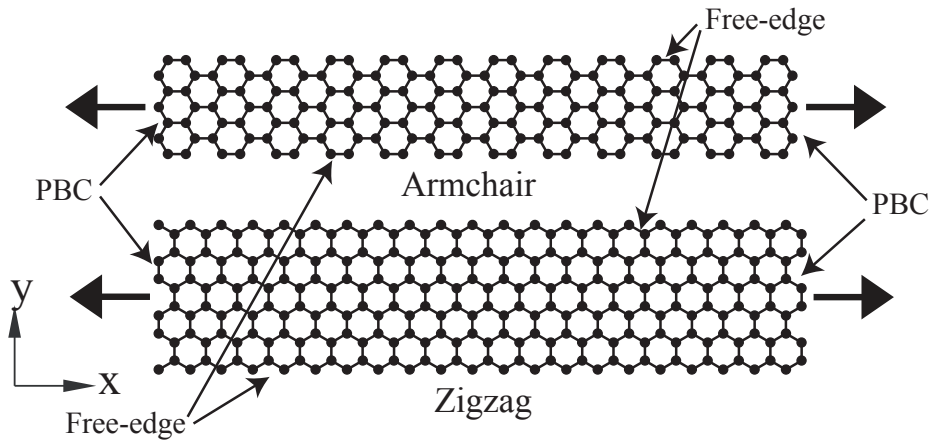


Figure 3.13: The smallest graphene sheet used for the study. Arrows indicate the direction where strain is applied.

3.2.1 Equilibrium Configuration

Initially, graphene sheets are allowed to relax over a time period of 30 ps. Elongation of sheets along the longitudinal direction has been observed as the sheets reaches equilibrium configuration. The elongation is significantly higher for narrow sheets. In order to quantify this, a quantity named initial strain ($\varepsilon_{initial}$) is introduced.

$$\varepsilon_{initial} = \frac{l_{eq} - l_0}{l_0}, \quad (3.10)$$

where l_{eq} is the equilibrium length of the graphene sheet and l_0 is the equilibrium length of the graphene sheet with an infinite width (PBCs in both longitudinal and transverse directions). The values of l_0 for armchair and zigzag graphene sheets are 50.29 Å and 50.81 Å, respectively.

3.2. Effect of Edges

Figure 3.14 compares $\varepsilon_{initial}$ of armchair and zigzag graphene sheets. The figure shows that the graphene sheets are subjected to a significant initial strain in both cases which could be as high as 0.015 at narrow widths. It also shows that zigzag graphene sheets are subjected to much higher initial strains compared to that of armchair sheets. This $\varepsilon_{initial}$ can also be calculated theoretically as explained below [64, 65].

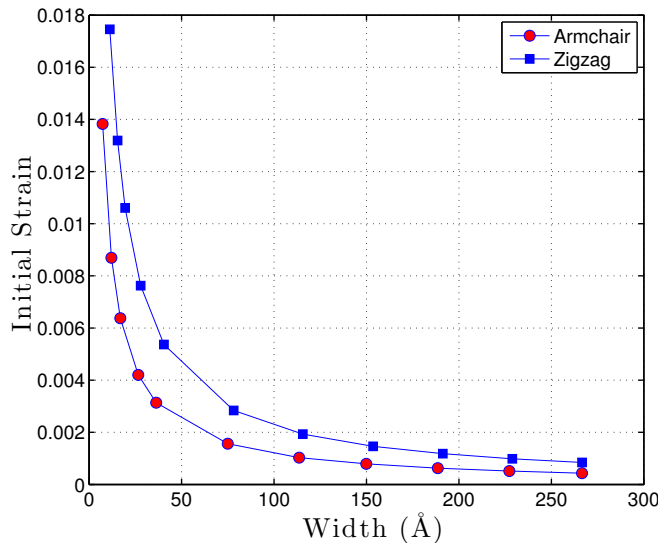


Figure 3.14: Variation of initial strain of graphene sheets with width.

The concept of surface stress of a three-dimensional (2D) crystal, proposed by Cammarata [123], can be used to define the edge stress of a graphene sheet(2D) [64]. The potential energy per unit length of a finite graphene sheet of width w subjected to an axial strain ε can be expressed as

$$U(\varepsilon, w) = U_0 + 2\tau\varepsilon + 2\frac{1}{2}E_s\varepsilon^2 + \frac{1}{2}E\varepsilon^2w, \quad (3.11)$$

where U_0 is the potential energy at zero strain. E and E_s are the bulk elastic modulus and edge elastic modulus, respectively. τ is the edge stress of graphene, which arises from the the difference of the energy between edge

3.2. Effect of Edges

and interior atoms. The second and third terms in (3.11) are related to the edge effects. The factor of two in these edge terms accounts for the two free edges of graphene. Stress $\sigma(\varepsilon, w)$ of the graphene sheet can be obtained from the derivative of Eq. (3.11) with respect to ε as

$$\sigma(\varepsilon, w) = \frac{2\tau}{w} + \frac{2E_s\varepsilon}{w} + E\varepsilon, \quad (3.12)$$

where, the effective Young's modulus (E_{eff}) can be defined as

$$E_{eff} = \frac{2E_s}{w} + E. \quad (3.13)$$

It can also be noticed in Eq. (3.12) that τ generates an $\varepsilon_{initial}$ at zero stress, which can be expressed as

$$\varepsilon_{initial} = \frac{-2\tau}{(2E_s + Ew)} = \frac{-2\tau}{wE_{eff}}. \quad (3.14)$$

Quing *et al.*, using molecular mechanics simulations with REBO potential field, found that the value of τ is -2.6 nN and -1.36 nN for zigzag and armchair graphene sheets [65].

When the two transverse edges of a graphene sheet are fixed in order to prevent initial strain, the graphene sheet buckles as shown in Fig. 3.16.

Fig. 3.17 shows the variation in potential energy with the distance from the edge. Excess edge energy (γ) of armchair and zigzag graphene sheet can be calculated as [65]

$$\gamma_{ac} = \frac{2(U_{a1} + U_{a2} - 2U_0)}{3r_0}, \quad (3.15a)$$

$$\gamma_{zz} = \frac{(U_{z1} + U_{z2} - 2U_0)}{\sqrt{3}r_0}, \quad (3.15b)$$

where U_{a1} , U_{a2} , U_{z1} and U_{z2} are the average potential energy of a edge atoms of armchair and zigzag graphene as demonstrated in Fig. 3.17; U_0 is the potential energy of an interior atom; r_0 is the equilibrium C-C bond

3.2. Effect of Edges

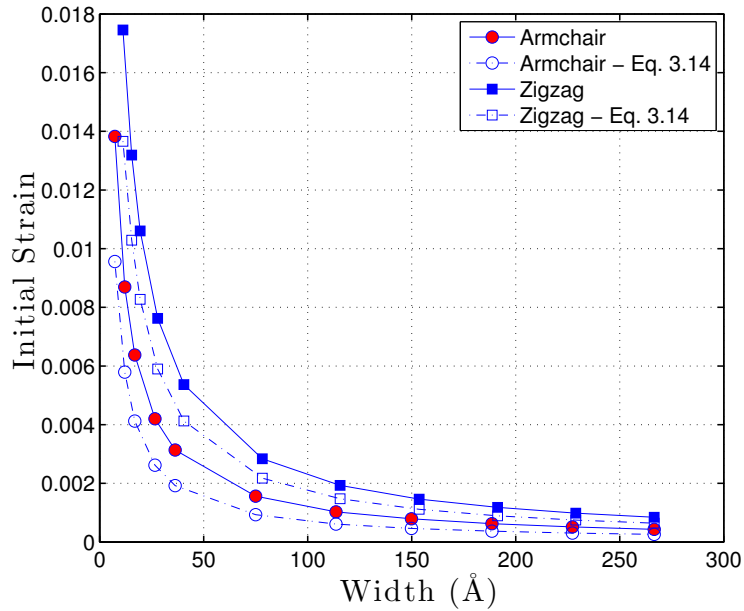


Figure 3.15: Comparison of initial strain of graphene sheets with width given by MD and Eq. (3.14)

length of graphene.

The calculated values of γ_{ac} and γ_{zz} are 11.63 eV/nm and 10.81 eV/nm. These values of γ_{ac} and γ_{zz} are well within the values reported in literature, which are given in Table 3.6. The values depend on the potential field and particular DFT method used for simulation. The values calculated in this work might give better approximation compared to values presented in [65] due to the fact that AIREBO potential field used in this work take into account the non-bonded interactions. According to DFT methods, γ_{zz} is greater than γ_{ac} , whereas REBO and AIREBO potential fields gives γ_{ac} is greater than γ_{zz} . However, the values calculated using empirical potential fields may be more accurate compared to the ones obtained from DFT, due to the fact that empirical potential fields use experimental data to fit some parameters of the potential field [90], whereas DFT is purely theoretical.

It can be noticed in Fig. 3.17 that the potential energy of the atoms in

3.2. Effect of Edges

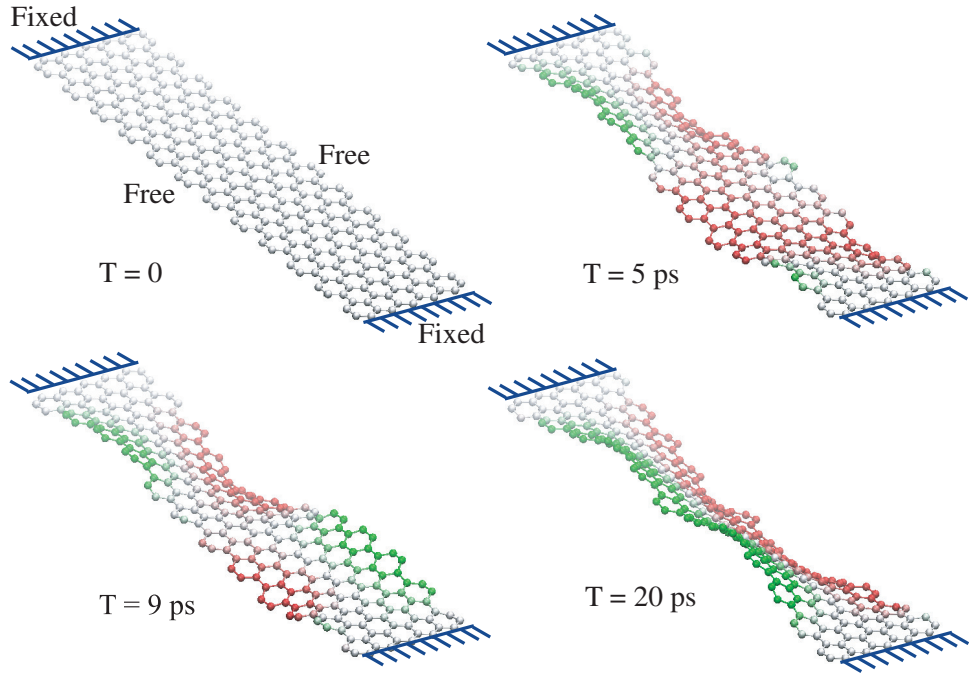


Figure 3.16: Buckling of an armchair graphene sheet due to edge force.

Table 3.6: Excess edge energy of graphene sheets by different methods.

Method	γ_{ac}	γ_{zz}
DFT (GAPW) [120]	9.8	13.2
DFT (VASP) [121]	10.0	12.0
DFT (SIESTA) [122]	12.43	15.33
MM (REBO) [65]	10.91	10.41
MD (AIREBO) [This work]	11.63	10.81

3rd row does not equal to the potential energy of interior atom due to non bonded interactions. Therefore, the conventional equation for γ given in

3.2. Effect of Edges

Eq. 3.15 should be modified as

$$\gamma_{ac} = \frac{2(U_{a1} + U_{a2} + U_{a3} + U_{a4} - 4U_0)}{3r_0}, \quad (3.16a)$$

$$\gamma_{zz} = \frac{(U_{z1} + U_{z2} + U_{z3} + U_{z4} + U_{z5} + U_{z6} - 6U_0)}{\sqrt{3}r_0}. \quad (3.16b)$$

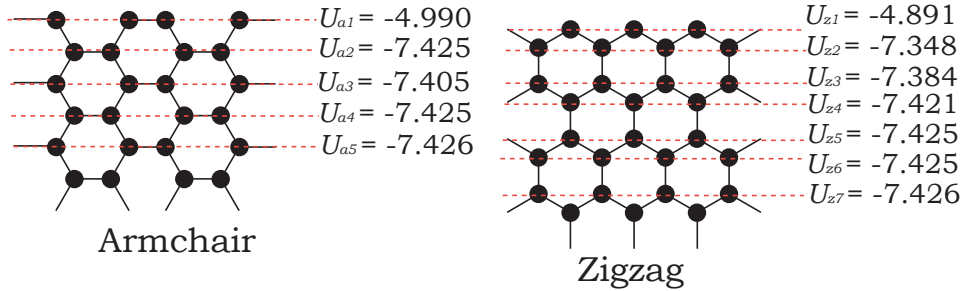


Figure 3.17: Potential energy variation of the atoms with the distance from the edge. $U_{a/z,i}$ is the average potential energy of an atom of armchair/zigzag graphene sheet in the i^{th} row indicated by a dashed line. Units of $U_{a,i}$ is eV.

The values of γ_{ac} and γ_{zz} according to Eq. 3.16 are 11.74 eV/nm and 11.01 eV/nm, respectively.

3.2.2 Stress Strain Behaviour

Fig. 3.18(a) shows that armchair graphene sheets with lower width break at relatively lower strains. However, at a given strain, armchair graphene sheets store equal amount of strain energy irrespective to the width. It can be seen in Fig. 3.18(b) that zigzag graphene sheets with narrow widths store a significantly higher amount of strain energy compared to the wider ones.

In order to further investigate the effect of edges on the strain energy storage of narrow graphene sheets, a $50 \text{ \AA} \times 50 \text{ \AA}$ symmetric graphene sheet was kept under various strains for 50 ps and then the average potential energy of atoms over last 40 ps of 50 ps was obtained. The free edges are kept

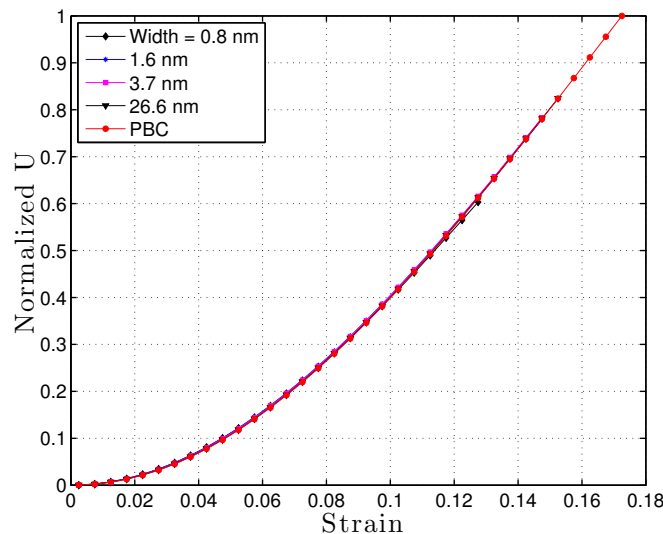
3.2. Effect of Edges

parallel to y-direction and PBCs were used along y-direction. Potential energy of atoms of an infinitely large graphene sheet was first obtained and that sets the baseline for the investigation. Fig. 3.19(a) and Fig. 3.20(a) show the potential energy variation with x-coordinates of an infinitely large armchair and zigzag graphene sheets, respectively. Potential energy at a x-coordinate given in the figures were taken as the average potential energy of all the atoms with similar x-coordinate, which is 24 atoms in armchair sheet and 21 atoms in zigzag sheet. As seen in Fig. 3.19(a) and Fig. 3.20(a), potential energy of atoms do not change near the edges due to the absence of edges. Fig. 3.19(b) and Fig. 3.20(b) show the variation of potential energy of finite armchair and zigzag graphene sheets, respectively. The figures show that the atoms close to edges store a significantly high potential energy at higher strains. This could be a result of higher change in bond angles near the edges compared to interior ones. It can also be noticed in Fig. 3.19(b) that potential energy of edge atoms decrease with increasing strain in armchair graphene sheets, which could compensate the increased potential energy of the atoms close to edge, so U - ε curve is not affected by edge atoms. However, zigzag edge atoms do not contribute to strain energy as seen in Fig. 3.20(b). Therefore, U - ε curve indicates the increase in potential energy of atoms which are close to edge.

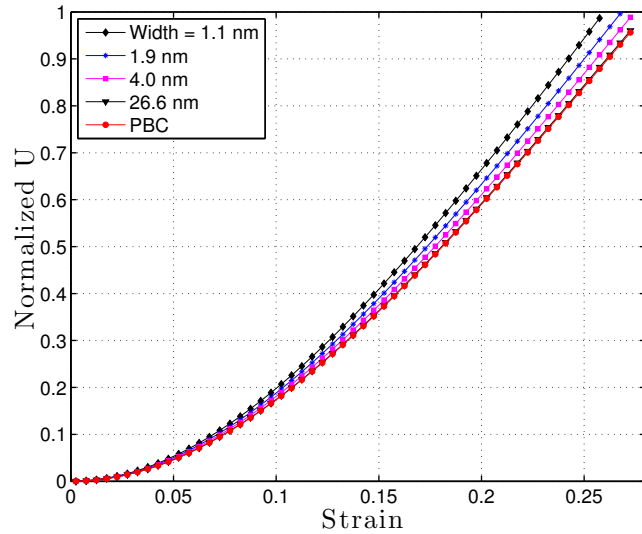
Stresses in the graphene sheets are calculated using Eq.(1.4). Fig. 3.21 shows the σ - ε relations of graphene sheets with various widths. It can be observed that narrow zigzag graphene sheets demonstrate a higher σ_{ult} values compared to the wider ones, even though they have smaller ε_{ult} values. This is due to the fact that atoms close to edges of zigzag graphene sheets store a higher amount of strain energy as explained above. Influence of edge atoms becomes greater as the graphene sheet gets thinner, which subjects narrow zigzag graphene sheets to a higher stress at a given strain.

Fig. 3.22 compares σ_{ult} and ε_{ult} of graphene sheets with various widths. There is a reduction of σ_{ult} in armchair sheets at narrow widths, while there is an increase in the σ_{ult} of zigzag sheets. The ε_{ult} of zigzag graphene sheets have not been affected much at narrow widths. However, the effect on armchair graphene is considerably high. This indicates that width of the

3.2. Effect of Edges



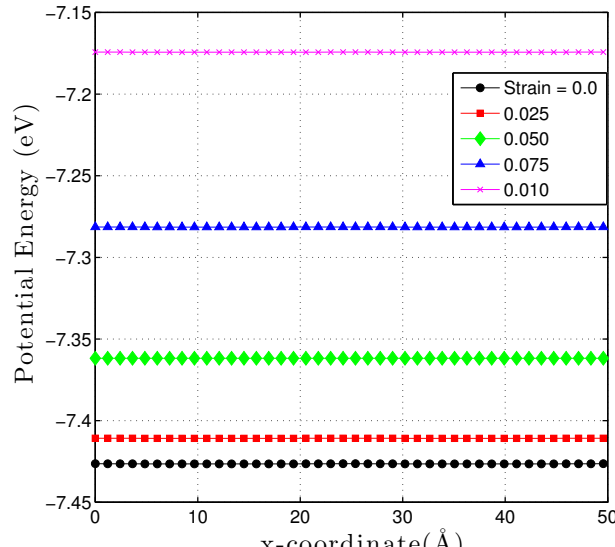
(a)



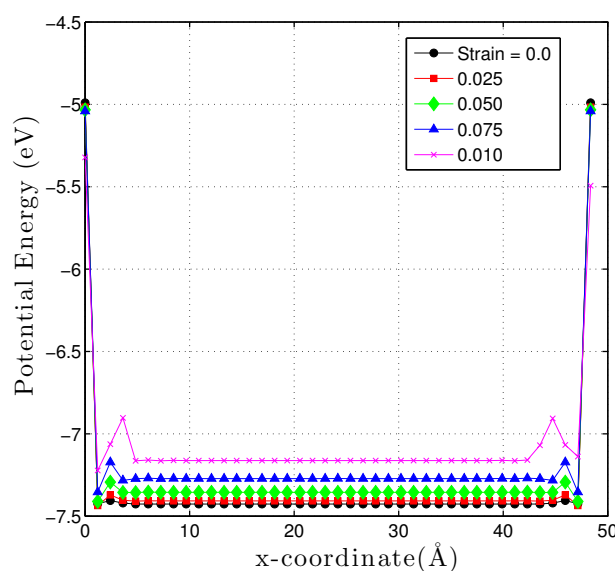
(b)

Figure 3.18: Variation of strain energy with strain of graphene sheet with different widths at 1 K (a) Armchair (b) Zigzag.

3.2. Effect of Edges



(a)



(b)

Figure 3.19: Variation of potential energy of atoms at different strains of (a) Infinitely large armchair graphene sheet (b) Armchair graphene sheet with edges . All the simulations are done at 1K.

3.2. Effect of Edges

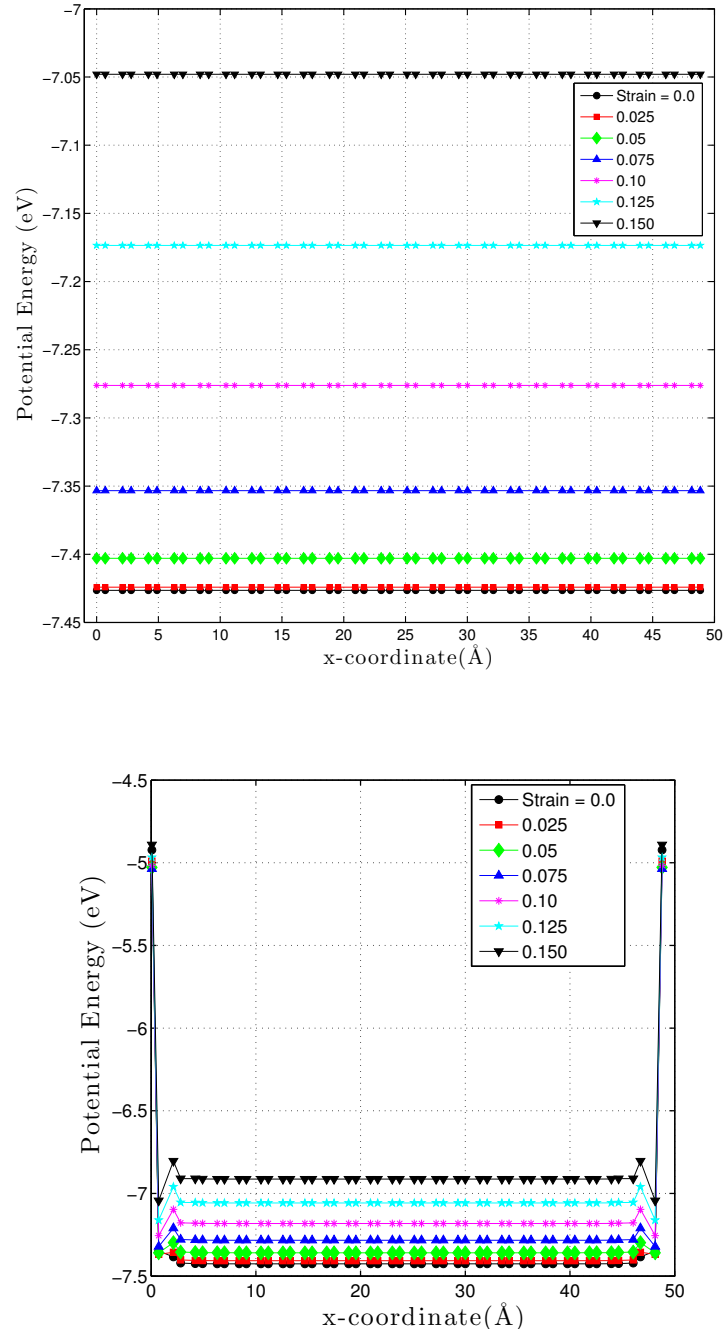


Figure 3.20: Variation of potential energy of atoms at different strains of (a) Infinitely large zigzag graphene sheet (b) Zigzag graphene sheet with edges. All the simulations are done at 1K.

3.2. Effect of Edges

graphene sheet has a greater influence on the strength properties of armchair graphene sheet compared to zigzag graphene sheets.

Fig. 3.23 compares the variation of E and D with width. Zigzag graphene sheets show a gradual reduction of E with the width. Armchair graphene sheets do not show any effect of width on E . However, there is a significant reduction of D value in both configurations of graphene with increasing width, and the reduction in zigzag graphene sheets is much higher than that of armchair graphene sheets.

The effective Young's modulus (E_{eff}) of narrow graphene sheets can be expressed as given in Eq. (3.13). However, this relation has been validated only for E values calculated at low strains ($\varepsilon < 0.005$) [64]. On the other hand, in this work E_{eff} has been calculated by considering nonlinear σ - ε relation of graphene up to fracture. In order to investigate the validity of the relation given in Eq. (3.13), the E values of graphene sheets has been calculated by considering the $U - \varepsilon$ relationship up to a strain value of 0.03, up to which both armchair and zigzag graphene sheets show a similar $U - \varepsilon$ relationships. A quadratic polynomial is fitted on $U - \varepsilon$ data as shown below.

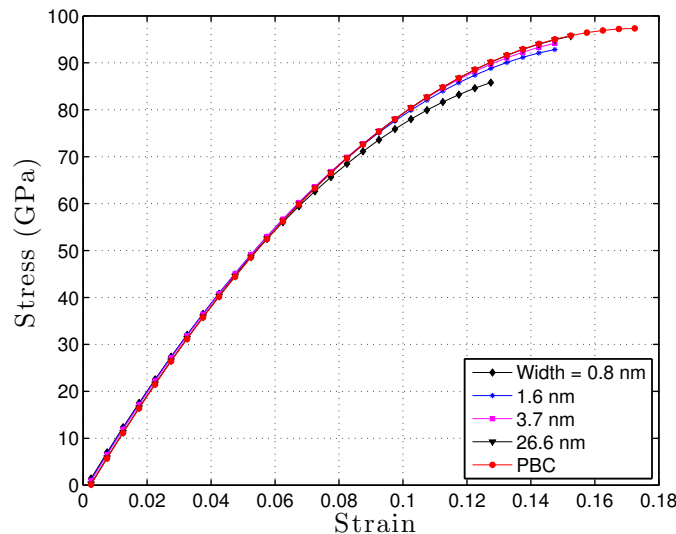
$$U = \frac{E}{2}\varepsilon^2 + C\varepsilon + K \quad (3.17)$$

Figure 3.24 shows that there is a small width effect even in armchair edges at very low strain. This indicates that E value of graphene is slightly sensitive to the method of calculation. Therefore, the method of calculation of E should be considered when comparing various studies.

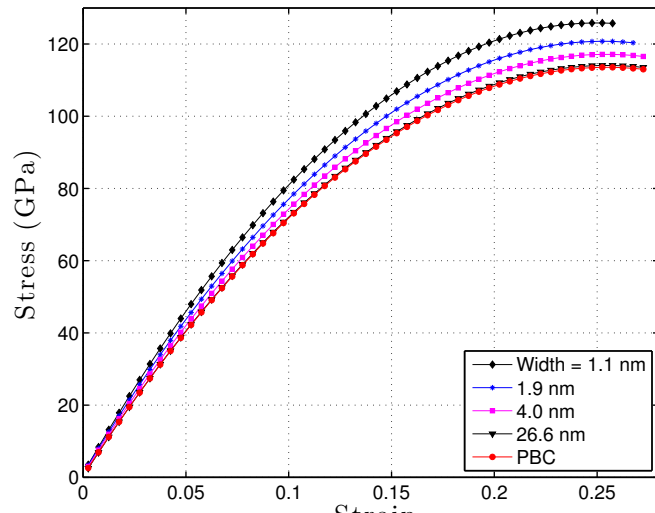
3.2.3 Effect of Temperature on Edge Effect

Effect of temperature on edges is studied by investigating the variation of strength and elastic modulii of graphene sheets at temperatures of 300 K . Fig. 3.25 shows that $\sigma - \varepsilon$ curves become linear at 300 K, due to the fact that graphene sheets fail at lower strains at higher temperatures as observed in Section 3.1. E values of zigzag graphene sheets, shown in Fig. 3.27, demonstrate a similar trend as seen at 1 K with significant fluctuations. Armchair graphene does not show any edge effect as at 1 K. D value of

3.2. Effect of Edges



(a)



(b)

Figure 3.21: Stress strain curves of graphene sheet with different widths at 1 K (a) Armchair (b) Zigzag

3.2. Effect of Edges

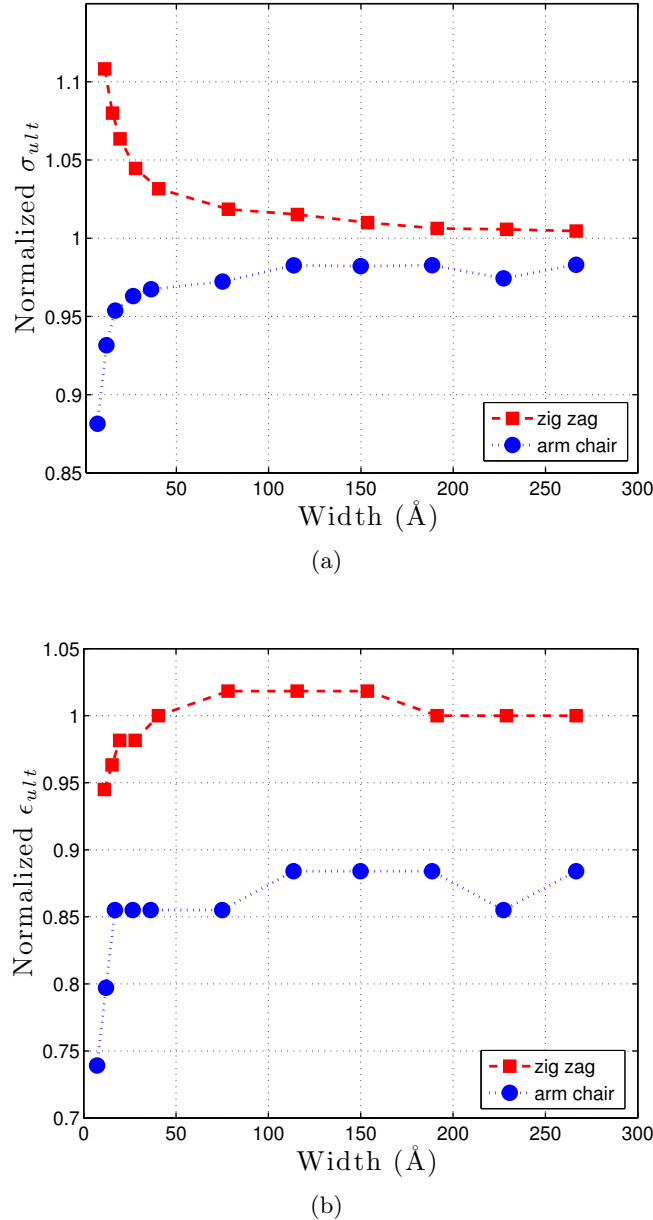
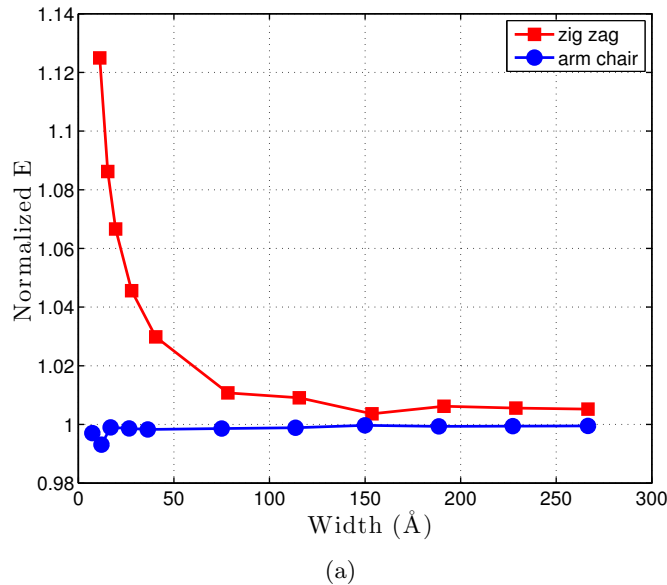
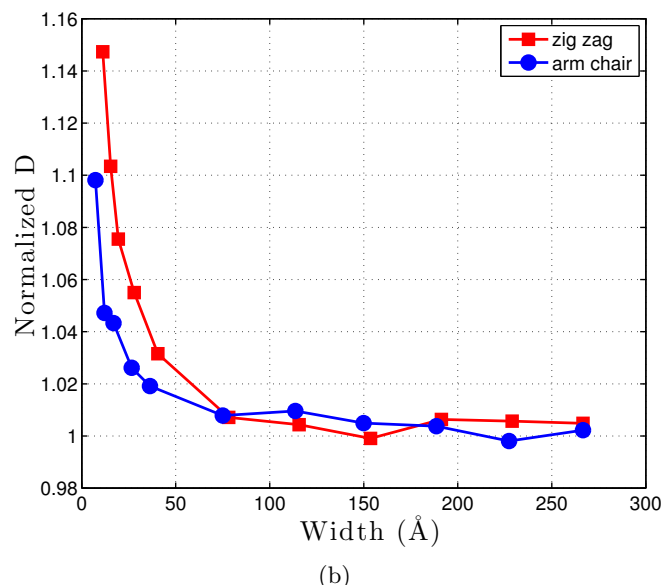


Figure 3.22: Ultimate stress and strain of graphene sheets with different widths at 1 K (a) Ultimate stresses have been normalized with respect to values of PBC graphene, which are 97.3 GPa and 113.6 GPa in armchair sheets and zigzag sheets, respectively. (b) Ultimate strains have been normalized with respect to values of PBC graphene. That are 0.173 and 0.273 GPa in armchair sheets and zigzag sheets, respectively.

3.2. Effect of Edges



(a)



(b)

Figure 3.23: Change of E and D with width of graphene sheet at 1 K (a) E value has been normalized by 0.89 TPa for zigzag graphene and 1.15 TPa by armchair (b) D value has been normalized by -1.74 TPa for zigzag and -3.3 TPa for armchair

3.2. Effect of Edges

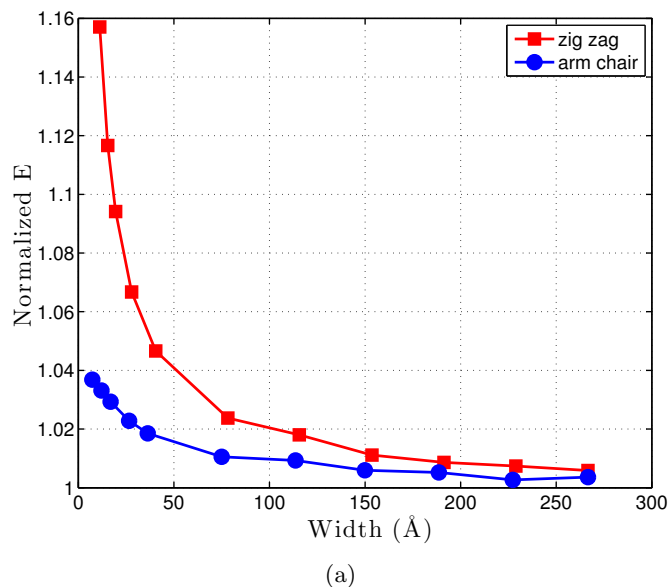


Figure 3.24: E vs width of graphene sheet at 1 K, where E is calculated considering strain up to 0.03. E value has been normalized by 0.83 TPa for zigzag graphene and 0.97 TPa by armchair.

3.3. Effect of Curvature on the Strength of Carbon Nanotubes

zigzag graphene shows a significant width effect at 300 K, whereas D value of armchair graphene doesn't show a consistent width effect.

3.3 Effect of Curvature on the Strength of Carbon Nanotubes

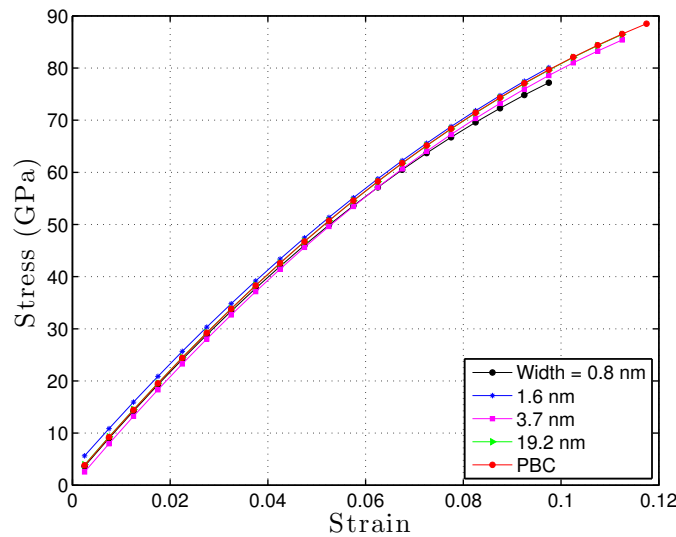
Carbon nanotube can be viewed as a rolled form of graphene. Fig. 3.28 shows armchair and zigzag CNTs. Using *ab initio* methods, Güleren *et al.* [124] and Portal *et al.* [125] showed that the bond lengths and angles of armchair and zigzag CNTs converge at a diameter of 7 Å and 6 Å, respectively. This suggest that there should not be an effect of diameter beyond 7 Å for armchair and zigzag CNTs. Using a nonorthogonal tight-binding formalism, Hernández *et al.* [126] showed that smaller diameter has a bigger influence on the E value of zigzag CNTs compared to armchair CNTs.

The variation of strength properties and elastic moduli of armchair and zigzag CNTs have been studied in this section, and a comparison of effect of diameter with the effect of edges of corresponding graphene sheets have been made. It should be noted that in graphene sheets, strain is applied along the chiral vector, while it is normal to the chiral vector in CNTs. Therefore, armchair graphene should be compared with zigzag CNT and zigzag graphene with armchair CNT.

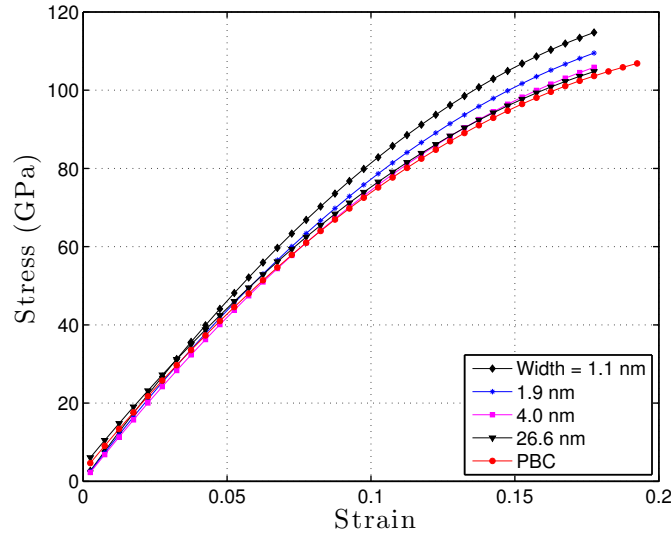
Fig. 3.29 compares armchair and zigzag CNTs with equal diameters. Zigzag CNT stores only about 50% of the strain energy stored in armchair CNT, however the σ_{ult} of zigzag CNT is around 85% of the σ_{ult} of the armchair as seen in the case of graphene. Fig. 3.30(a) shows that zigzag CNTs with various diameters follow a similar σ - ε curve, however, the curves of armchair CNTs cross each other as shown in Fig. 3.30(b). Zigzag CNTs have higher σ_{ult} and ε_{ult} compared to that of the armchair graphene sheet. Both CNTs have a small diameter effect on the modulii as shown in Fig 3.31.

It can be seen in Fig. 3.27 and Fig 3.31, both armchair CNTs and zigzag graphene sheets show diameter/width effect on E , but the trends are in reverse order. In zigzag sheets, E decreases with width, while it increases

3.3. Effect of Curvature on the Strength of Carbon Nanotubes



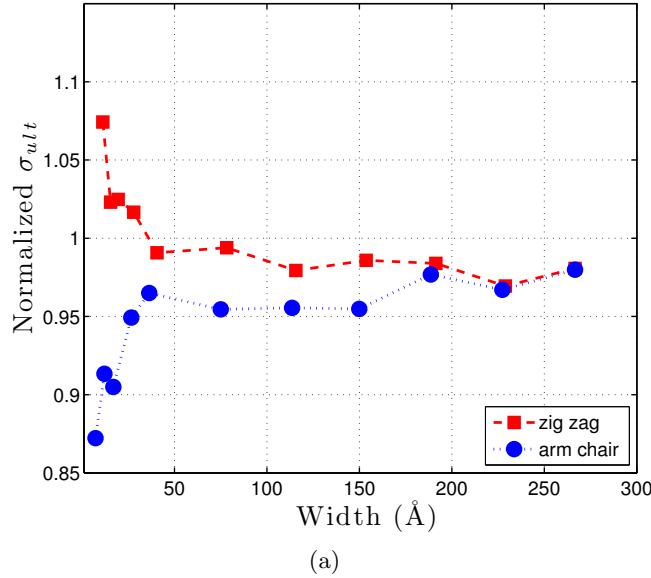
(a)



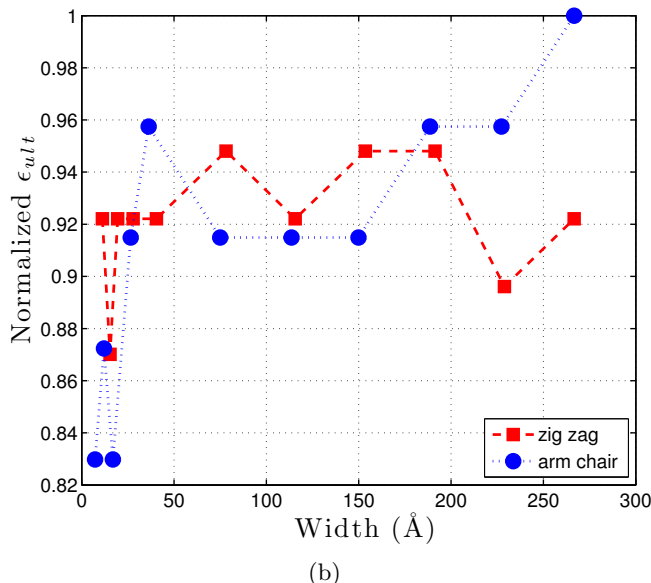
(b)

Figure 3.25: Stress strain curves of graphene sheet at 300 K (a) armchair (b) zigzag.

3.3. Effect of Curvature on the Strength of Carbon Nanotubes



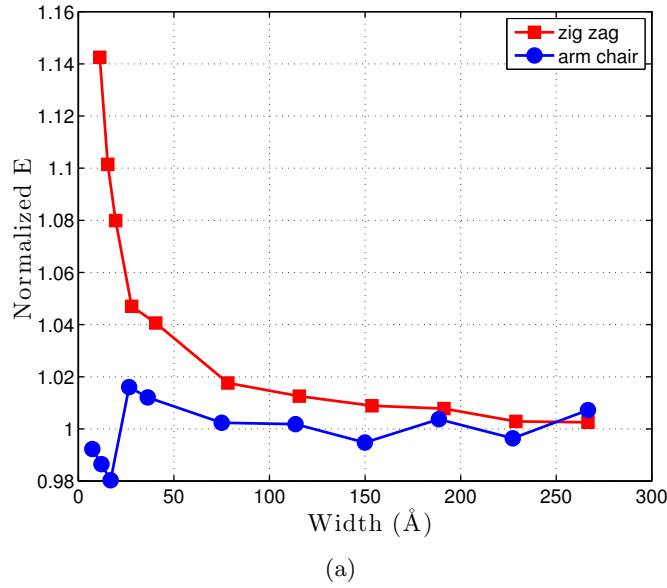
(a)



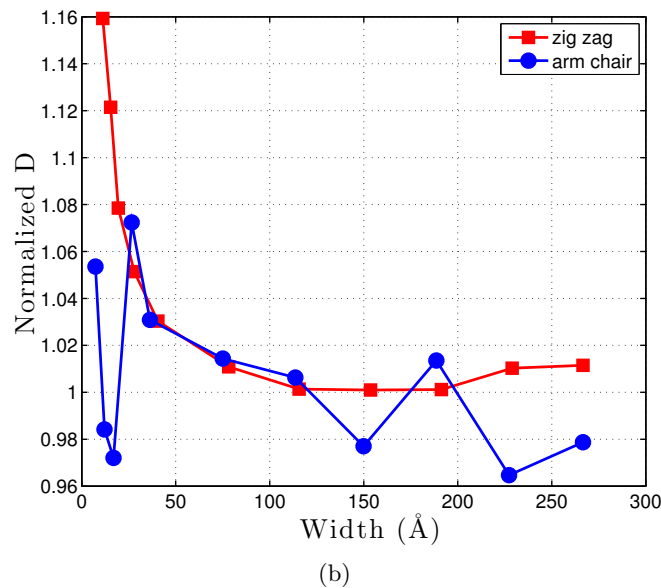
(b)

Figure 3.26: Ultimate stress and strain of graphene sheets with different widths at 300 K (a) Ultimate stresses have been normalized with respect to values of PBC graphene. That are 88.5 GPa and 106.8 GPa in armchair sheets and zigzag sheets, respectively. (b) Ultimate strains have been normalized with respect to values of PBC graphene. That are 0.118 and 0.193 GPa in armchair sheets and zigzag sheets, respectively.

3.3. Effect of Curvature on the Strength of Carbon Nanotubes



(a)



(b)

Figure 3.27: Change of E and D with width of graphene sheet at 300 K (a) E value has been normalized by 0.90 TPa for zigzag graphene and 1.11 TPa by armchair (b) D value has been normalized by -1.86 TPa for zigzag and -3.11 TPa for armchair

3.4. Conclusions

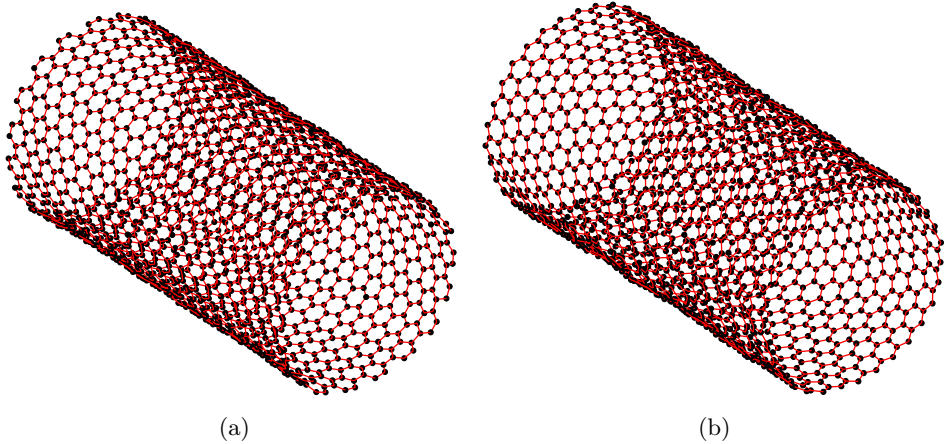


Figure 3.28: CNTs with a diameter of 24 Å (a) Armchair (b) Zigzag.

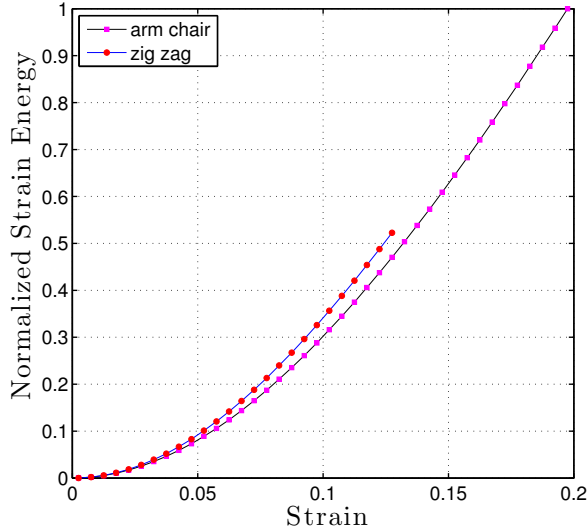
with diameter of armchair CNT. This indicates that the effect of curvature on E is higher than that of edges. However, E values reach the value of infinitely large zigzag graphene sheet as width/diameter increases. The value of D of zigzag graphene and armchair CNT show a similar variation.

3.4 Conclusions

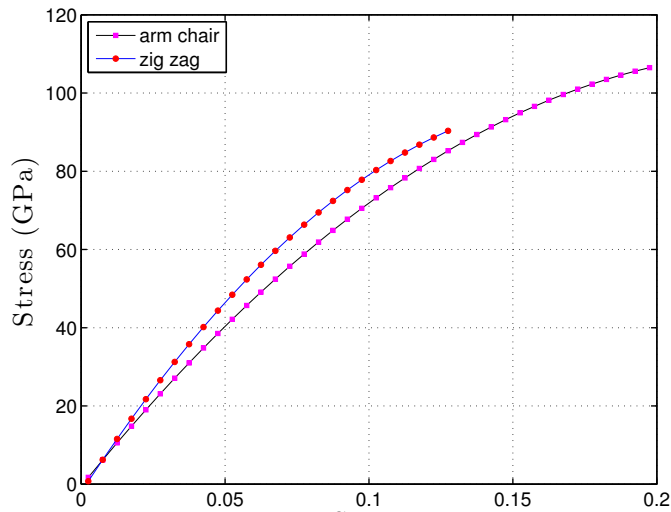
The investigation on the effects of temperature on graphene sheets revealed that the C-C bond length of graphene increases with temperature and graphene sheets at higher temperatures fails at lower strains. It has also been observed that the continuum stress measure is unable to capture stress-strain relation of graphene at higher temperatures, where as virial stress measure is accurate at higher temperatures.

A study on the edges of graphene showed that excess edge energy of graphene sheets induce an initial strain on the graphene sheets. Free edges has a greater influence on the mechanical properties of zigzag graphene sheets compared to armchair graphene sheets. Diameter of CNTs do not have effect on the mechanical properties when diameter is greater than 10 Å.

3.4. Conclusions



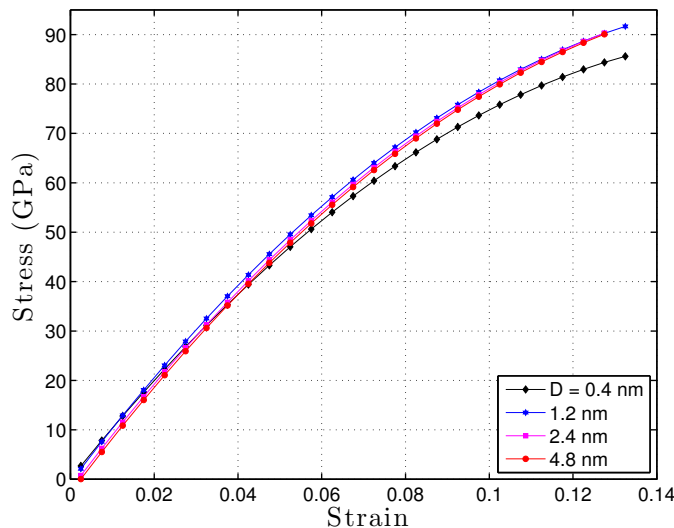
(a)



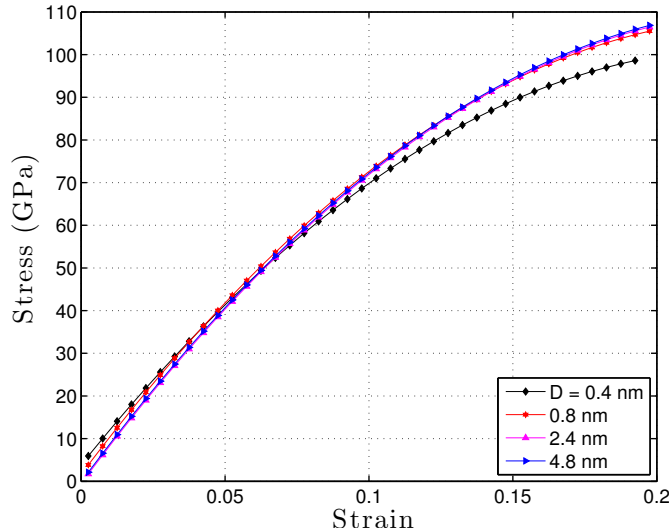
(b)

Figure 3.29: Comparison of CNTs with diameters of 24 Å (a) Strain energy versus strain. Strain energy has been normalized with respect to the maximum strain energy stored in armchair CNT that is $1.29 \times 10^{10} J/m^3$ (b) Stress-strain curves. Simulation was done at 300 K

3.4. Conclusions



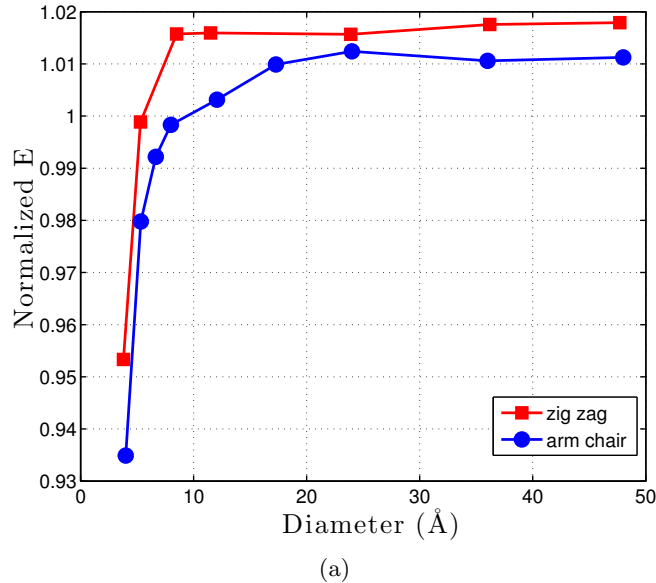
(a)



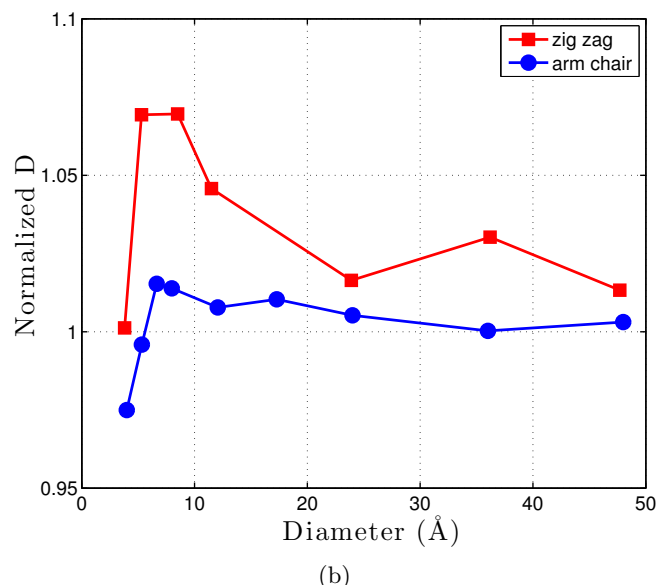
(b)

Figure 3.30: Stress strain curves for CNTs with different diameters (a) Zigzag (b) Armchair. Simulation was done at 300 K

3.4. Conclusions



(a)



(b)

Figure 3.31: Change of E and D of CNTs with different diameters (a) E value has been normalized by 0.90 TPa for armchair CNTs and 1.11 TPa by zigzag (b) D value has been normalized by -1.86 TPa for armchair and -3.11 TPa for zigzag

Chapter 4

Fracture of Defective Graphene

4.1 Introduction

As in many crystalline materials, defects are unavoidable in graphene during production and device fabrication stages. Researchers have found experimental evidences for the existence of geometric defects such as vacancy defects in graphene sheets [69, 127]. Theoretical studies have shown that defects significantly alter the mechanical and electronic properties of graphene [67, 68, 71, 72, 128–130]. On the other hand, understanding the fracture of a graphene sheet, which is one atom thick planar sheet, could give an insight to the fracture of crystalline materials at macroscale. Therefore, it is of interest to investigate the fracture of defective graphene sheets. The first part of this chapter presents a study of the effect of vacancy defects on the strength of graphene sheets. The second part investigates the applicability of the continuum fracture mechanics to calculate the strength of defective graphene sheets.

4.2 Effects of Vacancy Defects

Experimental investigations by using an atomic force microscope (AFM) have revealed that the ultimate tensile strength (σ_{ult}) and Young's modulus of graphene are around 130 GPa and 1 TPa, respectively [15]. However, vacancy defects could reduce the strength of graphene by around 50% [67, 68, 71, 72, 128–130]. The vacancy defects have a greater influence on the mechanical properties of graphene compared to other geometric defects such

4.2. Effects of Vacancy Defects

as StoneWales defects [68]. This section presents a detailed study of the effect of vacancy defects on mechanical properties of armchair and zigzag graphene sheets using MD simulations.

Cleri *et al.* [131] suggested that the size of simulation box should be greater than 10 times of the crack length in order to avoid finite-size effect. This rule has been implemented in the simulations of [71, 132]. The MD simulations presented in this chapter have been conducted with PBCs where the edges of the graphene sheet do not have any influence on the simulation results. However, the finiteness of sheet could have an effect on the MD simulations with cracks. In order to investigate the effect of finiteness, a set of armchair sheets of various sizes were subjected to uniaxial tensile test at a temperature of 300 K. A crack of length 1.4 nm has been introduced in the centre of sheets by removing 9 carbon atoms. Some graphene sheets used for this investigation are shown in Fig. 4.1.

Effect of the size of sheet on the stress-strain relation of graphene sheets is shown in Fig. 4.2. Stress of the sheet is obtained using the relationship between strain energy (U), stress (σ) and strain (ϵ) given in Eq. (3.4) and Eq. (3.6). As shown in Fig. 4.2, the $5 \text{ nm} \times 5 \text{ nm}$ graphene sheet is less stiff compared to the larger graphene sheets since the reduction of cross section due to crack is quite significant at this size. However, the $5 \text{ nm} \times 5 \text{ nm}$ graphene sheet withstands higher strain compared to the larger graphene sheets, and it stores a higher amount of strain energy up to fracture. As strain increases, the crack opening increases, and this helps the graphene sheet to withstand higher strain. It can be seen in Fig. 4.2 that the σ - ϵ curves converge as the size of graphene sheet reaches 10 times the crack width, which is $14.5 \text{ nm} \times 14.5 \text{ nm}$. Therefore, the size of the square graphene sheets were chosen to be more than 10 times of the crack width for the simulations presented hereafter.

In order to investigate the effect of crack length on the σ_{ult} and the Young's modulus of graphene sheet, a set of MD simulations were performed on armchair and zigzag sheets with various crack lengths ranging from 4 \AA to 29 \AA . The crack length and crack tip radius of the sheets are defined as shown in Fig. 4.3. MD simulations were performed for each crack length at

4.2. Effects of Vacancy Defects

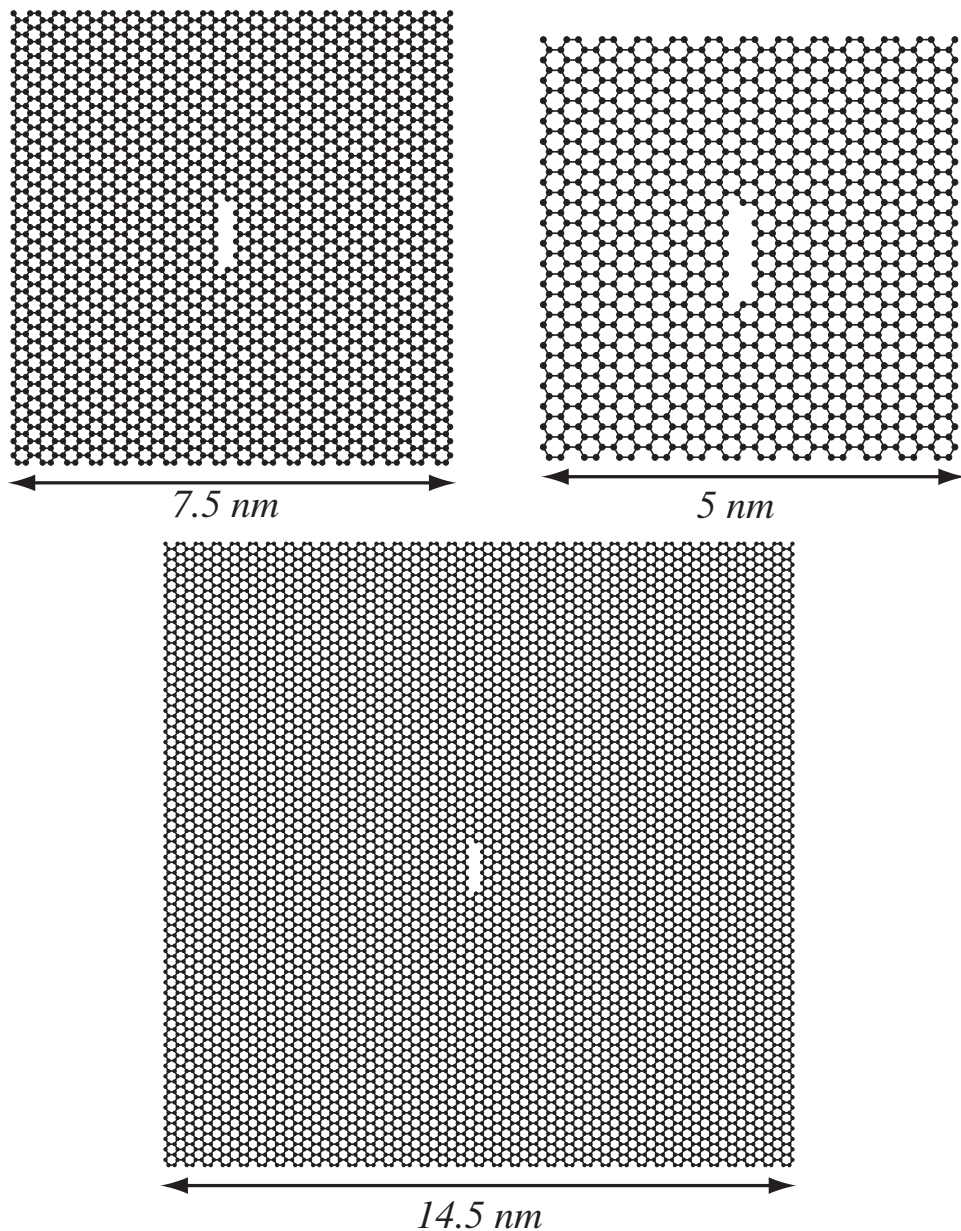


Figure 4.1: Different sizes of square graphene sheets used to investigate the effect of finiteness.

4.2. Effects of Vacancy Defects

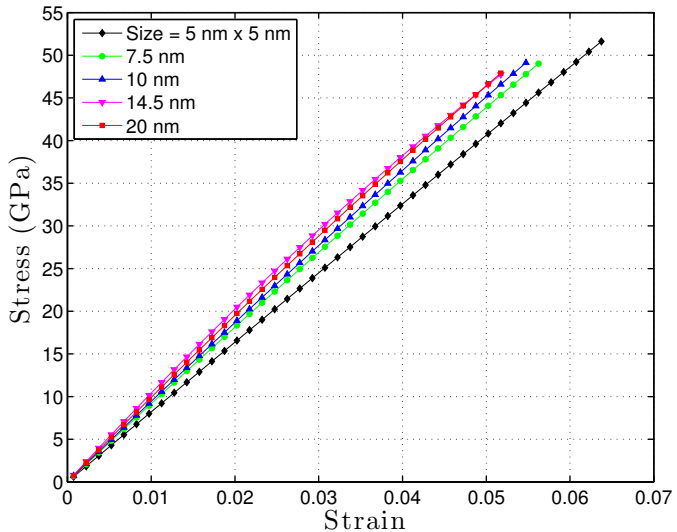


Figure 4.2: σ - ε relation of square graphene sheets with various sizes and a crack of width 1.4 nm in the centre.

temperatures of 1 K and 300 K to investigate the effect of temperature on the mechanical properties of defective sheets.

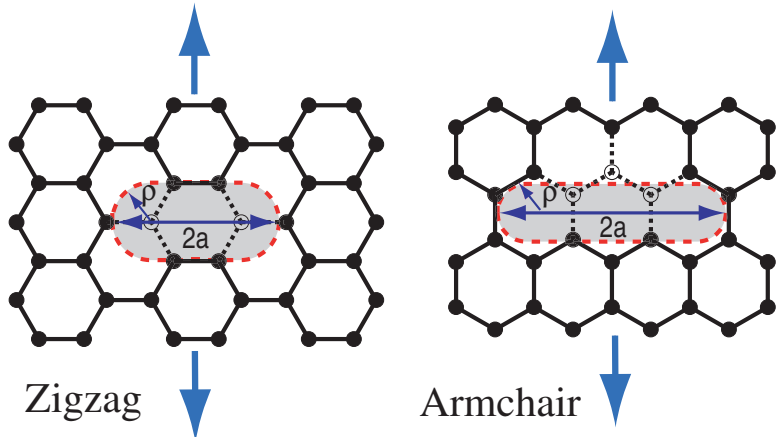


Figure 4.3: Crack length ($2a$) and crack tip radius (ρ) graphene sheets. Arrows indicate the straining direction.

4.2. Effects of Vacancy Defects

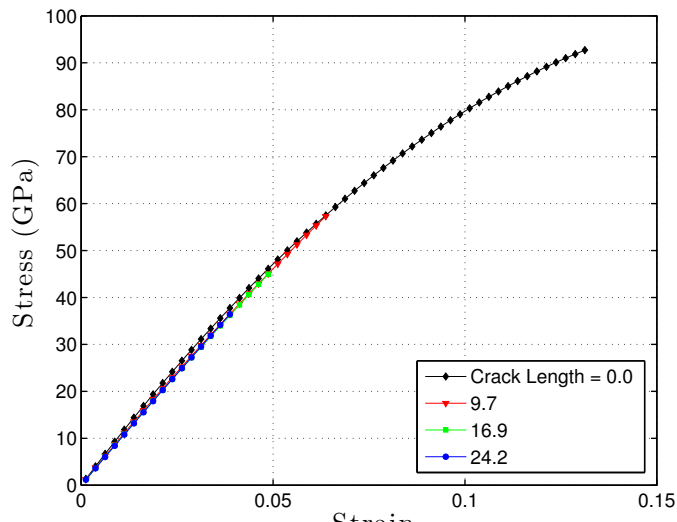
Stress-strain curves of sheets with various crack lengths at 300 K are given in Fig. 4.4. The results reveal that a single vacancy (one missing atom) reduces σ_{ult} in armchair sheet by 15.7% and in zigzag sheet by 23.3%, which indicates that graphene is very sensitive to defects. Therefore, it is necessary to produce defects free sheets for structural applications. It can also be noticed that the Young's modulus of sheets has not been affected by the crack length.

As the crack length increases, the rate of reduction in σ_{ult} decreases as shown in Fig. 4.5. Khare *et al.* [71] observed a similar variation in σ_{ult} with crack length. They used a coupled quantum mechanical/molecular mechanical method, which is computationally expensive compared to MD. On the other hand, they have only investigated the effect of crack in zigzag direction. Figure 4.5 shows that σ_{ult} of graphene sheet decreases at 300 K, and the effect of temperature on zigzag sheets are slightly higher compared to that of armchair sheets. Effect of temperature on the strength of pristine armchair and zigzag sheets are almost same as shown in Fig. 3.10. This indicates that vacancy defect enhances the temperature effect on zigzag graphene. On the other hand, the study in Section 3.2 indicates that edges have greater influence on the mechanical properties of zigzag sheet. Therefore, zigzag sheet is more vulnerable to geometric defects compared to armchair sheet.

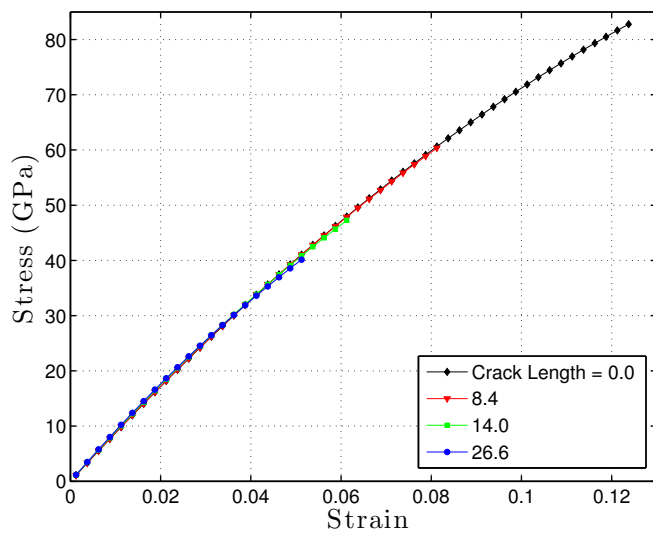
Figure 4.6 and Fig.4.7 show the fracture of armchair and zigzag sheets, respectively. The temperature in simulation is 1 K, and both the sheets have a single vacancy defect at the centre. Size of the sheets are 20 nm \times 20 nm each. Fracture of armchair sheet occurs perpendicular to strain direction, while that is at an angle of 60⁰ to the strain direction for zigzag sheet as explained in Section 3.1.

It was also noticed that as strain of the sheet increases, the crack tips come out of the plane of sheet, which eventually generate ripples in the sheet. Fig. 4.8 shows the variation in the geometry of a 27 nm \times 27 nm sheet as strain increases. The size of the crack is 2.7 nm. The crack tips can be considered as free edges, and these free edges get buckled even at the equilibrium state due to the forces acting on the edge atoms as explained in Chapter 3. As shown in Fig. 4.8, the out-of-plane deformation of the

4.2. Effects of Vacancy Defects



(a)



(b)

Figure 4.4: Stress - strain curve for graphene sheets with crack length. (a) and (b) for armchair and zigzag graphene sheets at 300 K, respectively.

4.3. Continuum Fracture Mechanics Approaches

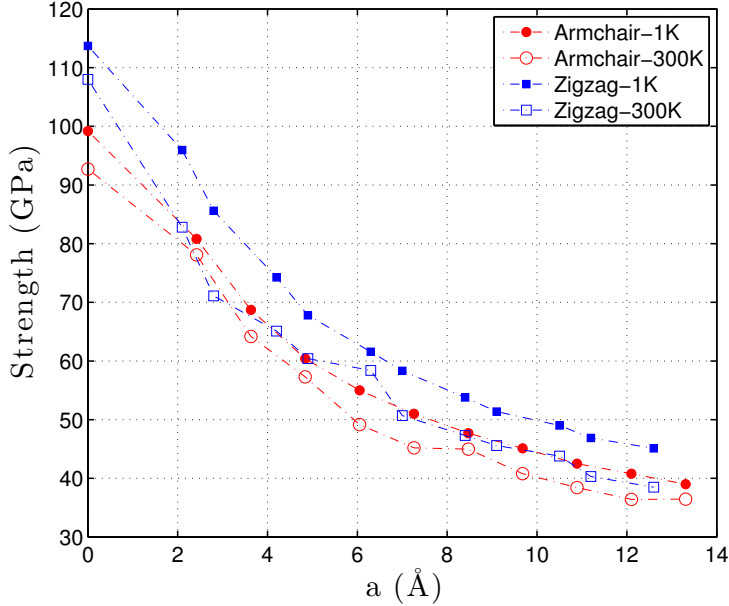


Figure 4.5: Comparison of ultimate strength of graphene at various crack lengths.

crack tip at equilibrium configuration is localized around the crack tip, and the average out-of-plane movement of the atoms are almost zero due to the shape. However, as strain increases up to 0.018, the shape of the crack tip changes, and the new configuration has a net out-of-plane movement of atoms, which acts as a localized ripple. As strain increases up to 0.0235, this localized ripple spreads throughout the graphene sheet.

4.3 Continuum Fracture Mechanics Approaches

The two fundamental theories in fracture mechanics were proposed by Inglis and Griffith. In 1913, Inglis mathematically derived the stress concentration around an elliptical hole in a linearly elastic field [133]. This was followed by the Griffith's work on the fracture of brittle solid in 1921 [75]. This section gives an overview of the theories proposed by Inglis and Griffith.

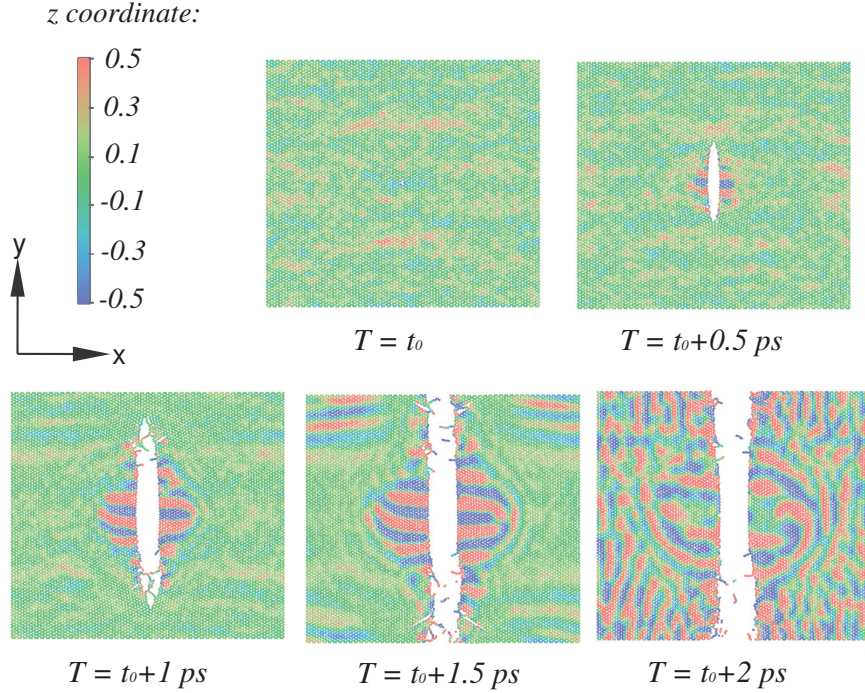


Figure 4.6: Fracture of armchair graphene sheet. Strain has been applied along x direction.

In Section 4.3.3, the strength of defective graphene sheets given by the two theories are compared with the results obtained from MD simulations.

4.3.1 Inglis' Local Stress

Inglis introduced the concept of stress concentration at an elliptical hole of a plate, which deforms linearly elastically. The length and width of the hole are taken as $2a$ and $2b$, respectively, as shown in Fig. 4.9. The length and width of the plate are assumed to be much larger compared to the size of the elliptical hole. The stress at crack tip (point A) is given by

$$\sigma_A = \sigma \left(1 + \frac{2a}{b} \right). \quad (4.1)$$

Inglis expressed Eq. (4.1) in terms of the radius of curvature ρ as

4.3. Continuum Fracture Mechanics Approaches

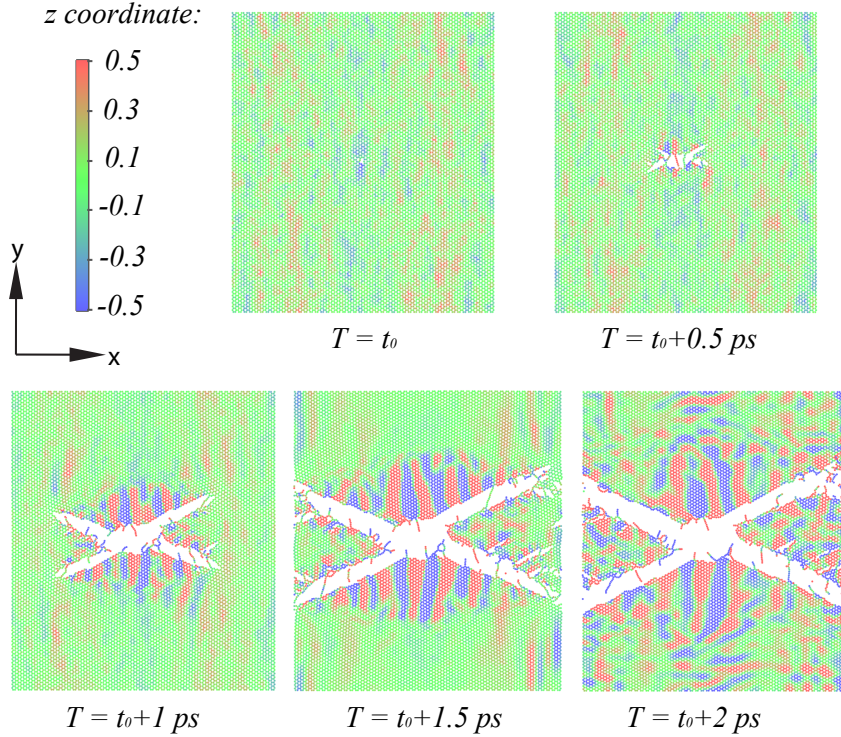


Figure 4.7: Fracture of zigzag graphene sheet. Strain has been applied along y direction.

$$\sigma_A = \sigma \left(1 + 2\sqrt{\frac{a}{\rho}} \right), \quad (4.2)$$

where $\rho = b^2/a$. When $a \gg b$, Eq. (4.2) becomes

$$\sigma_A = 2\sigma \sqrt{\frac{a}{\rho}}. \quad (4.3)$$

Eq. (4.3) gives an infinite stress at the tip of infinitely sharp crack ($\rho \approx 0$). However, infinitely sharp crack is not possible in real materials. As an example, metal shows a plastic deformation at the crack tip, which blunts the crack tip. The smallest possible ρ is in the order of inter atomic distance, r_0 . Therefore, the stress concentration at an atomistically sharp crack can

4.3. Continuum Fracture Mechanics Approaches

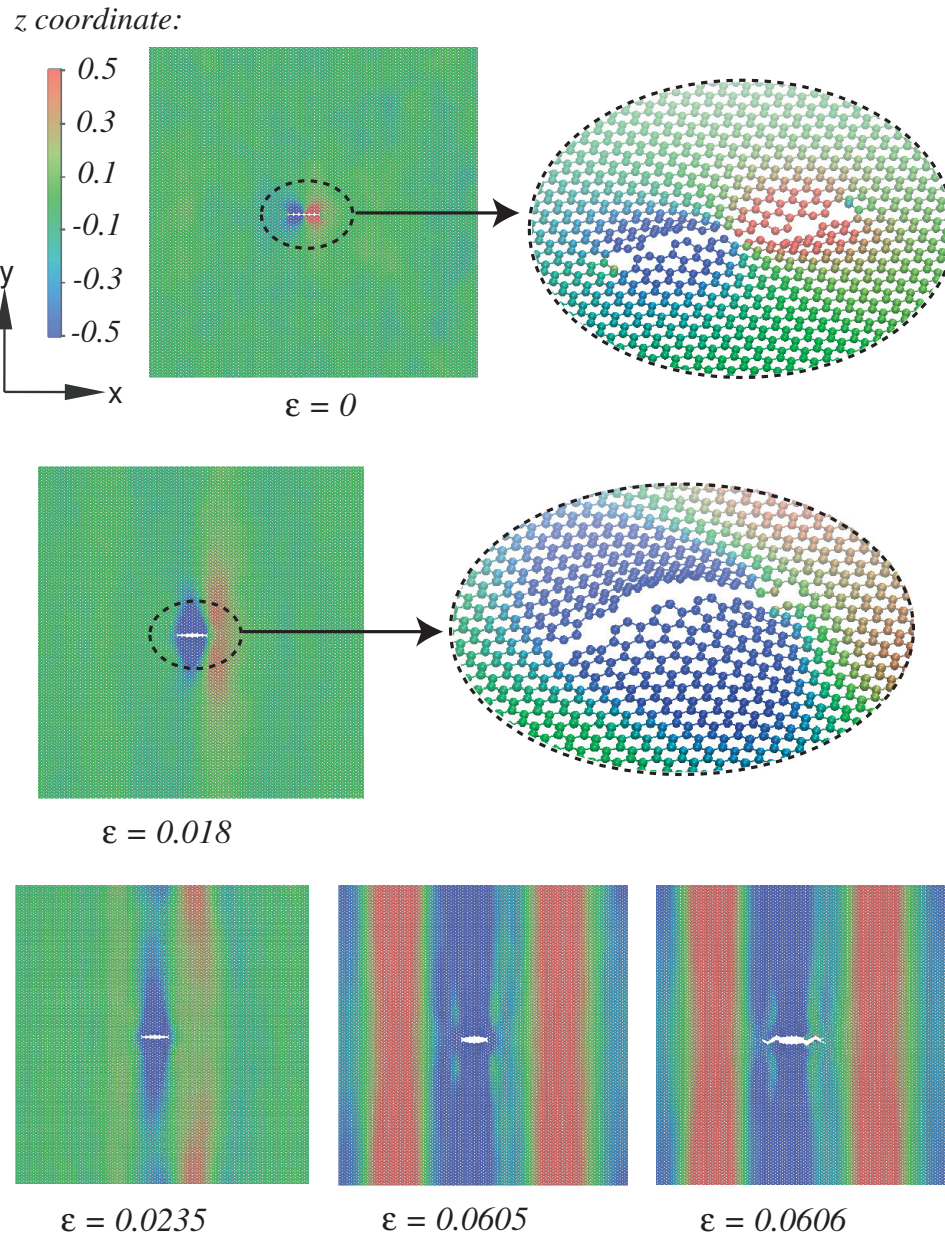


Figure 4.8: Ripples in defective graphene sheet. Strain has been applied along y-direction.

4.3. Continuum Fracture Mechanics Approaches

be written as

$$\sigma_A = 2\sigma \sqrt{\frac{a}{r_0}}. \quad (4.4)$$

Fracture strength, σ_c , of a bond at atomic scale can be written as [134]

$$\sigma_c = \sqrt{\frac{E\gamma_s}{r_0}}, \quad (4.5)$$

where E is the Young's modulus and γ_s is the surface energy.

Combining Eq. (4.4) and Eq. (4.5), the remote stress at failure (σ_f) can be expressed as

$$\sigma_f = \sqrt{\frac{E\gamma_s}{4a}}. \quad (4.6)$$

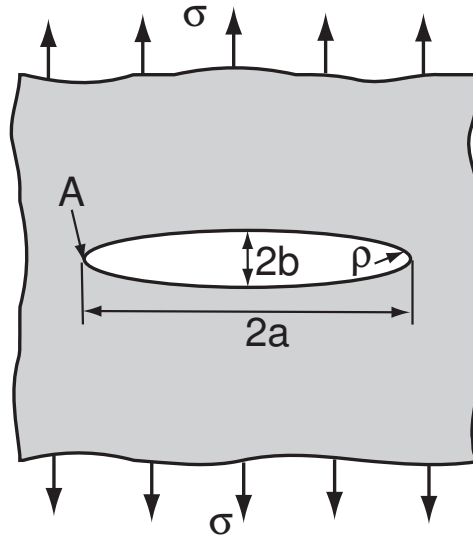


Figure 4.9: Parameters of an elliptical crack.

4.3.2 Griffith's Energy Balance

The infinite stress at a tip of a sharp crack in Inglis' local stress approach motivated Griffith to develop a fracture theory based on energy [75]. Griffith

4.3. Continuum Fracture Mechanics Approaches

showed that an existing crack can propagate only if such a process causes the total energy to decrease or remain constant. The theory can be summarized as below.

The surface energy increase, ΔE_s , by propagating a crack with a length of $2a$ (Fig. 4.9), can be written as

$$\Delta E_s = 4a\gamma_s, \quad (4.7)$$

where γ_s is the surface energy per unit area. The thickness of the plate is assumed to be unity. It should be noted that the crack of length $2a$ creates two free surfaces. Therefore, free surface area is equal to $4a$.

In linear elasticity, the change in energy, (ΔE_e) , due to the advancement of the crack can be written as

$$\Delta E_e = -\pi \frac{\sigma^2}{E} a^2, \quad (4.8)$$

where σ and E are the stress of the plate and the Young's modulus, respectively. Therefore, the change in the total energy, ΔE_{tot} , due to the advancement of the crack can be expressed as the summation of Eq. (4.7) and Eq. (4.8),

$$\Delta E_{tot} = 4a\gamma_s - \pi \frac{\sigma^2}{E} a^2. \quad (4.9)$$

The stationary point of ΔE_{tot} , which is a maximum, occurs at critical value of a , a_c , given as

$$a_c = \frac{2\gamma_s E}{\pi\sigma^2}. \quad (4.10)$$

When $a_c > a$, ΔE_{tot} get reduced with the reduction of crack length. This can be achieved by healing the crack, which is not so common. When $a_c < a$, ΔE_{tot} get reduced with increasing crack length. Therefore, the failure stress of a sheet, σ_f , with a crack length of $2a$ can be expressed as

$$\sigma_f = \sqrt{\frac{2\gamma_s E}{\pi a}}. \quad (4.11)$$

4.3. Continuum Fracture Mechanics Approaches

According to the Griffith's model, fracture occurs only when the energy stored in the structure is sufficient to overcome the surface energy of the material. However, the fracture occurs by breaking individual bonds. In order to break individual bonds, the stress of bonds should be greater than the ultimate strength of bonds. It can be seen in Eq. (4.5) and Eq. (4.11) that Inglis' value of σ_f is 37% less than that of Griffith's one. The applicability of Inglis' theory at atomistic scale is questionable since the shape of crack alters with the applied strain as seen in Fig. 4.8.

4.3.3 Comparison of Continuum Approaches with MD

The value of γ_s in Eq. (4.6) and Eq. (4.11) was calculated by dividing the difference in energy of a graphene sheet before and after fracture by the area of newly created surface [71], as graphically represented in Fig. 4.10. The value of γ_s is similar for both armchair and zigzag graphene sheets since the distance between two broken C-C bonds are similar in both graphene sheets. The Young's modulus was calculated from the σ - ε curve of pristine graphene sheets.

A comparison of strength of graphene sheets with various crack widths is given in Fig. 4.11. The strength of graphene sheets are always between the values given by Inglis' and Griffith's approaches, where Griffith's approach sets the upper bound for strength. The strength of graphene sheets at 300 K shows a slight fluctuation due to kinetic energy of atoms. Strength of graphene sheets given by MD simulations and continuum theories asymptote to a certain value as crack length increases. The curves indicate that the strength reaches to a stationary value as crack length increases. It should be noted that the fracture strength predicted by Inglis's and Griffith's theories assume linear elastic material behaviour, whereas graphene is a non-linear elastic material.

However, it should be noted that the Young's modulus of graphene is strain dependent. The strain dependent Young's modulus of armchair and zigzag graphene sheets can be expressed as $E(\varepsilon) = -5.886\varepsilon + 1.081$ TPa and $E(\varepsilon) = -3.504\varepsilon + 0.893$ TPa, respectively. However, Eq. (4.6) and

4.3. Continuum Fracture Mechanics Approaches

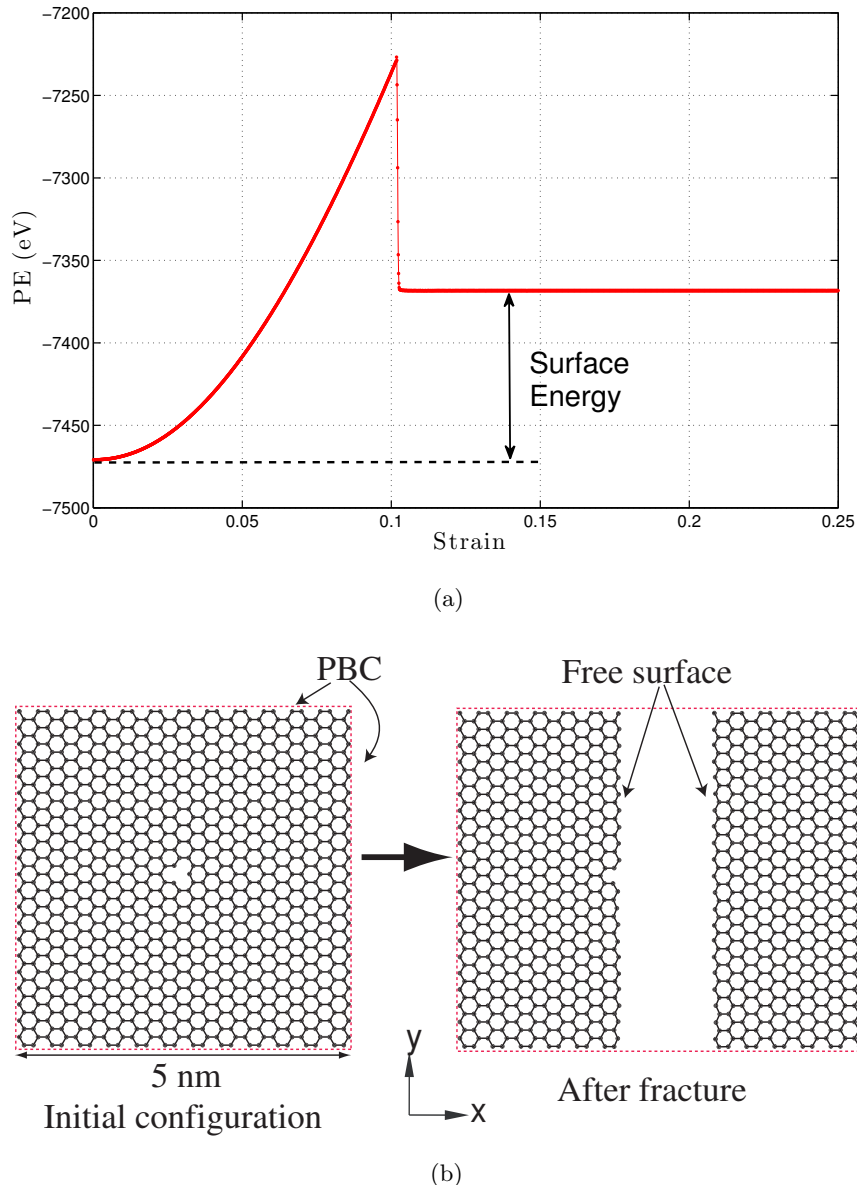


Figure 4.10: Calculation of γ_s . (a) Potential energy vs strain curve of the graphene sheet shown in (b).

4.3. Continuum Fracture Mechanics Approaches

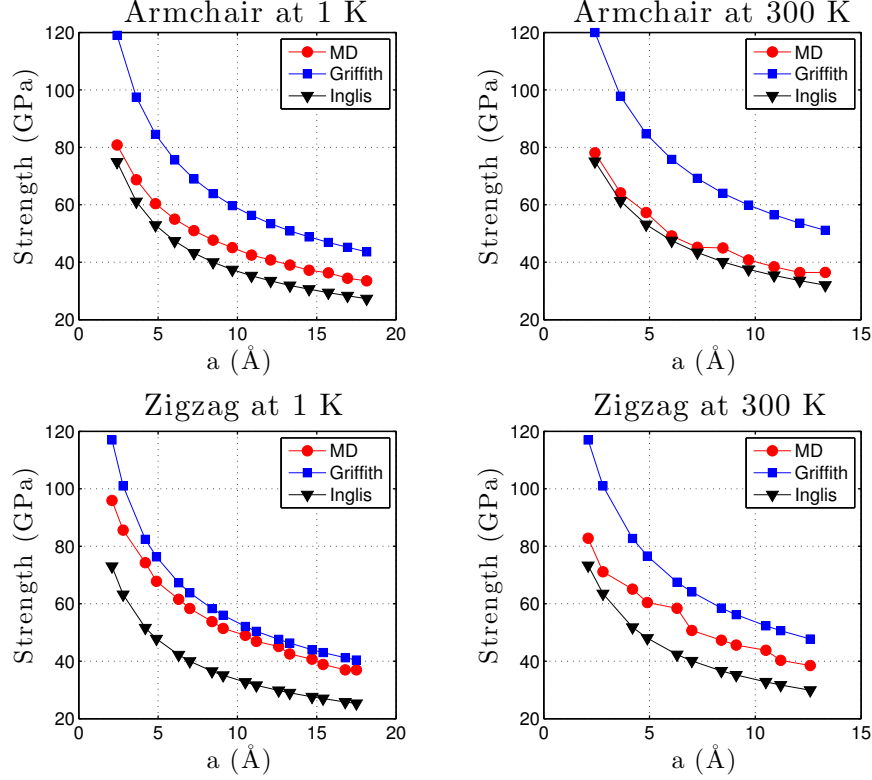


Figure 4.11: Comparison of Inglis' and Griffith's theories with MD.

Eq. (4.11) assume a constant Young's modulus. Therefore, the proper value of the Young's modulus is the Young's modulus at fracture. Considering this fact, Eq. (4.6) and Eq. (4.11) can be modified as

$$\sigma_f = \sqrt{\frac{E(\varepsilon_f)\gamma_s}{4a}} \text{ and} \quad (4.12)$$

$$\sigma_f = \sqrt{\frac{2E(\varepsilon_f)\gamma_s}{\pi a}}, \quad (4.13)$$

where $E(\varepsilon_f)$ is the Young's modulus at fracture.

Comparison of the strength values given by MD simulations, Eq. (4.12),

4.4. Conclusions

and Eq. (4.13) are compared in Fig. 4.12. It can be seen that Griffith's theory gives much closer strength value compared to Inglis' theory. The strength of zigzag graphene sheets given by Griffith and MD simulations agree quite well with each other. However, both Inglis' and Griffith's theories have been derived for a flat plate like structure. Graphene sheet does not remain flat as shown in Fig. 4.8. On the other hand, both the theories assume the continuity of the material, which is not the case in graphene. Therefore, a perfect agreement between continuum theories and MD simulations cannot be expected. However, MD simulations clearly show a square-root singularity of the strength values at 1 K as shown in Fig. 4.13. Equations of trend lines are $\sigma_{ult} = 120.9(1/\sqrt{a}) + 5.7$ ($R^2 = 1$) and $\sigma_{ult} = 139.7(1/\sqrt{a}) + 4.7$ ($R^2 = 1$) for armchair and zigzag sheets, respectively.

4.4 Conclusions

Finiteness of a defective graphene sheet has a significant influence on the MD simulations. A crack with length of 2.5 nm reduces the strength of both armchair and zigzag graphene sheets by around 50%. Strength of graphene sheets given by Griffith's theory reasonably agree with strength obtained from MD simulations. Crack tip shows an out-of-plane deformation at equilibrium configuration. This deformation propagates with the applies strain and eventually generate ripples in the sheet. Strength obtained from MD simulations shows a square-root singularity, which is expected in continuum fracture mechanics theories.

4.4. Conclusions

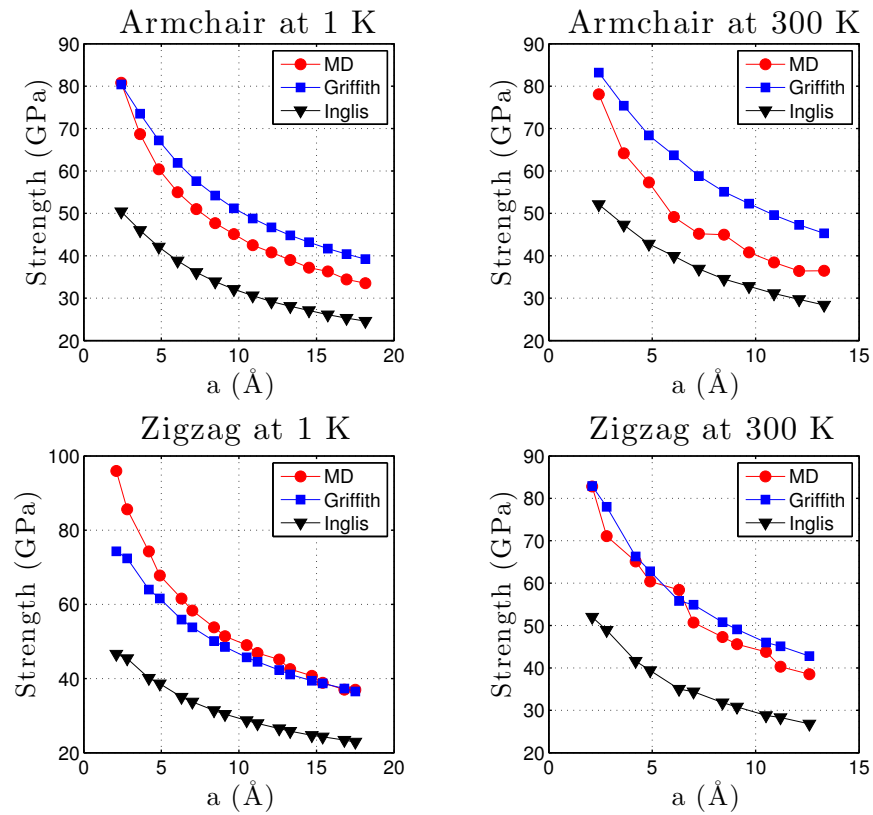


Figure 4.12: Comparison of Inglis' and Griffith's theories with MD simulations. Tangent modulus of a pristine graphene sheet at the fracture strain of defective graphene sheet was used for Inglis' and Griffith's theories.

4.4. Conclusions

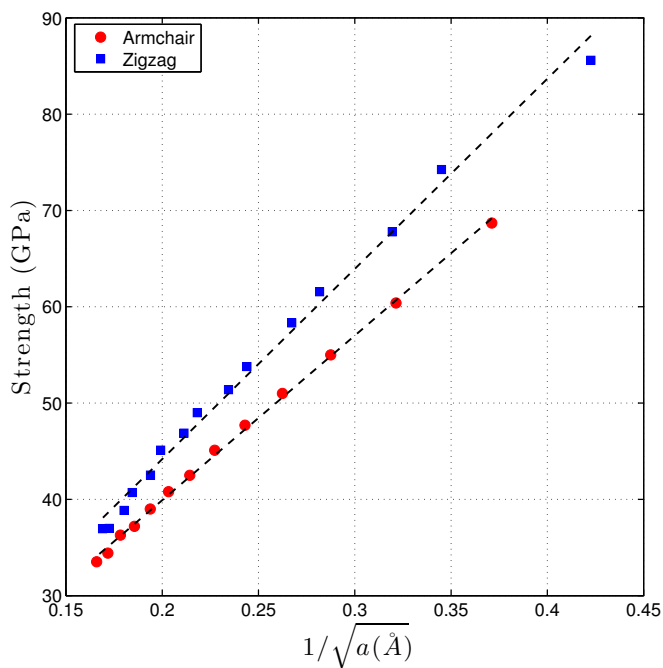


Figure 4.13: Square-root singularity of the strength of graphene.

Chapter 5

Summary and Conclusions

5.1 Summary of the Present Work and Major Findings

1. The effects of temperature on graphene have been investigated. The results revealed that graphene sheet expands with increasing temperature. It has also been observed that the amplitude of intrinsic ripples, which are out-of-plane movements of carbon atoms, in graphene also get increase with increasing temperature. These ripples reduce the net effect of thermal expansion. Graphene sheets at higher temperatures fail at lower strains due to higher kinetic energy of atoms. It has also been found that the continuum stress measure is unable to capture stress-strain relation of graphene at higher temperatures, whereas virial stress is accurate at higher temperatures.
2. A study on the effect of edges on the mechanical properties of graphene sheets showed that excess edge energy of a sheet induces an initial strain at the equilibrium configuration. However, free edges have an influence on the atoms up to 5 Å normal to the edges. The effect of free edges on mechanical properties of zigzag sheet is higher than that of armchair sheet.
3. Effect of vacancy defects on the strength of graphene sheets have been investigated. It was found that finiteness of a defective graphene sheet has a significant influence on the MD simulations. The length and the width of the graphene sheet should be longer than 10 times the crack length in order to eliminate the effect of finiteness. MD simulation results indicated that

5.2. Suggestions for Future Work

vacancy defect can reduce the strength of graphene sheet by around 60%. A single vacancy defect (one missing atom) could reduce the strength of graphene sheet by around 20%. Therefore, it is very important to minimize the defects in graphene sheets during production stage, specially for sheets which will be used for structural applications. It has also been observed that strength of defective sheets calculated by Griffith's theory reasonably agree with strength obtained from MD simulations.

5.2 Suggestions for Future Work

1. This thesis is mainly focused on the effect of pristine edges. However, it has been found that hydrogen passivation of edge atoms make edges much more stable than the pristine edges. Also, it has been found that at finite temperatures, armchair edge transforms to a zigzag edge due to stability of the latter. Therefore, a study of the effect of edge defects such as edge transformation and hydrogen passivation will give an overall picture of the effects of edges on mechanical properties of graphene.
2. Continuum stress interpretation is unable to capture the local stress distribution around a crack of a graphene sheet. In fact, virial stress is also not a good stress measure to calculate local atomic stresses. Investigation of stress concentration around the crack tip of a graphene sheet can give a better understanding of the effect of defects.
3. Griffith's theory for a linear elastic material is able to predict the strength of graphene sheet with reasonable accuracy. However, graphene is a non-linear material. Therefore, non-linear fracture mechanics approaches such as J-integral and crack-tip opening displacement methods will be able to explain the fracture of graphene sheet better.

Bibliography

- [1] R. Williams and P. Alivisatos, *Nanotechnology Research Directions: IWGN Workshop Report: Vision for Nanotechnology in the Next Decade*. Cambridge: Springer, 2000.
- [2] R. P. Feynman, “There’s plenty of room at the bottom [data storage],” *Microelectromechanical Systems, Journal of*, vol. 1, pp. 60 –66, mar 1992.
- [3] G. Binnig, H. Rohrer, C. Gerber, and E. Weibel, “Surface studies by scanning tunneling microscopy,” *Phys. Rev. Lett.*, vol. 49, pp. 57–61, Jul 1982.
- [4] G. Binnig, C. F. Quate, and C. Gerber, “Atomic force microscope,” *Phys. Rev. Lett.*, vol. 56, pp. 930–933, Mar 1986.
- [5] Nobelprize.org, “Nobel lectures in chemistry 1996-2000,” 22 Feb 2012
<http://www.nobelprize.org>.
- [6] S. Iijima, “Helical microtubules of graphitic carbon,” *Nature*, vol. 354, no. 6348, pp. 56–58, 1991.
- [7] D. Sano, J. M. Berlin, T. T. Pham, D. C. Marcano, D. R. Valdecanas, G. Zhou, L. Milas, J. N. Myers, and J. M. Tour, “Noncovalent assembly of targeted carbon nanovectors enables synergistic drug and radiation cancer therapy *in vivo*,” *ACS Nano*, vol. 6, no. 3, pp. 2497–2505, 2012.
- [8] G. S. Schlau-Cohen, A. Ishizaki, and G. R. Fleming, “Two-dimensional electronic spectroscopy and photosynthesis: Fundamentals and applications to photosynthetic light-harvesting,” *Chemical Physics*, vol. 386, no. 13, pp. 1 – 22, 2011.
- [9] J. Boekhoven, A. Brizard, K. Kowligi, G. Koper, R. Eelkema, and J. vanEsch, “Dissipative self-assembly of a molecular gelator by using a chemical fuel,” *Angewandte Chemie*, vol. 122, no. 28, pp. 4935–4938, 2010.

Bibliography

- [10] C. L. McGuiness, G. A. Diehl, D. Blasini, D.-M. Smilgies, M. Zhu, N. Samarth, T. Weidner, N. Ballav, M. Zharnikov, and D. L. Allara, “Molecular self-assembly at bare semiconductor surfaces: Cooperative substratemolecule effects in octadecanethiolate monolayer assemblies on gaas(111), (110), and (100),” *ACS Nano*, vol. 4, no. 6, pp. 3447–3465, 2010.
- [11] M. Fuechsle, J. A. Miwa, S. Mahapatra, H. Ryu, S. Lee, O. Warschkow, L. C. L. Hollenberg, G. Klimeck, and M. Y. Simmons, “A single-atom transistor.,” *Nat Nanotechnol*, Feb 2012.
- [12] T. Kudernac, N. Ruangsupapichat, M. Parschau, B. Maci, N. Katsonis, S. R. Harutyunyan, K.-H. Ernst, and B. L. Feringa, “Electrically driven directional motion of a four-wheeled molecule on a metal surface.,” *Nature*, vol. 479, pp. 208–211, Nov 2011.
- [13] K. S. Novoselov, A. K. Geim, S. V. Morozov, D. Jiang, Y. Zhang, S. V. Dubonos, I. V. Grigorieva, and A. A. Firsov, “Electric field effect in atomically thin carbon films,” *Science*, vol. 306, no. 5696, pp. 666–669, 2004.
- [14] P. R. Wallace, “The band theory of graphite,” *Phys. Rev.*, vol. 71, pp. 622–634, May 1947.
- [15] C. Lee, X. Wei, J. W. Kysar, and J. Hone, “Measurement of the elastic properties and intrinsic strength of monolayer graphene,” *Science*, vol. 321, no. 5887, pp. 385–388, 2008.
- [16] K. S. Novoselov, “Nobel lecture: Graphene: Materials in the flatland,” *Rev. Mod. Phys.*, vol. 83, pp. 837–849, Aug 2011.
- [17] D. A. Dikin, S. Stankovich, E. J. Zimney, R. D. Piner, G. H. B. Dommett, G. Evmenenko, S. T. Nguyen, and R. S. Ruoff, “Preparation and characterization of graphene oxide paper.,” *Nature*, vol. 448, pp. 457–460, Jul 2007.
- [18] S. Stankovich, D. A. Dikin, G. H. B. Dommett, K. M. Kohlhaas, E. J. Zimney, E. A. Stach, R. D. Piner, S. T. Nguyen, and R. S. Ruoff, “Graphene-based composite materials,” *Nature*, vol. 442, pp. 282–286, 07/20/print 2006.
- [19] T. Ramanathan, A. A. Abdala, S. Stankovich, D. A. Dikin, M. Herrera-Alonso, R. D. Piner, D. H. Adamson, H. C. Schniepp,

Bibliography

- X. Chen, R. S. Ruoff, S. T. Nguyen, I. A. Aksay, R. K. Prud Homme, and L. C. Brinson, “Functionalized graphene sheets for polymer nanocomposites,” *Nat Nano*, vol. 3, pp. 327–331, 06//print 2008.
- [20] M. A. Rafiee, J. Rafiee, I. Srivastava, Z. Wang, H. Song, Z.-Z. Yu, and N. Koratkar, “Fracture and fatigue in graphene nanocomposites,” *Small*, vol. 6, no. 2, pp. 179–183, 2010.
- [21] V. Eswaraiah, K. Balasubramaniam, and S. Ramaprabhu, “One-pot synthesis of conducting graphene-polymer composites and their strain sensing application,” *Nanoscale*, vol. 4, pp. 1258–1262, 2012.
- [22] C. Chen, S. Rosenblatt, K. I. Bolotin, W. Kalb, P. Kim, I. Kymissis, H. L. Stormer, T. F. Heinz, and J. Hone, “Performance of monolayer graphene nanomechanical resonators with electrical readout.,” *Nat Nanotechnol*, vol. 4, pp. 861–867, Dec 2009.
- [23] J. T. Robinson, M. Zalalutdinov, J. W. Baldwin, E. S. Snow, Z. Wei, P. Sheehan, and B. H. Houston, “Wafer-scale reduced graphene oxide films for nanomechanical devices,” *Nano Letters*, vol. 8, no. 10, pp. 3441–3445, 2008.
- [24] J. S. Bunch, A. M. van der Zande, S. S. Verbridge, I. W. Frank, D. M. Tanenbaum, J. M. Parpia, H. G. Craighead, and P. L. McEuen, “Electromechanical resonators from graphene sheets,” *Science*, vol. 315, no. 5811, pp. 490–493, 2007.
- [25] A. Reserbat-Plantey, L. Marty, O. Arcizet, N. Bendiab, and V. Bouchiat, “A local optical probe for measuring motion and stress in a nanoelectromechanical system.,” *Nat Nanotechnol*, vol. 7, pp. 151–155, March 2012.
- [26] T. Land, T. Michely, R. Behm, J. Hemminger, and G. Comsa, “Stm investigation of single layer graphite structures produced on pt(111) by hydrocarbon decomposition,” *Surface Science*, vol. 264, no. 3, pp. 261 – 270, 1992.
- [27] C. Berger, Z. Song, X. Li, X. Wu, N. Brown, C. Naud, D. Mayou, T. Li, J. Hass, A. N. Marchenkov, E. H. Conrad, P. N. First, and W. A. de Heer, “Electronic confinement and coherence in patterned epitaxial graphene,” *Science*, vol. 312, no. 5777, pp. 1191–1196, 2006.

Bibliography

- [28] B. Peng, M. Locascio, P. Zapol, S. Li, S. L. Mielke, G. C. Schatz, and H. D. Espinosa, “Measurements of near-ultimate strength for multiwalled carbon nanotubes and irradiation-induced crosslinking improvements.,” *Nat Nanotechnol*, vol. 3, pp. 626–631, Oct 2008.
- [29] A. Szabo and N. S. Ostlund, *Modern Quantum Chemistry: Introduction to Advanced Electronic Structure Theory*. Dover Publications, 1996.
- [30] A. J. Gonis, *Theoretical Materials Science: Tracing the Electronic Origins of Materials Behavior*. Cambridge: Materials Research Society, 2000.
- [31] D. C. Rapaport, *The Art of Molecular Dynamics Simulation*. Cambridge: Cambridge University Press, 1995.
- [32] H. Eschrig, *Optimized LCAO Method: and the Electronic Structure of Extended Systems*. Cambridge: Springer, 1989.
- [33] F. Khademolhosseini, A. S. Phani, A. Nojeh, and N. Rajapakse, “Nonlocal continuum modeling and molecular dynamics simulation of torsional vibration of carbon nanotubes,” *Nanotechnology, IEEE Transactions on*, vol. 11, pp. 34 –43, jan. 2012.
- [34] Y. Q. Zhang, G. R. Liu, and J. S. Wang, “Small-scale effects on buckling of multiwalled carbon nanotubes under axial compression,” *Phys. Rev. B*, vol. 70, p. 205430, Nov 2004.
- [35] L. J. Sudak, “Column buckling of multiwalled carbon nanotubes using nonlocal continuum mechanics,” *Journal of Applied Physics*, vol. 94, no. 11, pp. 7281–7287, 2003.
- [36] Y. Q. Zhang, G. R. Liu, and X. Y. Xie, “Free transverse vibrations of double-walled carbon nanotubes using a theory of nonlocal elasticity,” *Phys. Rev. B*, vol. 71, p. 195404, May 2005.
- [37] Q. Wang, “Wave propagation in carbon nanotubes via nonlocal continuum mechanics,” *Journal of Applied Physics*, vol. 98, no. 12, p. 124301, 2005.
- [38] H. Heireche, A. Tounsi, and A. Benzair, “Scale effect on wave propagation of double-walled carbon nanotubes with initial axial loading,” *Nanotechnology*, vol. 19, no. 18, p. 185703, 2008.

Bibliography

- [39] Y.-G. Hu, K. Liew, Q. Wang, X. He, and B. Yakobson, “Nonlocal shell model for elastic wave propagation in single- and double-walled carbon nanotubes,” *Journal of the Mechanics and Physics of Solids*, vol. 56, no. 12, pp. 3475 – 3485, 2008.
- [40] S. Cuenot, C. Frétigny, S. Demoustier-Champagne, and B. Nysten, “Surface tension effect on the mechanical properties of nanomaterials measured by atomic force microscopy,” *Phys. Rev. B*, vol. 69, p. 165410, Apr 2004.
- [41] R. Dingreville, J. Qu, and M. Cherkaoui, “Surface free energy and its effect on the elastic behavior of nano-sized particles, wires and films,” *Journal of the Mechanics and Physics of Solids*, vol. 53, no. 8, pp. 1827 – 1854, 2005.
- [42] A. W. McFarland, M. A. Poggi, M. J. Doyle, L. A. Bottomley, and J. S. Colton, “Influence of surface stress on the resonance behavior of microcantilevers,” *Applied Physics Letters*, vol. 87, no. 5, p. 053505, 2005.
- [43] L. He, C. Lim, and B. Wu, “A continuum model for size-dependent deformation of elastic films of nano-scale thickness,” *International Journal of Solids and Structures*, vol. 41, no. 34, pp. 847 – 857, 2004.
- [44] C. Liu and R. Rajapakse, “Continuum models incorporating surface energy for static and dynamic response of nanoscale beams,” *Nanotechnology, IEEE Transactions on*, vol. 9, pp. 422 –431, july 2010.
- [45] C. Liu, R. K. N. D. Rajapakse, and A. S. Phani, “Finite element modeling of beams with surface energy effects,” *Journal of Applied Mechanics*, vol. 78, no. 3, p. 031014, 2011.
- [46] J. Wackerfu, “Molecular mechanics in the context of the finite element method,” *International Journal for Numerical Methods in Engineering*, vol. 77, no. 7, pp. 969–997, 2009.
- [47] K. Tserpes and P. Papanikos, “Finite element modeling of single-walled carbon nanotubes,” *Composites Part B: Engineering*, vol. 36, no. 5, pp. 468 – 477, 2005.
- [48] G. M. Odegard, T. S. Gates, L. M. Nicholson, and K. E. Wise, “Equivalent-continuum modeling of nano-structured materials,”

Bibliography

- Composites Science and Technology*, vol. 62, no. 14, pp. 1869 – 1880, 2002.
- [49] M. Meo and M. Rossi, “Prediction of youngs modulus of single wall carbon nanotubes by molecular-mechanics based finite element modelling,” *Composites Science and Technology*, vol. 66, no. 11-12, pp. 1597 – 1605, 2006.
 - [50] L. Nasdala and G. Ernst, “Development of a 4-node finite element for the computation of nano-structured materials,” *Computational Materials Science*, vol. 33, no. 4, pp. 443 – 458, 2005.
 - [51] L. Nasdala, G. Ernst, M. Lengnick, and H. Rothert, “Finite element analysis of carbon nanotubes with stone-wales defects,” *Computer Modeling in Engineering and Sciences*, vol. 7, pp. 293–304, MAR 2005.
 - [52] B. Liu, Y. Huang, H. Jiang, S. Qu, and K. Hwang, “The atomic-scale finite element method,” *Computer Methods in Applied Mechanics and Engineering*, vol. 193, no. 17-20, pp. 1849 – 1864, 2004.
 - [53] B. Liu, H. Jiang, Y. Huang, S. Qu, M.-F. Yu, and K. C. Hwang, “Atomic-scale finite element method in multiscale computation with applications to carbon nanotubes,” *Phys. Rev. B*, vol. 72, p. 035435, Jul 2005.
 - [54] C. O. Girit, J. C. Meyer, R. Erni, M. D. Rossell, C. Kisielowski, L. Yang, C.-H. Park, M. F. Crommie, M. L. Cohen, S. G. Louie, and A. Zettl, “Graphene at the edge: Stability and dynamics,” *Science*, vol. 323, no. 5922, pp. 1705–1708, 2009.
 - [55] Y.-W. Son, M. L. Cohen, and S. G. Louie, “Energy gaps in graphene nanoribbons,” *Phys. Rev. Lett.*, vol. 97, p. 216803, Nov 2006.
 - [56] Z. Ni, H. Bu, M. Zou, H. Yi, K. Bi, and Y. Chen, “Anisotropic mechanical properties of graphene sheets from molecular dynamics,” *Physica B: Condensed Matter*, vol. 405, no. 5, pp. 1301 – 1306, 2010.
 - [57] K. A. Ritter and J. W. Lyding, “The influence of edge structure on the electronic properties of graphene quantum dots and nanoribbons,” *Nat Mater*, vol. 8, pp. 235–242, Mar 2009.

Bibliography

- [58] H. Zhao, K. Min, and N. R. Aluru, “Size and chirality dependent elastic properties of graphene nanoribbons under uniaxial tension,” *Nano Letters*, vol. 9, no. 8, pp. 3012–3015, 2009.
- [59] R. Faccio, P. A. Denis, H. Pardo, C. Goyenola, and A. W. Mombru, “Mechanical properties of graphene nanoribbons,” *Journal of Physics: Condensed Matter*, vol. 21, no. 28, p. 285304, 2009.
- [60] M. Burghard, H. Klauk, and K. Kern, “Carbon-based field-effect transistors for nanoelectronics,” *Advanced Materials*, vol. 21, no. 25-26, pp. 2586–2600, 2009.
- [61] M. Topsakal and S. Ciraci, “Elastic and plastic deformation of graphene, silicene, and boron nitride honeycomb nanoribbons under uniaxial tension: A first-principles density-functional theory study,” *Phys. Rev. B*, vol. 81, p. 024107, Jan 2010.
- [62] Q. Lu, W. Gao, and R. Huang, “Atomistic simulation and continuum modeling of graphene nanoribbons under uniaxial tension,” *Modelling and Simulation in Materials Science and Engineering*, vol. 19, no. 5, p. 054006, 2011.
- [63] V. B. Shenoy, C. D. Reddy, A. Ramasubramaniam, and Y. W. Zhang, “Edge-stress-induced warping of graphene sheets and nanoribbons,” *Phys. Rev. Lett.*, vol. 101, p. 245501, Dec 2008.
- [64] C. D. Reddy, A. Ramasubramaniam, V. B. Shenoy, and Y.-W. Zhang, “Edge elastic properties of defect-free single-layer graphene sheets,” *Journal of Applied Physics*, vol. 94, no. 10, p. 101904, 2009.
- [65] Q. Lu and R. Huang, “Excess energy and deformation along free edges of graphene nanoribbons,” *Phys. Rev. B*, vol. 81, p. 155410, Apr 2010.
- [66] H. Bu, Y. Chen, M. Zou, H. Yi, K. Bi, and Z. Ni, “Atomistic simulations of mechanical properties of graphene nanoribbons,” *Physics Letters A*, vol. 373, no. 37, pp. 3359 – 3362, 2009.
- [67] F. Banhart, J. Kotakoski, and A. V. Krasheninnikov, “Structural defects in graphene,” *ACS Nano*, vol. 5, no. 1, pp. 26–41, 2011.
- [68] R. Ansari, S. Ajori, and B. Motevalli, “Mechanical properties of defective single-layered graphene sheets via molecular dynamics

Bibliography

- simulation,” *Superlattices and Microstructures*, vol. 51, no. 2, pp. 274 – 289, 2012.
- [69] A. Hashimoto, K. Suenaga, A. Gloter, K. Urita, and S. Iijima, “Direct evidence for atomic defects in graphene layers.,” *Nature*, vol. 430, pp. 870–873, Aug 2004.
- [70] M. H. Gass, U. Bangert, A. L. Bleloch, P. Wang, R. R. Nair, and A. K. Geim, “Free-standing graphene at atomic resolution.,” *Nat Nanotechnol*, vol. 3, pp. 676–681, Nov 2008.
- [71] R. Khare, S. L. Mielke, J. T. Paci, S. Zhang, R. Ballarini, G. C. Schatz, and T. Belytschko, “Coupled quantum mechanical/molecular mechanical modeling of the fracture of defective carbon nanotubes and graphene sheets,” *Phys. Rev. B*, vol. 75, p. 075412, Feb 2007.
- [72] M. Wang, C. Yan, L. Ma, N. Hu, and M. Chen, “Effect of defects on fracture strength of graphene sheets,” *Computational Materials Science*, vol. 54, no. 0, pp. 236 – 239, 2012.
- [73] N. M. Pugno and R. S. Ruoff , “Quantized fracture mechanics,” *Philosophical Magazine*, vol. 84, no. 27, pp. 2829–2845, 2004.
- [74] N. Pugno, A. Carpinteri, M. Ippolito, A. Mattoni, and L. Colombo, “Atomistic fracture: Qfm vs. md,” *Engineering Fracture Mechanics*, vol. 75, no. 7, pp. 1794 – 1803, 2008.
- [75] A. A. Griffith, “The phenomena of rupture and flow in solids,” *Philosophical Transactions of the Royal Society of London. Series A, Containing Papers of a Mathematical or Physical Character*, vol. 221, no. 582-593, pp. 163–198, 1921.
- [76] B. J. Alder and T. E. Wainwright, “Phase transition for a hard sphere system,” *The Journal of Chemical Physics*, vol. 27, no. 5, pp. 1208–1209, 1957.
- [77] H. C. Andersen, “Molecular dynamics simulations at constant pressure and/or temperature,” *The Journal of Chemical Physics*, vol. 72, no. 4, pp. 2384–2393, 1980.
- [78] G. Bussi, D. Donadio, and M. Parrinello, “Canonical sampling through velocity rescaling,” *The Journal of Chemical Physics*, vol. 126, no. 1, pp. 014101–7, 2007.

Bibliography

- [79] H. J. C. Berendsen, J. P. M. Postma, W. F. van Gunsteren, A. DiNola, and J. R. Haak, “Molecular dynamics with coupling to an external bath,” *The Journal of Chemical Physics*, vol. 81, no. 8, pp. 3684–3690, 1984.
- [80] P. H. Hnenberger, “Thermostat algorithms for molecular dynamics simulations,” *Advanced Computer Simulation*, vol. 173, no. 173, pp. 105–149, 2005.
- [81] D. J. Evans and B. L. Holian, “The nose–hoover thermostat,” *The Journal of Chemical Physics*, vol. 83, no. 8, pp. 4069–4074, 1985.
- [82] W. G. Hoover, “Canonical dynamics: Equilibrium phase-space distributions,” *Phys. Rev. A*, vol. 31, pp. 1695–1697, Mar 1985.
- [83] S. Nosé, “A unified formulation of the constant temperature molecular dynamics methods,” *The Journal of Chemical Physics*, vol. 81, no. 1, pp. 511–519, 1984.
- [84] S. Nosé, “A molecular dynamics method for simulations in the canonical ensemble,” *Molecular Physics*, vol. 52, no. 2, pp. 255–268, 1984.
- [85] G. J. Martyna, D. J. Tobias, and M. L. Klein, “Constant pressure molecular dynamics algorithms,” *The Journal of Chemical Physics*, vol. 101, no. 5, pp. 4177–4189, 1994.
- [86] M. Griebel and J. Hamaekers, “Molecular dynamics simulations of the mechanical properties of polyethylene-carbon nanotube composites,” in *Handbook of Theoretical and Computational Nanotechnology* (M. Rieth and W. Schommers, eds.), vol. 9, ch. 8, pp. 409–454, American Scientific Publishers, 2006.
- [87] M. E. Tuckerman, J. Alejandre, R. Lpez-Rendn, A. L. Jochim, and G. J. Martyna, “A liouville-operator derived measure-preserving integrator for molecular dynamics simulations in the isothermalisobaric ensemble,” *Journal of Physics A: Mathematical and General*, vol. 39, no. 19, p. 5629, 2006.
- [88] T. Belytschko, S. P. Xiao, G. C. Schatz, and R. S. Ruoff, “Atomistic simulations of nanotube fracture,” *Phys. Rev. B*, vol. 65, p. 235430, Jun 2002.

Bibliography

- [89] S. J. Stuart, A. B. Tutein, and J. A. Harrison, “A reactive potential for hydrocarbons with intermolecular interactions,” *Journal of Applied Physics*, vol. 112, no. 14, pp. 6472–6486, 2000.
- [90] D. W. Brenner, “Empirical potential for hydrocarbons for use in simulating the chemical vapor deposition of diamond films,” *Physical Review B*, vol. 42, p. 9458, 11/15/ 1990.
- [91] O. A. Shenderova, D. W. Brenner, A. Omelchenko, X. Su, and L. H. Yang, “Atomistic modeling of the fracture of polycrystalline diamond,” *Phys. Rev. B*, vol. 61, pp. 3877–3888, Feb 2000.
- [92] R. Grantab, V. B. Shenoy, and R. S. Ruoff, “Anomalous strength characteristics of tilt grain boundaries in graphene,” *Science*, vol. 330, no. 6006, pp. 946–948, 2010.
- [93] F. Liu, P. Ming, and J. Li, “*Ab initio* calculation of ideal strength and phonon instability of graphene under tension,” *Phys. Rev. B*, vol. 76, p. 064120, Aug 2007.
- [94] J. E. Jones, “On the determination of molecular fields. ii. from the equation of state of a gas,” *Proceedings of the Royal Society of London. Series A*, vol. 106, no. 738, pp. 463–477, 1924.
- [95] S. Plimpton, “Fast parallel algorithms for short-range molecular dynamics,” *J. Comput. Phys.*, vol. 117, pp. 1–19, March 1995.
- [96] K. Mylvaganam and L. Zhang, “Important issues in a molecular dynamics simulation for characterising the mechanical properties of carbon nanotubes,” *Carbon*, vol. 42, no. 10, pp. 2025 – 2032, 2004.
- [97] H. Zhao and N. R. Aluru, “Temperature and strain-rate dependent fracture strength of graphene,” *Journal of Applied Physics*, vol. 108, no. 6, p. 064321, 2010.
- [98] T. Dumitrica and B. I. Yakobson, “Strain-rate and temperature dependent plastic yield in carbon nanotubes from ab initio calculations,” *Applied Physics Letters*, vol. 84, no. 15, pp. 2775–2777, 2004.
- [99] T. Dumitrica, M. Hua, and B. I. Yakobson, “Symmetry-, time-, and temperature-dependent strength of carbon nanotubes,” *Proceedings of the National Academy of Sciences*, vol. 103, no. 16, pp. 6105–6109, 2006.

Bibliography

- [100] S. Plimpton, A. Thompson, and P. Crozier, “Lammps molecular dynamics simulator,” February 2012 <http://lammps.sandia.gov/>.
- [101] W. Humphrey, A. Dalke, and K. Schulten, “VMD – Visual Molecular Dynamics,” *Journal of Molecular Graphics*, vol. 14, pp. 33–38, 1996.
- [102] W. Humphrey, A. Dalke, and K. Schulten, “Vmd - molecular graphics viewer,” February 2012
<http://www.ks.uiuc.edu/Research/vmd/>.
- [103] V. Singh, S. Sengupta, H. S. Solanki, R. Dhall, A. Allain, S. Dhara, P. Pant, and M. M. Deshmukh, “Probing thermal expansion of graphene and modal dispersion at low-temperature using graphene nanoelectromechanical systems resonators,” *Nanotechnology*, vol. 21, no. 16, p. 165204, 2010.
- [104] W. Bao, F. Miao, Z. Chen, H. Zhang, W. Jang, C. Dames, and C. N. Lau, “Controlled ripple texturing of suspended graphene and ultrathin graphite membranes.,” *Nat Nanotechnol*, vol. 4, pp. 562–566, Sep 2009.
- [105] J.-W. Jiang, J.-S. Wang, and B. Li, “Thermal expansion in single-walled carbon nanotubes and graphene: Nonequilibrium green’s function approach,” *Phys. Rev. B*, vol. 80, p. 205429, Nov 2009.
- [106] A. Fasolino, J. H. Los, and M. I. Katsnelson, “Intrinsic ripples in graphene.,” *Nat Mater*, vol. 6, pp. 858–861, Nov 2007.
- [107] C. H. Lui, L. Liu, K. F. Mak, G. W. Flynn, and T. F. Heinz, “Ultraflat graphene.,” *Nature*, vol. 462, pp. 339–341, Nov 2009.
- [108] M. Pozzo, D. Alfè, P. Lacovig, P. Hofmann, S. Lizzit, and A. Baraldi, “Thermal expansion of supported and freestanding graphene: Lattice constant versus interatomic distance,” *Phys. Rev. Lett.*, vol. 106, p. 135501, Mar 2011.
- [109] J. Cormier, J. M. Rickman, and T. J. Delph, “Stress calculation in atomistic simulations of perfect and imperfect solids,” *Journal of Applied Physics*, vol. 89, no. 1, pp. 99–104, 2001.
- [110] J. H. Irving and J. G. Kirkwood, “The statistical mechanical theory of transport processes. iv. the equations of hydrodynamics,” *The Journal of Chemical Physics*, vol. 18, no. 6, pp. 817–829, 1950.

Bibliography

- [111] R. J. Hardy, “Formulas for determining local properties in molecular-dynamics simulations: Shock waves,” *The Journal of Chemical Physics*, vol. 76, no. 1, pp. 622–628, 1982.
- [112] J. F. Lutsko, “Stress and elastic constants in anisotropic solids: Molecular dynamics techniques,” *Journal of Applied Physics*, vol. 64, no. 3, pp. 1152–1154, 1988.
- [113] K. S. Cheung and S. Yip, “Atomic-level stress in an inhomogeneous system,” *Journal of Applied Physics*, vol. 70, no. 10, pp. 5688–5690, 1991.
- [114] D. H. Tsai, “The virial theorem and stress calculation in molecular dynamics,” *The Journal of Chemical Physics*, vol. 70, no. 3, pp. 1375–1382, 1979.
- [115] R. Clausius, “On a mechanical theorem applicable to heat,” *Philosophical Magazine Series 4*, vol. 40, no. 265, pp. 122–127, 1870.
- [116] R. J. Swenson, “Comments on virial theorems for bounded systems,” *American Journal of Physics*, vol. 51, no. 10, pp. 940–942, 1983.
- [117] M. Zhou, “A new look at the atomic level virial stress: on continuum-molecular system equivalence,” *Proceedings of the Royal Society of London. Series A: Mathematical, Physical and Engineering Sciences*, vol. 459, no. 2037, pp. 2347–2392, 2003.
- [118] A. K. Subramanyan and C. Sun, “Continuum interpretation of virial stress in molecular simulations,” *International Journal of Solids and Structures*, vol. 45, no. 14-15, pp. 4340 – 4346, 2008.
- [119] E. Cadelano, P. L. Palla, S. Giordano, and L. Colombo, “Nonlinear elasticity of monolayer graphene,” *Phys. Rev. Lett.*, vol. 102, p. 235502, Jun 2009.
- [120] P. Koskinen, S. Malola, and H. Häkkinen, “Self-passivating edge reconstructions of graphene,” *Phys. Rev. Lett.*, vol. 101, p. 115502, Sep 2008.
- [121] B. Huang, M. Liu, N. Su, J. Wu, W. Duan, B.-l. Gu, and F. Liu, “Quantum manifestations of graphene edge stress and edge instability: A first-principles study,” *Phys. Rev. Lett.*, vol. 102, p. 166404, Apr 2009.

Bibliography

- [122] S. Jun, “Density-functional study of edge stress in graphene,” *Phys. Rev. B*, vol. 78, p. 073405, Aug 2008.
- [123] R. C. Cammarata, “Surface and interface stress effects in thin films,” *Progress in Surface Science*, vol. 46, no. 1, pp. 1 – 38, 1994.
- [124] O. Gürseren, T. Yildirim, and S. Ciraci, “Systematic *ab initio* study of curvature effects in carbon nanotubes,” *Phys. Rev. B*, vol. 65, p. 153405, Mar 2002.
- [125] D. Sánchez-Portal, E. Artacho, J. M. Soler, A. Rubio, and P. Ordejón, “*Ab initio* structural, elastic, and vibrational properties of carbon nanotubes,” *Phys. Rev. B*, vol. 59, pp. 12678–12688, May 1999.
- [126] E. Hernández, C. Goze, P. Bernier, and A. Rubio, “Elastic properties of c and $B_xC_yN_z$ composite nanotubes,” *Phys. Rev. Lett.*, vol. 80, pp. 4502–4505, May 1998.
- [127] K. Suenaga, H. Wakabayashi, M. Koshino, Y. Sato, K. Urita, and S. Iijima, “Imaging active topological defects in carbon nanotubes,” *Nat Nanotechnol*, vol. 2, pp. 358–360, Jun 2007.
- [128] A. Omelchenko, J. Yu, R. K. Kalia, and P. Vashishta, “Crack front propagation and fracture in a graphite sheet: A molecular-dynamics study on parallel computers,” *Phys. Rev. Lett.*, vol. 78, pp. 2148–2151, Mar 1997.
- [129] M. Xu, A. Tabarraei, J. Paci, J. Oswald, and T. Belytschko, “A coupled quantum/continuum mechanics study of graphene fracture,” *International Journal of Fracture*, pp. 1–11, 2012.
- [130] K. Kim, V. I. Artyukhov, W. Regan, Y. Liu, M. F. Crommie, B. I. Yakobson, and A. Zettl, “Ripping graphene: Preferred directions,” *Nano Letters*, vol. 12, no. 1, pp. 293–297, 2012.
- [131] F. Cleri, S. R. Phillpot, D. Wolf, and S. Yip, “Atomistic simulations of materials fracture and the link between atomic and continuum length scales,” *Journal of the American Ceramic Society*, vol. 81, no. 3, pp. 501–516, 1998.
- [132] A. Mattoni, L. Colombo, and F. Cleri, “Atomic scale origin of crack resistance in brittle fracture,” *Phys. Rev. Lett.*, vol. 95, p. 115501, Sep 2005.

Bibliography

- [133] C. Inglis, “Stress in a plate due to the presence of cracks and sharp corners,” *Trans R Inst Naval Architects*, vol. 60, p. 219241, 1913.
- [134] T. L. Anderson, *Fracture Mechanics: Fundamentals and Applications*. Taylor & Francis, 2005.

Appendix A Input Files for LAMMPS

LAMMPS input file *in.graphene* to simulate the uniaxial tensile test in Section 2.5.1 is given below.

```
##-----INITIALIZATION-----
units      metal
dimension   3
boundary    f p f
atom_style  atomic
newton     on

##-----ATOM DEFINITION-----
read_data   data.grap

##-----SETTINGS-----
pair_style  airebo 3.0
pair_coeff  * * ~ LAMMPS/lammps-7Apr11/potentials/CH.airbo C

timestep   0.0005
fix        1 all npt temp 300 300 0.05 y 0 0 0.5
thermo     20

compute    1 all stress/atom
compute    2 all pe/atom pair bond
compute    3 all reduce sum c_1[1] c_1[2] c_1[3]
```

Appendix A Input Files for LAMMPS

```
thermo_style      custom step temp pe etotal lx ly pxx pyy c_3[1] c_3[2] c_3[3]

##-----RUNING-RELAXATION-----
run      60000

##-----RUNNING-DEFORMATION-----
unfix      1
fix      1 all nvt temp 300 300 0.05

fix      2 all ave/atom 1 1000 1000 c_1[1] c_1[2] c_1[3] c_2 fx fy fz
dump     1 all custom 1000 dump.new.* id type x y z vx vy vz c_1[1] c_1[2] c_1[3]
c_2 f_2[1] f_2[2] f_2[3] f_2[4] f_2[5] f_2[6] f_2[7]

variable    srate equal 1.0e9
variable    srate1 equal "v_srate / 1.0e12"
fix      3 all deform 1 y erate $srate1 units box remap x

run      600000
```

Appendix A Input Files for LAMMPS

Part of the LAMMPS input file data.graphene to simulate the uniaxial tensile test in Section 2.5.1 is given below.

252 atoms

1 atom types

Masses

1 12.010000

#simulation box

-1.396000 12.564000 xlo xhi

-0.604486 50.172316 ylo yhi

-2.000000 2.000000 zlo zhi

Atoms

1 1 0.698000 0.000000 0.000000

2 1 0.000000 1.208971 0.000000

3 1 0.698000 2.417943 0.000000

4 1 0.000000 3.626914 0.000000

5 1 0.698000 4.835886 0.000000

6 1 0.000000 6.044857 0.000000

.....

.

.

.

250 1 11.168000 47.149887 0.000000

251 1 10.470000 48.358859 0.000000

252 1 11.168000 49.567830 0.000000

Appendix A Input Files for LAMMPS

LAMMPS output file log.lammps of the uniaxial tensile test in Section 2.5.1 is given below.

```
Step Temp PotEng KinEng TotEng Lx Ly Pxx Pyy 3[1] 3[2] 3[3]
0 0 -1759.0 0 -1759.0 13.96 50.77 -13041.9 81852.3 0.37e+08 -2.32e+08 0
20 22.7 -1760.5 0.73 -1759.7 13.96 51.01 -23485.6 92940.9 0.67e+08 -2.65e+08 0
40 13.2 -1761.2 0.43 -1760.8 13.96 51.69 -19014.7 -11949.8 0.55e+08 0.34e+08 0
60 13.6 -1760.1 0.44 -1759.6 13.96 52.31 -45878.3 -86754.5 1.34e+08 2.53e+08 0
80 34.3 -1760.4 1.11 -1759.2 13.96 52.41 -14782.4 -97297.1 0.43e+08 2.85e+08 0
.....
```

Appendix B Input Files for VMD

Part of the VMD input file graphene.lammpstrj to visualize the uniaxial tensile test in Section 2.5.1 is give below.

```
ITEM: Timestep
0
ITEM: Number of Atoms
252
ITEM: Box Bounds pp pp ff
-1.396000 12.564000
-0.604486 50.172300
-2.000000 2.000000
ITEM: Atoms id type x y z
1 0 0.698000 0.000000 0.000000
2 1 0.000000 1.208970 0.000000
3 1 0.698000 2.417940 0.000000
.
.
.
250 1 11.168000 47.149900 0.000000
251 1 10.470000 48.358900 0.000000
252 1 11.168000 49.567800 0.000000
```

ITEM: Timestep

Appendix B Input Files for VMD

```
1000  
ITEM: NUMBER OF ATOMS  
252  
ITEM: BOX BOUNDS pp pp ff  
-1.396000 12.564000  
-0.966049 50.533900  
-2.000000 2.000000  
ITEM: ATOMS id type x y z  
1 0 0.648417 -0.352954 0.000000  
2 1 0.002844 0.873234 0.000000  
3 1 0.648417 2.099420 0.000000  
. .  
. .  
250 1 11.165200 47.468400 0.000000  
251 1 10.519600 48.694600 0.000000  
252 1 11.165200 49.920800 0.000000
```

```
ITEM: Timestep  
2000  
ITEM: NUMBER OF ATOMS  
252  
ITEM: BOX BOUNDS pp pp ff  
-1.396000 12.564000  
-1.294850 50.862700  
-2.000000 2.000000  
ITEM: ATOMS id type x y z  
1 0 0.763745 -0.673928 0.000000  
2 1 0.052989 0.567919 0.000000  
3 1 0.763745 1.809760 0.000000  
. .
```

Appendix B Input Files for VMD

```
250 1 11.115000 47.758100 0.000000  
251 1 10.404300 48.999900 0.000000  
252 1 11.115000 50.241800 0.000000
```

.....